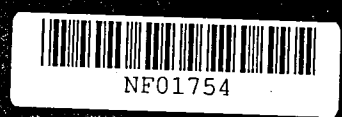

JPL NO. 9950-552

AeroChem TP-410

DOE/JPL 955491-81/6

Distribution Category:UC-63



# DEVELOPMENT OF PROCESSES FOR THE PRODUCTION OF SOLAR GRADE SILICON FROM HALIDES AND ALKALI METALS

PHASE I

C.R. DICKSON AND R.K. GOULD



PHASE II

C.R. DICKSON, W. FELDER, AND R.K. GOULD



FINAL REPORT

MARCH 1981



The JPL Low-Cost Silicon Solar Array Project is sponsored by the U.S. Department of Energy and forms part of the Solar Photovoltaic Conversion Program to initiate a major effort toward the development of low-cost solar arrays. This work was performed for the Jet Propulsion Laboratory, California Institute of Technology by agreement between NASA and DoE.

AeroChem Research Laboratories, Inc.

Princeton, New Jersey

DRL No. 118
Item No. 4, DRD No. QR

DOE/JPL 955491-81/6
Distribution Category:UC-63

# DEVELOPMENT OF PROCESSES FOR THE PRODUCTION OF SOLAR GRADE SILICON FROM HALIDES AND ALKALI METALS



PHASE I

C.R. DICKSON AND R.K. GOULD

PHASE II

C.R. DICKSON, W. FELDER, AND R.K. GOULD

FINAL REPORT

MARCH 1981

JPL Contract No. 955491
LSA Task 1, SILICON MATERIAL



Approved by:

Hartwell F. Calcote
Director of Research

AeroChem Research Laboratories, Inc.
Princeton, New Jersey

## FOREWORD AND ACKNOWLEDGMENTS

This is the final report on a program covering the period October 1979 to February 1981. The following people contributed to this program: A. Wilczynski, P.J. Howard, R.F. Burkert, and J. Allen.

## ABSTRACT

Phase I of this program was directed toward the development of processes involving high temperature reactions of silicon halides with alkali metals for the production of solar grade silicon in volume at low cost. Experiments were performed to evaluate product separation and collection processes, measure heat release parameters for scaling purposes, determine the effects of reactants and/or products on materials of reactor construction, and make preliminary engineering and economic analyses of a scaled-up process. Samples of the silicon product were delivered to JPL for evaluation of solar cell performance.

Using a laboratory scale apparatus, the feasibility of the basic process to make and collect silicon was demonstrated. The first product samples of silicon were small, weighing 1 to 3 g, and were produced with separation/collection efficiencies of 10 to 30%. At the end of the contract, metallic silicon ingots weighing $\approx$ 1/4 kg were produced routinely in one-hour runs with separation/collection efficiencies of $\approx$ 80%. The process produced pure silicon free of the sodium reactant (< 10 ppma). Other impurities were present at levels of 1-10 ppma or lower. The jet impaction/separation process was also demonstrated to be a purification process. In some cases, the impurity concentration decreased by a factor of $10^3$ or more.

A preliminary engineering and economic analysis made on the AeroChem process showed that it has a low manufacturing cost and the lowest plant cost of all the present JPL sponsored processes. Most importantly, the AeroChem process produces the silicon product at the low price of $10/kg in 1980 dollars.

The objective of Phase II of the program was to characterize the kinetics and mechanism of the formation and growth of silicon particles from the decomposition of silane at high temperatures. The experiments were aimed at determining the rates at which gas-phase species form silicon particle precursors, the time required for silane decomposition to produce particles, and the competing rate of growth of silicon seed particles injected into a decomposing silane environment.

A high-temperature fast-flow reactor (HTFFR) was modified to study the decomposition of silane and the subsequent growth of particles. Particle growth measurements were made as functions of temperature (873-1473 K), pressure (50-550 Torr), and residence time (0.5 to 30 ms). Optical diagnostics consisting of absorption and Mie scattering of the light at 90° from He-Ne or $Ar^+$ lasers

were used to determine the appearance growth rates and absolute sizes of the particles. The extent of silane decomposition as a function of residence time, temperature, and pressure was measured by infrared absorption spectroscopy. These measurements were used to determine the particle concentrations corresponding to the particle growth measurements. Particles were collected in the HTFFR observation zone as a check on the particle concentrations measured optically. The growth of seeded silicon particles was studied in a decomposing silane environment at 873 K, 1173 K, and 1473 K. The seeded particles were either a commercial silicon powder (nominal 5 μm diam) or JPL silicon samples ($\approx$ 0.1-0.2 μm diam) produced in a free space reactor. Unsuccessful attempts were made to observe Si atoms and the molecular species SiH, $SiH_2$, and $Si_2H_6$. Finally, a simplistic model is presented to explain the growth of silicon in a decomposing silane environment.

This final report is divided into two independent sections describing work on Phases I and II of the contract.

PHASE I

## TABLE OF CONTENTS



## LIST OF TABLES

## LIST OF FIGURES

PHASE II

## TABLE OF CONTENTS



## LIST OF TABLES

T-410

# LIST OF FIGURES

# PHASE I

## I. INTRODUCTION

The object of this program was to determine the feasibility of using continuous high temperature flames of alkali metals and silicon halides to produce high purity "solar grade" silicon in large quantities. These flames have been observed previously[1-7] and were found to be characterized by fast kinetics and a variety of chemiluminescent emissions. Equilibrium thermochemical calculations[4] indicate that high adiabatic flame temperatures ($\approx$ 2400 K) are attained and that solid or liquid silicon is the only condensed phase present in the equilibrium product distributions at these temperatures. Thus, separation of the condensed silicon from the gas-phase reaction products offers the potential for a large scale industrial process for the preparation of high purity "solar grade" silicon.

The aims of this program were to achieve product separation, to test various reactor/collector designs, and to run the silicon test apparatus for extended periods of time. Initially, the silicon test apparatus was run repetitively on a routine basis for twenty minutes until all of the sodium reagent in the vaporizer was depleted. These runs enabled the measurement of the reagent flow rates and the silicon collection efficiencies. Samples of metallic silicon weighing 50 to 80 g were collected by an impaction process at efficiencies of 60 to 80%. This was especially encouraging since complete product separation was demonstrated. Unlike the separation in a graphite flow tube achieved in a previous contract,[3] the silicon separated by the impaction process produced only metallic-like silicon ingots with no visible evidence of the powdered product. Analysis of these samples by plasma emission spectroscopy showed the sodium content to be less than 10 ppma.

Toward the end of this contract, a new large capacity (3 kg) Na vaporizer was constructed, installed, and put into operation. The first successful run lasted 1 1/4 h and produced a 238 g of separated silicon at an 82% collection efficiency. One hour runs were subsequently made on a routine basis. Samples from these runs were submitted to JPL for evaluation.

A preliminary engineering and economic analysis of the AeroChem process was made. This analysis showed that the AeroChem process has a low manufacturing

cost and the lowest plant cost of all the present JPL sponsored processes. Most importantly, the AeroChem process produces the silicon product at the low price of $10/kg Si in 1980 dollars. This price is below the Task I objective of the JPL Low-Cost Solar Array Project to produce solar grade silicon at a cost of less than $10 per kg in 1975 dollars.

## II. BACKGROUND

The reactions of silicon halides with alkali metals have been studied extensively at AeroChem with funding from JPL as part of Task I of the Low-Cost Solar Array Project.[1-7] Over the past few years AeroChem has developed a flame process in which silicon is obtained from the rapid, exothermic reaction of silicon tetrachloride and sodium. The reaction of $SiCl_4(g)$ with Na vapor is luminous and rapidly approaches thermochemical equilibrium representing 95 to 99% conversion to silicon and sodium chloride. In all cases we have examined, the reaction rate appears to be mixing limited. The reaction is very exothermic, i.e., for the reaction with sodium vapor

$$4Na + SiCl_4 \rightarrow Si + 4NaCl$$

the heats of reaction at 298 K and 1800 K are $\Delta H_{298} = -234.64$ kcal mol$^{-1}$ and $\Delta H_{1800} = -109.78$ kcal mol$^{-1}$, respectively. The adiabatic flame temperature, depending on pressure, lies in the range 2200-2500 K, but the intense thermal emission from the silicon droplet fume in actual systems quickly drops the temperature. If the reactor is operated with its walls at 1700 to 1800 K, the reaction products remain as NaCl(g) and Si(ℓ) and the difference in phase of the two products can be exploited to separate them. If the reaction is conducted in a cool reactor, NaCl condenses and first Si and then NaCl rapidly freeze so that the resulting product is a very fine brown powder made up of 90% (by weight) salt particles and 10% submicron Si particles.

The present process has several distinct advantages. Before mixing in the reactor, both reagents are vaporized, thereby contributing to a purer silicon product. The enthalpy of vaporization that would normally be lost in a separate distillation process for reagent purification can, in this configuration, contribute to maintaining the high temperatures in the post-flame gases necessary for product separation. Also the product separation may be a purification process since impurities may be carried away with the salt vapor instead

of condensing with the silicon. Finally, little inert gas diluent is required (or desired) in these diffusion flames which results in an obvious economic advantage.

To consider any laboratory process for scale-up to industrial production, a crude energy balance is informative. Figure 1 shows the energy requirements of the silicon test apparatus and other energy requirements from thermochemical calculations. The major power requirement ($\approx$ 5 kWh/kg Si) is for the sodium vaporization process. Very little power ($\approx$ 0.3 kWh/kg Si) is required for the vaporization of $SiCl_4$. On the present laboratory scale $\approx$ 12-14 kWh/kg Si is required to heat the reactor. The exothermicity of the reaction gives a net release of 2.5 kWh/kg Si. For a commercial scale reactor this reaction heat release would largely supply the energy needed to heat the reactor. Upon condensation of the salt product, an additional 8 kWh/kg Si will be released. Thus, the AeroChem process has obvious energy saving advantages.

As part of Task I of the JPL Low-Cost Solar Array Project the overall objective is to produce solar grade silicon at a cost of less than $10/kg (in 1975 dollars). Present technology produces semiconductor grade silicon at a cost between $40 and $60/kg, so a factor of four or more reduction in cost is desired with only slightly less stringent purity requirements. All of the above advantages indicated that the proposed AeroChem process should produce very cheap silicon of high purity within the objectives of Task I of the Low-Cost Solar Array Project.

## III. NEW SILICON TEST APPARATUS

### A. GENERAL DESCRIPTION

The new silicon test apparatus evolved throughout this program to its present form as shown in Fig. 2. The apparatus consisted of four main sections: the power supplies, the control panels, the reagent vaporizers, and the reactor/crucible assembly contained in the process vessel. As the new silicon test apparatus was brought to an operational stage, several modifications were made on each of these sections. Briefly, variable transformers replaced welder power supplies as power sources, the control panel was reorganized to give a better view of the pressure, temperature, and electrical monitors, and design changes were made on the reactor/crucible assembly.

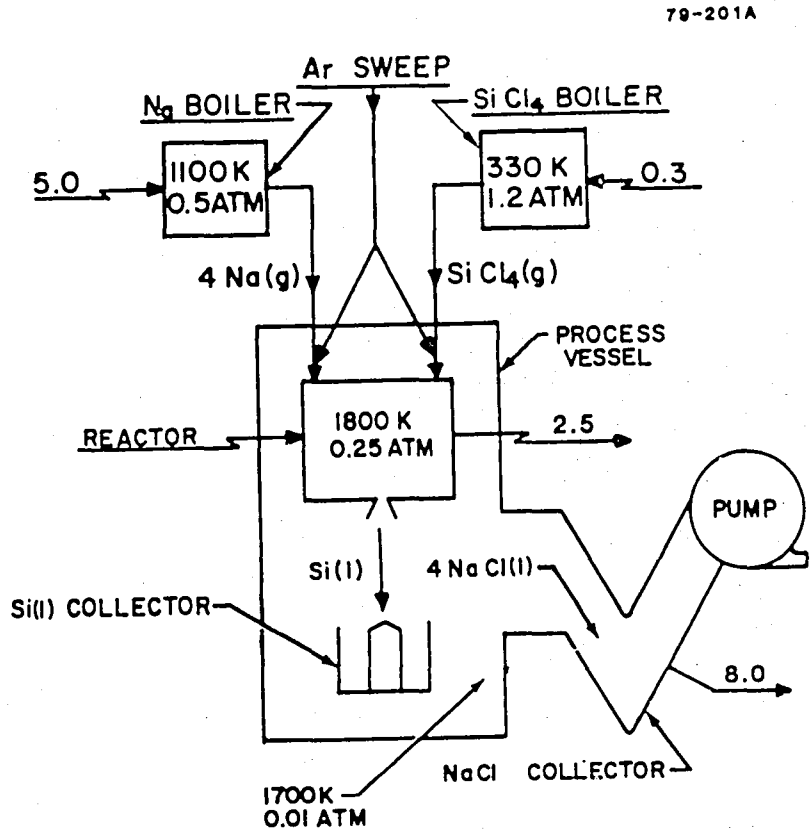


FIGURE 1 ENERGY REQUIREMENTS OF SILICON TEST APPARATUS

Nominal operating conditions used are indicated as well as energy requirements obtained from thermochemical calculations. Energy calculations are in units of kWh per kg of Si produced

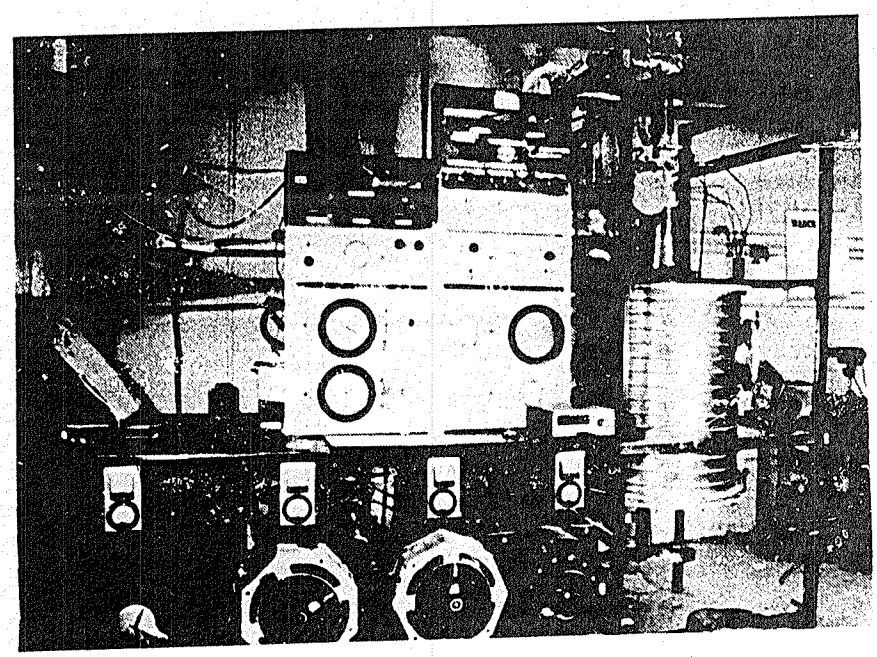

FIGURE 2 OVERVIEW OF NEW SILICON TEST APPARATUS

A schematic diagram of the present silicon test apparatus is shown in Fig. 3. Here, the associated plumbing and pressure monitoring are displayed in an overall fashion. A view of this diagram relates the controls and the reagent vaporizers to the process vessel containing the reactor/crucible assembly. The sodium vaporizer was typically operated at 900°C at 1 atm pressure, while the $SiCl_4$ vaporizer was typically operated at 60°C at 1 atm. The reagents sonically expanded into the reactor heated to 1500°C at 0.25 atm. The crucible portion of the reactor/crucible assembly was kept at 0.02 atm. Since the reagents reacted nearly stoichiometrically little pumping was required to maintain a vacuum once the process vessel was evacuated.

## B. POWER SUPPLIES

The graphite heater rods for the reactor/crucible assembly were each powered by a 7 kVA variable Autotransformer controlling a power transformer (Signal Transformer 56-100) wound to give an output of 200 A at 28 V. An identical power supply was used to power the sodium vaporizer. The power supplies for the $SiCl_4$ vaporizer consisted of 110 V SCR light bulb dimmers.

Prior to a run, the power to each graphite heater rod was gradually increased to 3.2 kW (160 A at 20 V), until the reactor temperature reached 1420-1450°C. The power to the sodium heat pipe was gradually increased to $\approx$ 3.2 kW (120 A at 27 V). One 110 V SCR light dimmer was used for the immersion heater inside the $SiCl_4$ vaporizer. The power output (18 W) was increased to a maximum when the vaporizer was opened to the reactor. A heating tape was also used to maintain the proper temperature on the $SiCl_4$ vaporizer. To prevent any $SiCl_4$ from condensing in the inlet tube to the reactor, an additional heat tape which was controlled by another 110 V SCR light dimmer was used.

## C. REAGENT VAPORIZERS

The use of vaporized reagents results in high adiabatic flame temperatures, above the boiling point of the product alkali metal salt. This technique of introducing the reactants also has the advantage that one may put a distillation stage at the input to the reactor, reducing the impurity concentration in the reactants. Gas-phase alkali metals are not, however, used extensively in the chemical industry and so some work was necessary to develop the needed expertise.

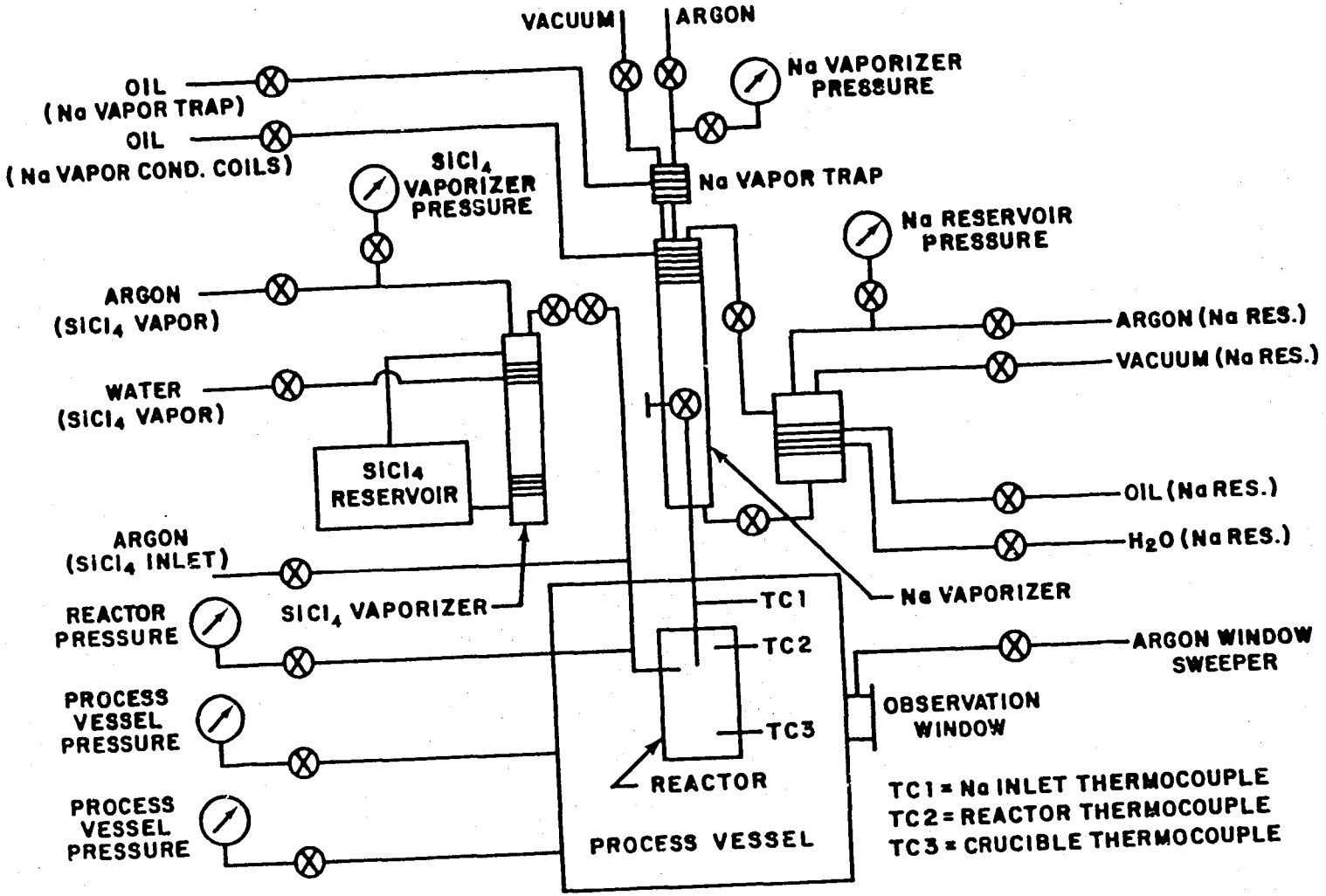


FIGURE 3 SCHEMATIC OF SILICON TEST APPARATUS

The sodium vaporizer shown in Fig. 4 was constructed from 304 stainless steel.[7] The "boiler" was also the sodium reservoir which had a capacity of 0.5 kg. The heating coils were constructed from 1/8 in. diam steel rod. As the sodium vapor rose in the heat pipe a red zone appeared when the stainless steel jacket became hot (≈ 900°C). A blanket of argon maintained the proper pressure (1/2 to 1 atm) above the sodium vapor. Water cooling coils at the top of the vaporizer prevented sodium vapor from entering the argon inlet or the pressure gauge. A tapered stainless steel rod placed in a stainless seat was used to control the entrance of the sodium vapor into the reactor in an on-off fashion. A 0.040 in. diam orifice was used to sonically expand the sodium vapor into the reactor. Erosion of the orifice was prevented by minimizing oxygen or sodium oxide in the vaporizer.

With this sodium vaporizer the silicon test apparatus could only be run for periods of twenty minutes. This limitation was due to the capacity of the sodium vaporizer (≈ 0.5 kg). An attempt to run longer by over-filling the vaporizer resulted in liquid sodium entering the apparatus and promptly destroying many graphite components. Consequently, it became essential to have a vaporizer with a large separate reservoir that could replenish the sodium consumed during operation. Thus, a new large capacity (≈ 3 kg) Na vaporizer was constructed. The larger capacity permitted longer runs (1-2 h) and resulted in larger (0.25-0.5 kg) silicon samples.

A diagram of the new large capacity sodium vaporizer is shown in Fig. 5. The sodium in the 3 kg reservoir was melted or solidified by using hot oil or cold water coils which were silver-soldered to the reservoir. The liquid sodium flowed by gravity through a 3/8 in. diam stainless steel tube into the sodium vaporizer. A pressure equilibrating tube maintained equal pressures in the vaporizer and reservoir during filling. When the valve in the pressure equilibrating tube was closed, the sodium was forced back into the reservoir by pressurizing the heat pipe with argon. The liquid sodium was "valved off" with a cold water coil producing a plug of solid sodium in the vaporizer inlet tube. The valve was opened by melting the solid sodium plug with a hot oil coil.

The new Na vaporizer was similar in design to the previously described vaporizer with two major differences. First, hot oil coils instead of cold water coils condensed the sodium vapor. This prevented clogging by solid sodium since the oil was kept above the Na melting point. Second, the

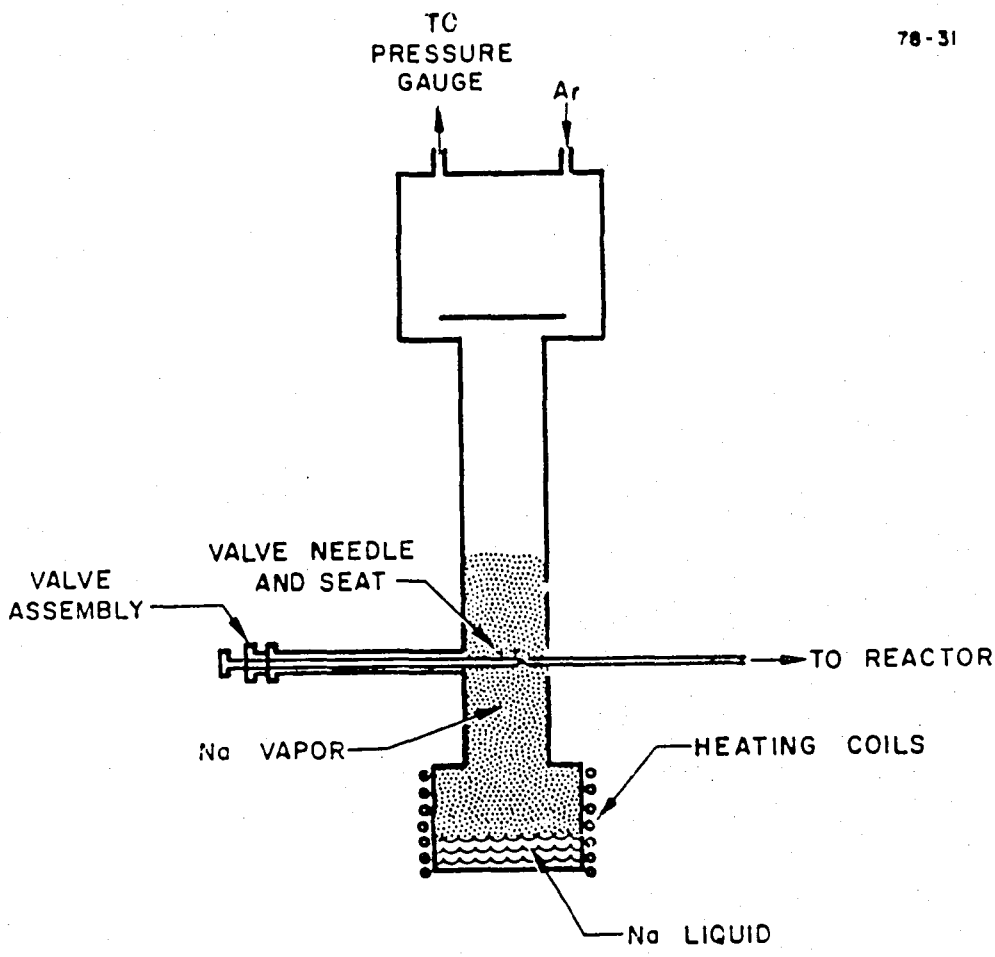


FIGURE 4 SODIUM VAPORIZER

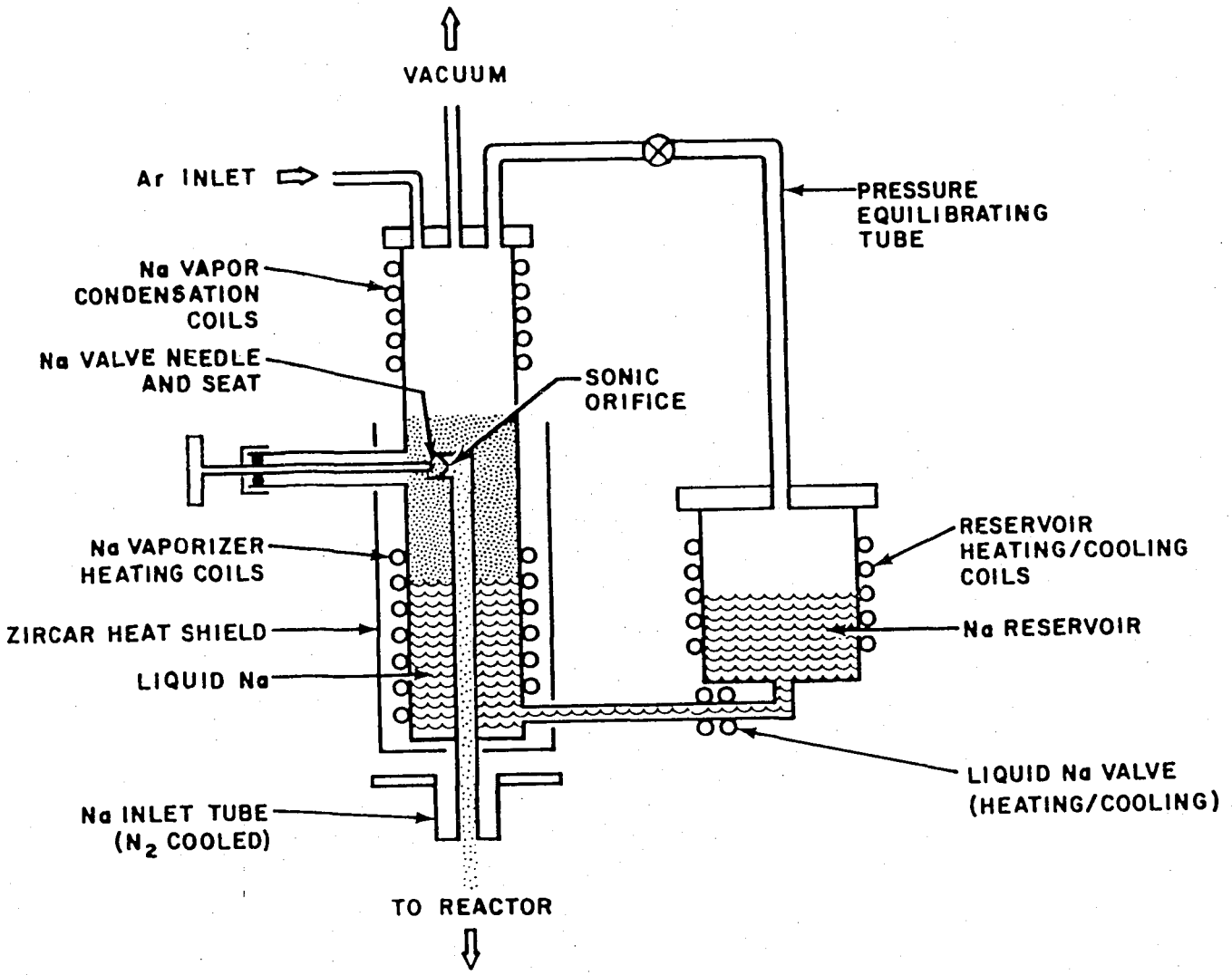


FIGURE 5 NEW SODIUM VAPORIZER

valve needle and seat were inside the vaporizer and were thus surrounded by the Na vapor. This kept the orifice and the inlet tube at the boiling point of Na.

The remaining features of the new large capacity Na vaporizer were identical with only minor modifications. The liquid sodium was vaporized by resistively heating a 3/16 in. diam stainless steel coil. The sodium vapor expanded sonically through a 0.09 in. diam orifice into the Na inlet tube leading to the reactor. Flowing $N_2$ gas prevented melting of the inlet tube and oxidation of the stainless steel heating coil. The vaporizer insulation was made from alumina.

When several small difficulties encountered in initial testing of the new vaporizer were eliminated and safety procedures were developed for handling large quantities of liquid sodium, the system was successfully run for 1 1/4 h. A photograph of the large capacity sodium heat pipe and reservoir before installation is shown in Fig. 6.

Throughout this work the $SiCl_4$ vaporizer remained unchanged. It consisted of a water-cooled stainless steel cylindrical boiler ($\approx$ 2.12 in. diam, $\approx$ 18 in. high) and a 4.5 ℓ stainless steel reservoir. A diagram of the $SiCl_4$ vaporizer is shown in Fig. 7. As in the sodium vaporizer, a blanket of argon was used to control the pressure at which the $SiCl_4$ vapor sonically expanded into the reactor through a 0.125 in. diam orifice. A differential thermocouple reading zero mV difference indicated that the $SiCl_4$ vapor was above the delivery tube exit to the reactor. This vaporizer provided sufficient $SiCl_4$ to run for 1 1/2-2 h.

## D. REACTOR/COLLECTOR ASSEMBLY

Considerable effort was directed toward modification of the heaters for the reactor/collector, the reactor holder through which the reagents enter the reactor, and the reactor/collector assembly. All of the problems associated with these components were overcome and many successful 1 h runs were completed using the new silicon test apparatus.

The reactor/collector assembly was redesigned to minimize heat losses and reduce the number of graphite heaters. Initially, six 1/4 in. diam graphite rods resistively heated the reactor/collector assembly. This arrangement required twelve electrode connections to deliver the necessary power since the reactor and collector were separate units. The final graphite heater arrangement used only three 1/4 in. diam graphite rods to heat both the reactor and the

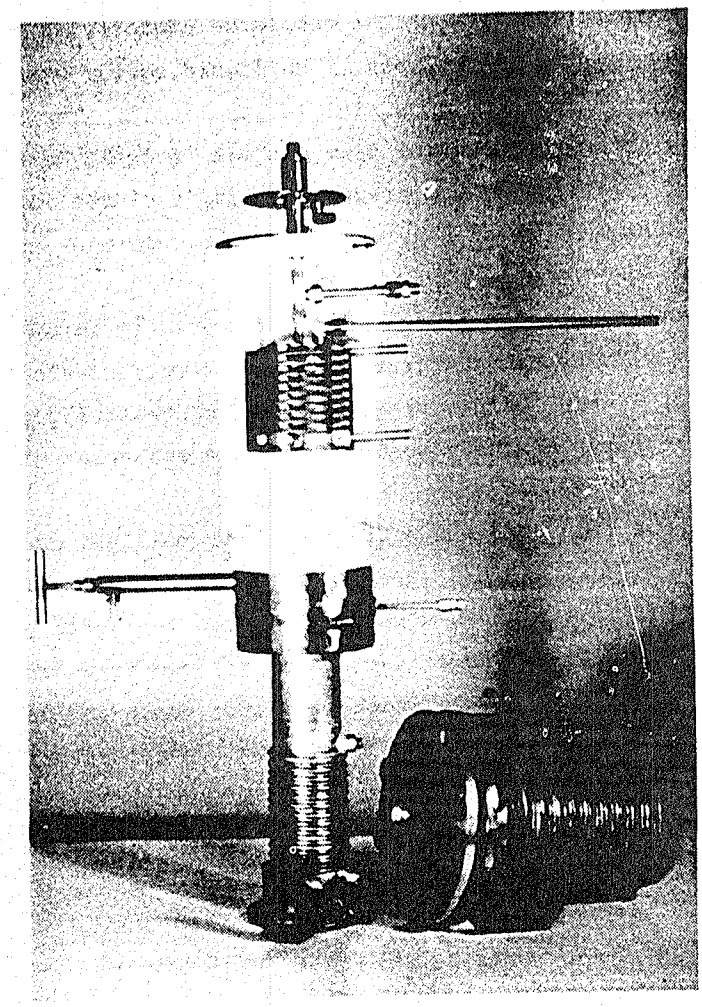

FIGURE 6 LARGE CAPACITY SODIUM HEAT PIPE AND RESERVOIR

79-119

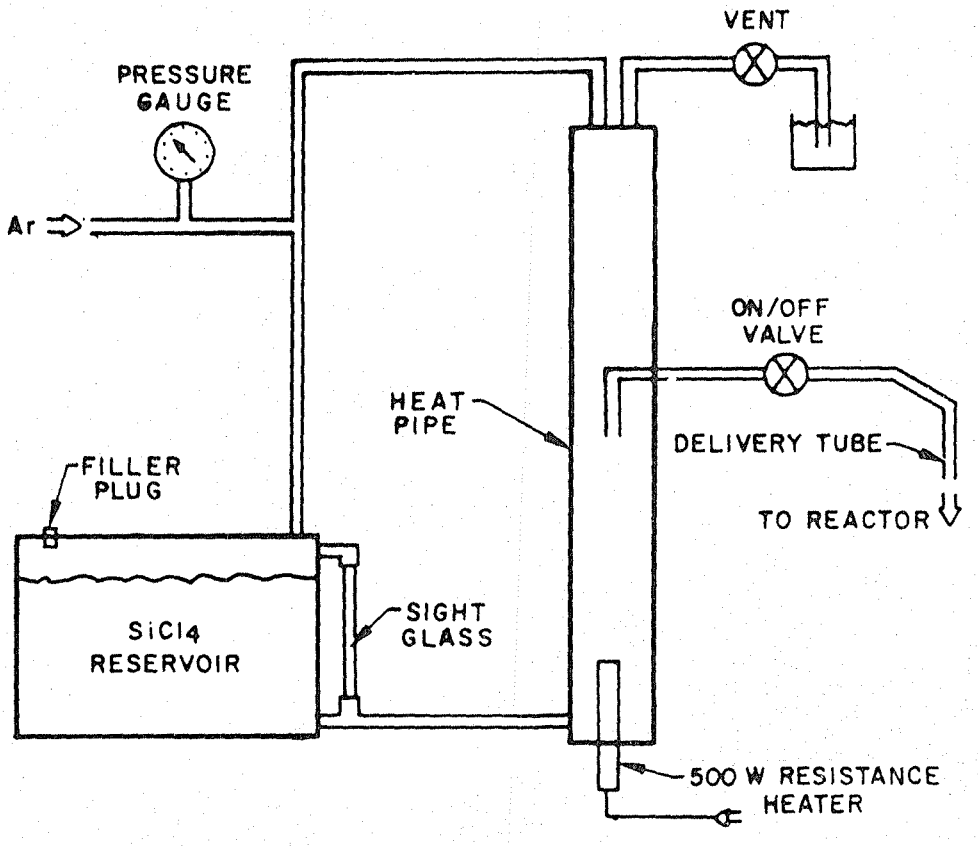


FIGURE 7 $SiCl_4$ VAPORIZER

collector. This reduced the number of electrode connections to three, since the opposite ends of the rods were grounded to the reactor body. To prevent misalignment of the graphite heaters during assembly, the reactor and collector were made as one integrated piece, as shown in Fig. 8. This configuration has several advantages. The heat losses due to radiation were greatly reduced since a large gap no longer existed between the reactor and collector. The power requirements were thus reduced by a factor of nearly two, and temperatures in excess of 1700 K were easily and reliably obtained. In addition, the machining of the assembly was greatly simplified reducing its construction time. A photograph of the final reactor/collector used in these experiments is shown in Fig. 9.

In earlier work, small amounts of liquid sodium often destroyed the graphite reactor holder during a run. This problem was solved by constructing

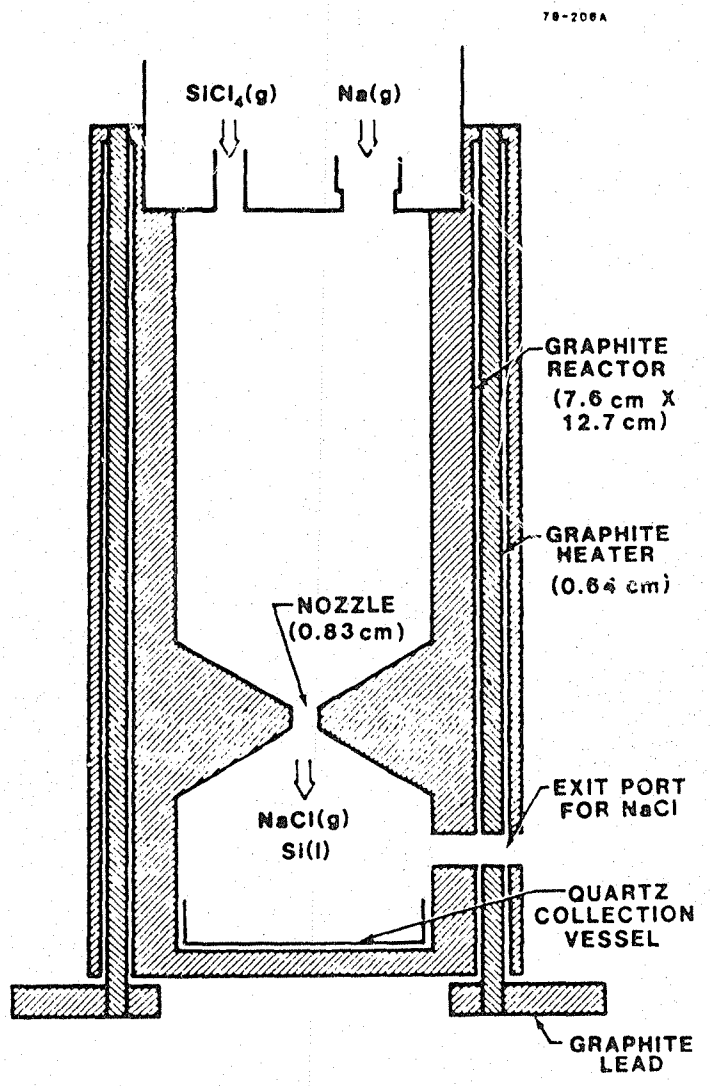


FIGURE 8 NEW THICK WALLED GRAPHITE REACTOR AND COLLECTOR

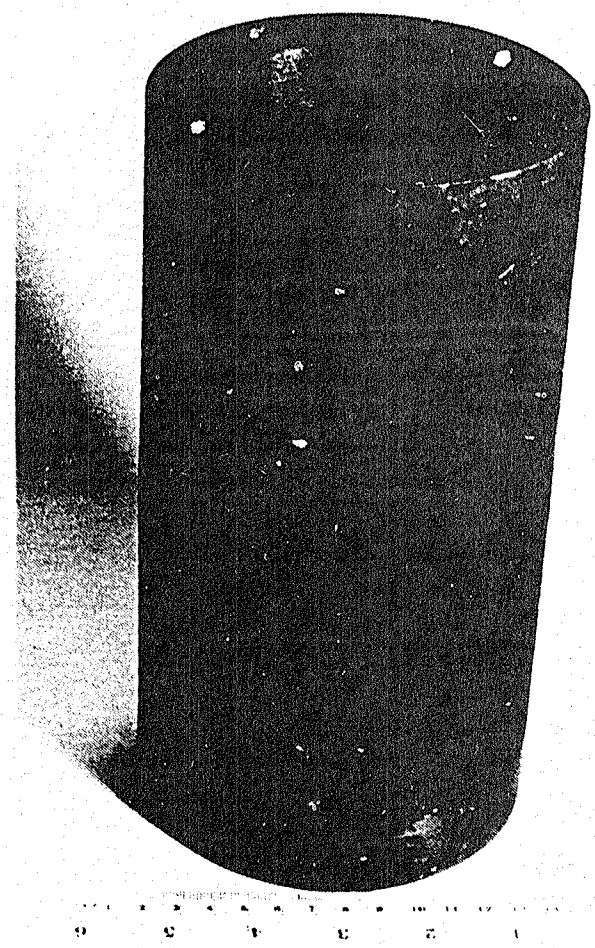

FIGURE 9 PHOTOGRAPH OF REACTOR/COLLECTOR ASSEMBLY

the reactor holder in two pieces. The upper part was made from stainless steel to withstand the attack of sodium, while the lower part was made from graphite to withstand the high temperatures of the reactor. This design (shown in Fig. 10) was successfully employed for several twenty minute runs with the silicon test apparatus.

Initially, the double-walled sodium inlet tube was made completely from stainless steel. Since this required careful regulation of the $N_2$ cooling to prevent the stainless steel from melting, the new inlet tube was constructed of nickel and Inconel as shown in Fig. 10. Since the outer wall of the inlet tube was nickel (m.p. $\approx$ 1750 K) it could withstand higher temperatures than stainless steel. It also had a much higher heat conductivity which served to minimize hot spots. This design was successfully used for several twenty minute runs without failure.

In some of the one hour runs with the silicon test apparatus, the reagent inlet section of the reactor holder was modified slightly. Only the

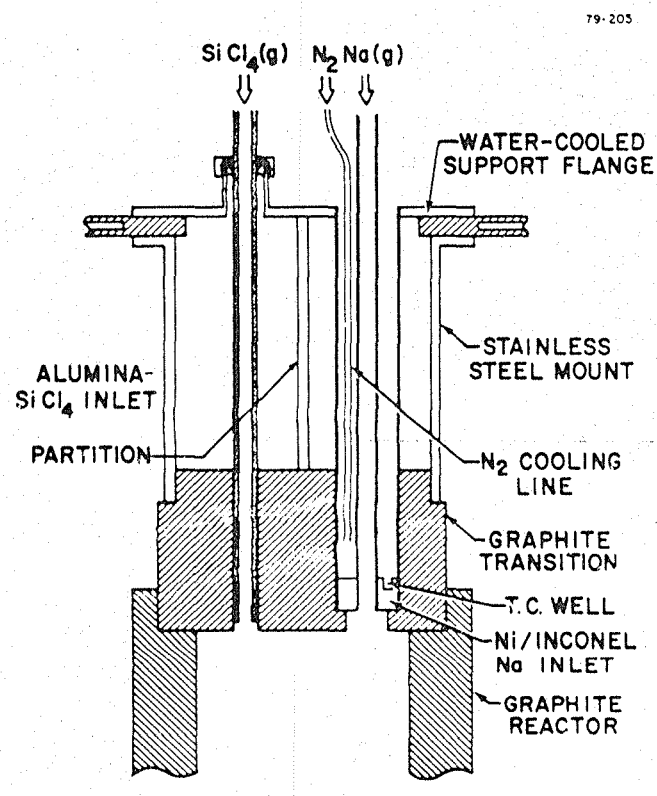


FIGURE 10 REACTOR HOLDER AND REAGENT INLET ASSEMBLY

sodium entered from the top and the need to partition the reagent inlets was eliminated. The $SiCl_4$ reagent then entered the side of the reactor through an alumina tube to intersect the sodium vapor at right angles. This reagent inlet design presumably increased the mixing of the reagents. Furthermore, the construction of the reactor holder was greatly simplified. No noticeable differences in the performance of the apparatus occurred when this modification was implemented. This was taken to indicate that good reactant mixing was achieved with either inlet arrangement.

The final arrangement of the reactor/collector in the process vessel is shown in Fig. 11. Not shown in Fig. 11 is the $SiCl_4$ reagent entry at right angles. The large stainless steel tank was water cooled and was sealed with an "O-ring" pressing on the top aluminum flange. The process vessel was lowered by a cable connection attached through pulleys to a counterweight. In this manner, assembly of the reactor/holder components was facilitated. Visual observation of the reaction jet was made through holes in the side of the reactor assembly (shown in Fig. 11). These holes also served as exit ports for the salt vapor, leaving the condensed silicon inside the crucible. Although not constructed during this contract, a series of baffles could be used to condense the salt and prevent its deposition onto the walls of the process vessel.

## E. MATERIALS STUDY

Several attempts were made to collect large samples of silicon as cast ingots. The failure of the collector materials used as collection vessels frustrated these attempts initially. Quartz collection dishes withstand the attack by silicon but either the $SiCl_4$, NaCl, or Na attacks the quartz dish at temperatures of 1700 K. To investigate alternative crucible materials, samples of sintered SiC (from Carborundum Co.) were placed in the Na vaporizer, reactor chamber, and collection vessel. All samples remained completely unchanged. Thus, sintered SiC may prove to be a suitable material for the reactor/collector assembly.

Several other alternative materials were tested as collection crucibles for the silicon product. A tantalum dish at 1800 K was completely destroyed during a twenty minute run and no silicon was collected. Using an alumina crucible at 1650 K, it was possible to successfully collect the silicon. Crucibles made from POCO DFP1 graphite, which the manufacturer reputes

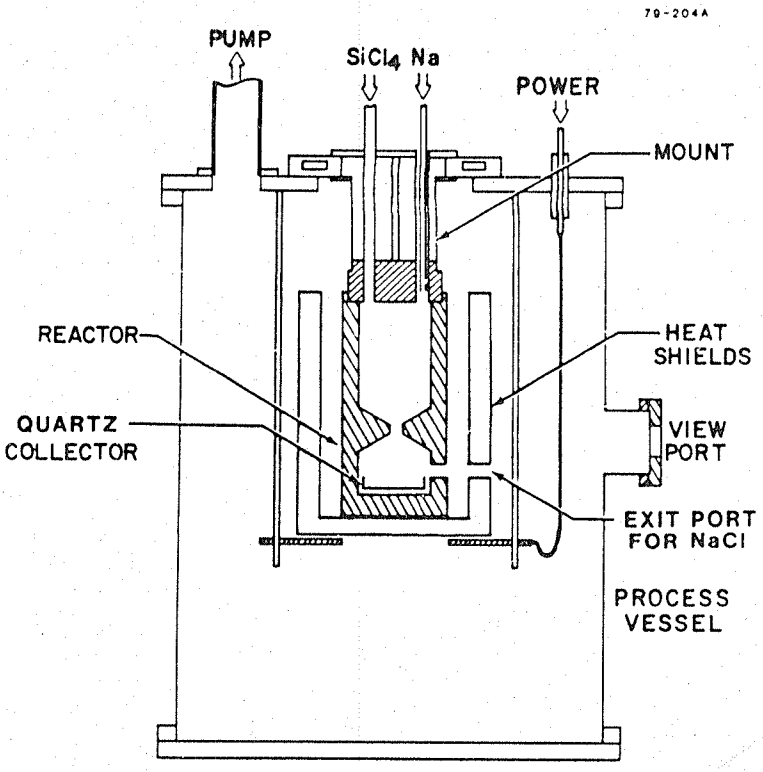


FIGURE 11 PROCESS VESSEL CONTAINING THE REACTOR/COLLECTOR

to be highly impervious, did not contain the silicon at 1800 K. However, at 1650 K no silicon was observed to penetrate the POCO DFP1 graphite and a consolidated ingot was obtained.

The penetration of silicon into the crucible collector was also prevented by applying a paint of UCAR-14 cement resin diluted with methylethylketone.[8] After drying in an oven for several hours, the crucible was heated to 1500 K in a vacuum. Silane was then introduced and a silicon coating was deposited when the silane came in contact with the hot crucible. The crucible treated in this manner prevented penetration by molten silicon collected during a run.

## IV. REAGENT FLOW RATE MEASUREMENTS

To ensure that the silicon reactor was operating near stoichiometry, the reagent flow rates were measured for simulated (no reaction taking place) and actual running conditions. For the production of 0.5 kg $h^{-1}$ Si, the $SiCl_4$

flow rate must be 0.84 g $s^{-1}$ and the Na flow rate must be 0.46 g $s^{-1}$. The $SiCl_4$ flow rate was measured by monitoring the volume loss in the $SiCl_4$ heat pipe reservoir. These volume measurements were accurate to within 1%. The sodium flow rate was measured by simple weight loss of the sodium vaporizer ( ≈ 5 kg) which can be weighed to within 0.01% uncertainty, but oxidation during heating, and sodium leakage at the valve resulted in a ≈ 5% uncertainty in the Na flow rate.

No reaction took place during the simulated run, and each reagent flow rate was separately measured. The operating conditions were 12 psig in the $SiCl_4$ vaporizer with a 0.041 in. diam orifice and 0.5 atm pressure in the Na vaporizer having a 0.125 in. diam orifice. Both reagents expanded sonically into the process vessel held at a pressure of 0.1 Torr. During actual runs, these operating conditions cannot be kept perfectly constant because of pressure and temperature variations as the reagents are depleted. The results of the simulated runs gave flow rates of 0.72 g $s^{-1}$ for $SiCl_4$ and 0.5 g $s^{-1}$ for Na. This is a $Na/SiCl_4$ molar ratio of 5.5 (4 is stoichiometric). However, for three actual runs, the Na flow rate measured 0.36 ± 0.04 g $s^{-1}$ and the $SiCl_4$ flow rate measured 0.72 ± 0.03 g $s^{-1}$. This corresponds to a $Na/SiCl_4$ molar ratio of 3.7, a nearly stoichiometric ratio slightly rich in $SiCl_4$.

For all of the reactor variations tested, both the mixing and reaction appeared to be completed within the confines of the 0.58 ℓ reactor assembly. Otherwise, molecular chemiluminescence or Na* emission would have been observed outside the immediate vicinity of the collection vessel. Other evidence for the completeness of the reaction is that the process vessel pressure did not increase with the vacuum pump shut off.

## V. SILICON SEPARATION/COLLECTION EFFICIENCY

The basis for continuous product separation is that the alkali metal salt exits as a gas from the reaction chamber while the silicon product is present as a condensed phase. As the products exit from the reactor nozzle, a shock wave is formed upon impaction in the collecting crucible kept at a temperature near 1700 K. The salt vapor flows away from the crucible, leaving the condensed silicon behind.

Calculations using the Air Force Rocket Propulsion Laboratory ISP Computer Code[3] for the reaction of Na with $SiCl_4$ show that for an isothermal approximation in the reactor at 1800 K, 98% of the silicon is formed as a liquid. Upon expansion (supersonic flows) from ≈ 0.5 atm to 0.01 atm an additional 1% of silicon appears in the condensed phase. However, this 1% gain is then lost by heating due to the formation of a shock wave upon impaction. Because 98-99% of the silicon is formed in the condensed phase in the post-flame region and very large pressure drops are available for the impaction process, we anticipated that the collection efficiency should be high. An interesting result of these calculations is that a mixture of solid and liquid silicon exists in the post-shock region. Indeed, this is experimentally observed. The results of these computations are given in Fig. 12 which shows the details of the impaction-separation process.

Experimental separation and collection studies were initiated as the silicon test apparatus was being improved. The early runs were often terminated after a few minutes because of failures in the sodium inlet tube or the reactor holder. However, significant experimental results were obtained as the silicon test apparatus was brought to its final upgraded stage by testing new designs and modifications.

The first few runs with the silicon test apparatus prior to changes in the reactor/collector design produced small conical ingots of metallic silicon. Only 3 to 4 g samples could be collected because of failures of the sodium inlet tube. These samples were nevertheless significant because they demonstrated complete separation of the products. An important discovery was that the silicon product appeared as a slush-like material which froze into a solid ingot at a crucible temperature of 1500 K. Upon slicing the ingot with a diamond saw, no powdered silicon or salt byproduct could be seen. It was also significant that this silicon-slush did not appear to penetrate into the graphite.

After redesigning the sodium inlet, the silicon test apparatus could be run for twenty to thirty minutes. This time was determined only by the 500 g capacity of the original sodium heat pipe. The first tweny minute run produced a large conical mound of silicon powder mixed with consolidated metallic silicon. This type of mixture apparently resulted because the temperature of the crucible was below 1500 K. Subsequent twenty minute runs were made with the improved reactor/crucible design. During these runs, small (10-40 g) samples

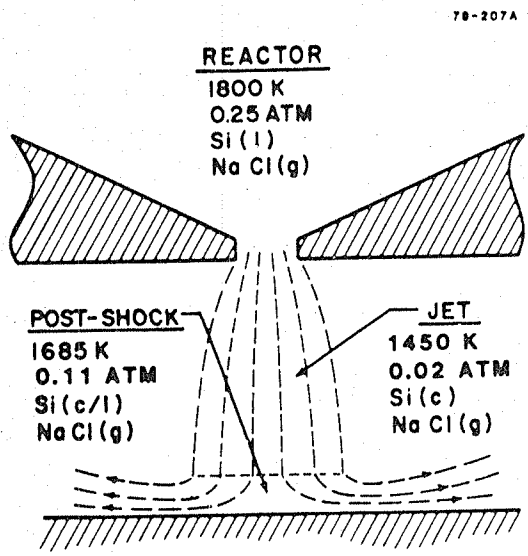


FIGURE 12 IMPACTION SEPARATOR FOR SILICON AND SALT PRODUCTS

of metallic, fused silicon were collected (a total of 120 g was produced). However, most of the silicon product soaked into the untreated graphite reactor assembly which then cracked upon cooling. Although this prevented the collection of consolidated ingots, collection efficiencies could be measured and 10-30% were measured routinely.

In order to calculate the collection efficiencies, after the runs the weight of Na and $SiCl_4$ consumed and the weight of the silicon produced were measured. The efficiency of the collection process was determined by computing the ratio of the actual Si collected to the total weight of Si produced.* At temperatures 50-100 K above the melting point of silicon ($\approx$1690 K) nearly all of the silicon produced was deposited with the salt byproduct on the walls of the process vessel, i.e., virtually no product separation occurred. At temperatures slightly above the melting point of silicon, the collection efficiencies measured $\approx$ 30 to 40%. At temperatures at or slightly below the melting point of silicon, the collection efficiencies measured 60 to 80%. The highest efficiencies measured, including the 1 1/4 h run, were 82%. All of these efficiencies were measured in runs using a simple pedestal impactor in the

* In each run some of the silicon produced soaked into the graphite reactor. This silicon was counted as collected silicon.

collection crucible. The above observations indicate that the collection efficiency is a strong function of collector temperature. However, the exact conditions which provide a high collection efficiency were not determined in this contract.

One explanation that could account for the temperature dependence of the collection efficiency is that the silicon aerosol particulates coalesce and increase in size near the impactor surface which is at a temperature below the melting point of silicon. These larger aerosol particles then aggregate upon impaction into a silicon mass more easily than smaller particles. The formation of the larger silicon particles is similar to the formation of fog when warm air passes over a cold surface and the silicon mass is analogous to the formation of "ice feathers" which grow toward the wind at very cold temperatures during winter months. A photograph of the jet is shown in Fig. 13a and an ingot growing into the jet is shown in Fig. 13b.

Other factors such as collector geometry, collector-nozzle exit distance, and nozzle diameter could also be important in optimizing the collection efficiency. A systematic study of the effects of each of these parameters would be valuable but was well beyond the scope of this program. Furthermore, since high separation efficiencies were obtained regularly, there was less urgency in finding ways of further improving the efficiency, and research in other problem areas (purity and long run times) was emphasized in the remainder of the program.

## A. PRODUCT CHARACTERIZATION

Because we obtained large samples of silicon, it was possible to begin to characterize and evaluate the silicon product as a potential solar grade feedstock material. The silicon obtained was analyzed and evaluated with respect to its crystalline nature, electrical properties, and purity. These results are presented here.

The silicon obtained by the AeroChem process appeared as a consolidated polycrystalline mass. One silicon ingot was sliced into 1 in. diam wafers using a diamond saw. Microscopic examination of the wafers after polishing and etching revealed irregularly shaped crystals of silicon that were often several mm long. Several small (0.3 mm) triangular faces of {111} planes of single crystals were identified. On one ingot two hexagonal shaped faces of single crystals were observed. The length of a diagonal in these hexagons measured $\approx 4$ mm.

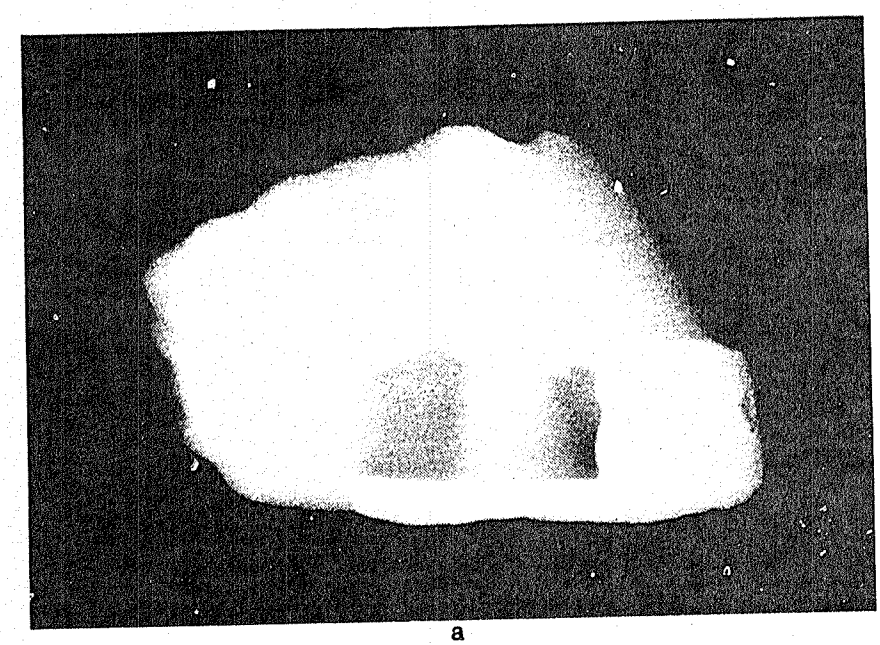

a

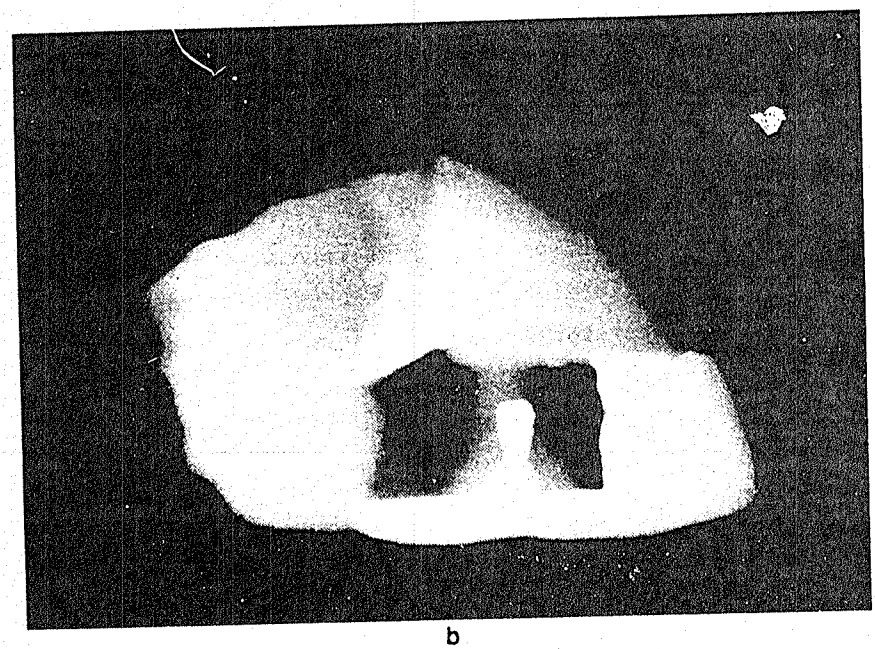

b

FIGURE 13 JET EXITING FROM REACTOR NOZZLE (a)
AND SILICON INGOT GROWING INTO JET (b)

Figure 14 clearly shows the difference in the nature of the silicon product collected at two different temperatures. Figure 14a shows that at the proper collector temperature ( $>$ 1500 K) polycrystalline silicon ingots were collected with high efficiency ( $\approx$ 80%). However, Fig. 14b shows that at very low collector temperatures ($\leq$ 1500 K), a poorly separated amorphous silicon powder mixed with salt was obtained.

The resistivity of the polished and etched wafers, as measured by the four probe resistivity technique, varied from values of several hundred Ω-cm to $\approx$ 1000 Ω-cm. These resistivity values may have some meaning in spite of the polycrystalline nature of the silicon since the resistivity was lowered to less than 10 Ω-cm by doping one of the wafers with boron. The silicon material was found to be p-type using the hot probe technique. This result is consistent with the 3 ppma impurity level of Al found in this particular sample of silicon.

## B. PURITY OF SILICON PRODUCT

During the latter part of this contract, efforts were directed toward the analysis of the silicon product. Only optical emission has been used thus far to characterize the silicon product. Results were obtained from Princeton Testing Laboratories (PTL) and from Lawrence Livermore Laboratories (LLL). The local testing laboratory analyzed silicon samples obtained early in the program in three to twenty minute runs. After the large capacity sodium source was installed and one hour runs were initiated, samples were sent to Lawrence Livermore Laboratories since their sensitivity is greater than that of the local laboratory. Sodium analyses from both laboratories are presented.

Princeton Testing Laboratories discovered product contamination due to crushing of the sample. This result is similar to that found by Battelle Columbus Laboratories,[8] i.e., semiconductor grade silicon became contaminated with thousands of ppma impurities during the crushing operation. The analyses of silicon samples obtained in the final portion of this contract were performed by Lawrence Livermore and a 1 mil etch was used to remove any possible contamination of the samples due to crushing.

A comparison of the analysis performed by PTL for three silicon samples is given in Table I. The three minute run contained large amounts (several hundred ppma) of impurities. However, the two twenty minute runs

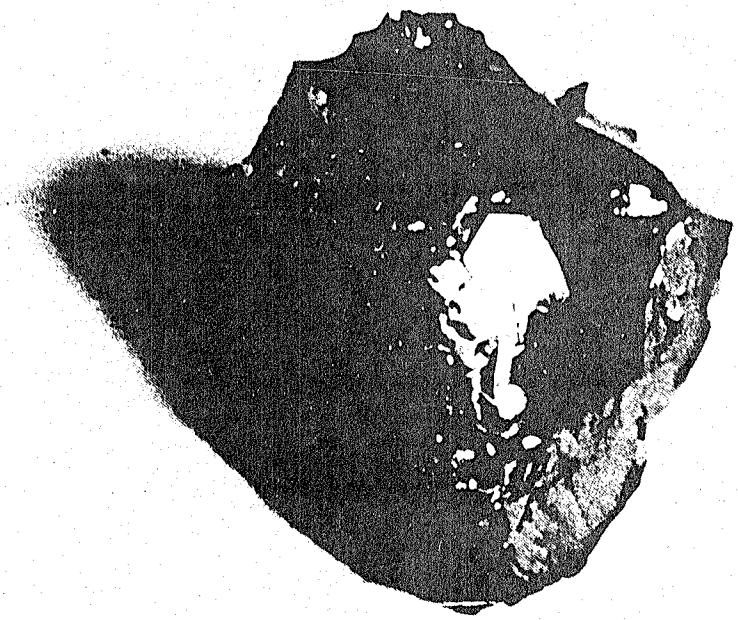

a

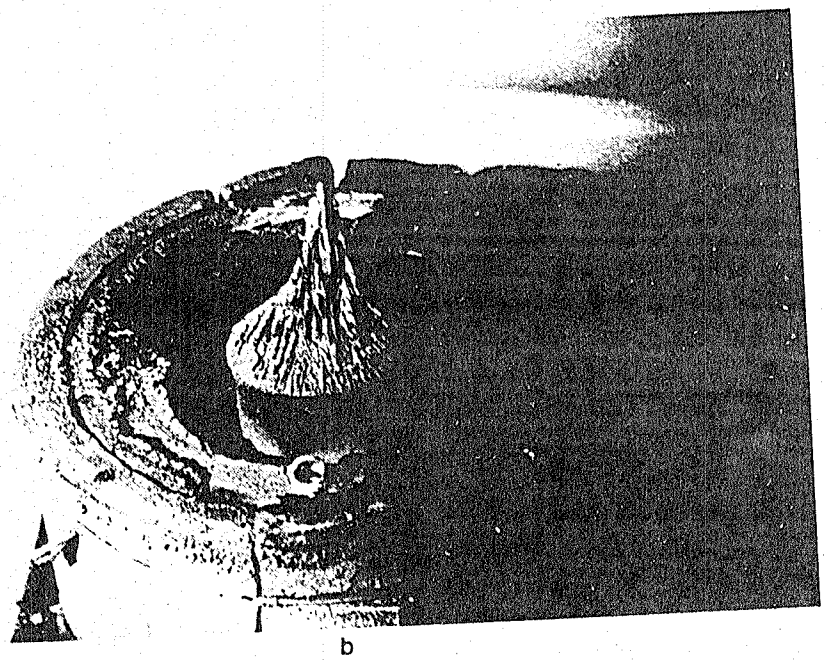

b

FIGURE 14 POLYCRYSTALLINE SILICON INGOT (a)
AND POLYCRYSTALLINE SILICON POWDER (b)

TABLE I

EMISSION SPECTROGRAPHIC ANALYSIS (PRINCETON TESTING LABORATORIES) OF SILICON SAMPLES

| Element | 20 min Run (Graphite Dish) Impurity Conc. ppma | 20 min Run (Alumina Dish) Impurity Conc. ppma | 3 min Run Impurity Conc. ppma | Detection Limit (min. conc.) ppma |
|---|---|---|---|---|
| Ag | < 0.3 | < 0.3 | 1-3 | 0.3 |
| Al | nd | 3 | 200 | 1 |
| As | nd | nd | nd | 112 |
| B | < 26 | nd | 26 | 26 |
| Ba | nd | nd | nd | 61 |
| Be | nd | nd | nd | 31 |
| Bi | nd | nd | nd | 1 |
| Ca | nd | nd | 70 | 1 |
| Cd | nd | nd | nd | 8 |
| Co | nd | nd | nd | 5 |
| Cr | nd | nd | 81 | 5 |
| Cu | < 0.4 | nd | 66 | 0.4 |
| Fe | 3 | nd | 75 | 5 |
| Ga | nd | nd | nd | 4 |
| Ge | nd | nd | nd | 4 |
| In | nd | nd | nd | |
| Mg | < 1 | 1-12 | 93 | 12 |
| Mn | < 5 | nd | nd | 5 |
| Mo | < 3 | nd | nd | 3 |
| Na | nd (12)[a] | nd (12)[a] | 609 | 360(6)[a] |
| Ni | nd | nd | 475 | 5 |
| P | nd | nd | nd | 90 |
| Pb | nd | nd | nd | 4 |
| Sb | nd | nd | nd | 23 |
| Sn | nd | nd | nd | 2 |
| Ti | nd | nd | nd | 6 |
| V | nd | nd | nd | 6 |
| Zn | nd | nd | nd | 43 |
| Zr | nd | nd | nd | 3 |

[a] Plasma emission spectroscopic analysis gave 9-12 ppma Na for these runs with a detection limit of 6 ppma.

showed a substantial decrease in the impurities. For the twenty minute run using an alumina collecting dish, the silicon product contained only 1-12 ppma Mg, 3 ppma Al, and less than 0.3 ppma Ag. All other impurities were below the detection limit for emission spectroscopy. The run using the graphite (Stackpole 2020) collection dish contained Ag, Cu, Fe, Mg, Mn, and Mo, all at levels lower than 10 ppma. Thus, it was anticipated that the one hour runs would reduce the impurities even further.

The analytical results obtained by the Lawrence Livermore Laboratories for the silicon samples obtained during one hour runs are given in Table II. The runs producing the analyzed samples were very similar. The major differences were in the choice of collector material. For the 4/10 and 4/25 runs Stackpole 2020 graphite crucible collectors with pedestal separators were used. For the 5/12 run a high purity Poco graphite collector was used. The collectors for the 4/18 and 4/22 runs were shallow, 100 $cm^3$ Coors alumina dishes. Another difference in the runs was that a molybdenum tube was used in the first four runs to line the sodium inlet to the reactor. The downstream end of this tube was eaten away during this series and this is believed to account for the high, but decreasing, levels of Mo in the samples. This tube was subsequently replaced by graphite in the 5/12 run.

To adequately discuss the possible source of contamination some knowledge of the impurity levels in the reactant and construction materials should be known. Table III shows analyses of the silicon tetrachloride and sodium used in these runs as well as typical analyses of 304 stainless steel which is a major construction material for the current apparatus. The reactor material is Stackpole 2020 graphite. Manufacturer's literature indicates this material to have about 1500 ppm "ash content".

While the source of Mo contamination is clear, the sources of other impurities are not obvious from the analyses. Volatile impurities such as As, Cd, P, Pb, Sr, and Zn appear to be a function of collector material and may tend to leach or evaporate from the graphite into the silicon. Use of high quality graphite would minimize this. All the elements listed except Na have moderately or highly volatile chlorides which could accompany the $SiCl_4$. The $SiCl_4$ is relatively pure as delivered, but is allowed to sit in a stainless steel reservoir for several hours before the run starts. This may result in leaching of many impurities (particularly As, B, P. and the transition metals) from the reservoir. Since some misting of the boiling $SiCl_4$ during the run is

TABLE II

PLASMA EMISSION SPECTROSCOPY ANALYSIS (LAWRENCE LIVERMORE LABORATORIES) OF SILICON SAMPLES

| | Concentration, ppma | | | | | |
|---|---|---|---|---|---|---|
| Element[a] | 4/10 Run[b] | 4/18 Run[b] | 4/22 Run[b] | 4/25 Run[b] | 5/12 Run | Best Value |
| Al | 8.7 | 2.8 | 7.1 | 1.7 | 0.8 | 0.8 |
| As | 0.7 | < 0.1 | 0.05 | 0.4 | < 0.2 | < 0.2 |
| B[c] | 2.1 | 6.5 | 4.8 | 12. | < 0.1 | < 0.1 |
| Ca | 0.2 | < 0.4 | 1.3 | 0.5 | 3.4 | < 0.4 |
| Cd | 0.1 | < 0.03 | 0.005 | 0.1 | < 0.001 | < 0.001 |
| Co | 0.3 | < 0.06 | 0.02 | 0.2 | 0.02 | 0.02 |
| Cu | 0.5 | 0.3 | 0.9 | 0.03 | 12. | 0.03 |
| Fe | 13.8 | 10.2 | 7.1 | 0.5 | 2.7 | 0.5 |
| Li | 0.1 | < 0.04 | < 0.04 | < 0.04 | < 0.03 | < 0.03 |
| Mn | 1.9 | 0.8 | 1.0 | 0.06 | 0.4 | 0.06 |
| Mg | 0.6 | < 0.7 | 1.0 | < 0.5 | < 0.5 | < 0.5 |
| Mo | > 400. | 12. | 16. | 0.5 | 4.6 | 0.5 |
| Na | 5.8 | 66. | 7.5 | 12. | 260. | 5.8 |
| Ni | 11. | 0.3 | 0.4 | 0.2 | 0.8 | 0.2 |
| P | 7.2 | < 2. | < 1. | < 5. | < 1.5 | < 1. |
| Pb | 0.6 | 0.13 | 0.03 | 0.8 | 0.3 | 0.03 |
| Se | 1.0 | < 0.3 | < 0.2 | 0.4 | < 0.2 | < 0.2 |
| Sr | < 0.02 | < 0.02 | < 0.02 | < 0.02 | 0.1 | < 0.02 |
| Ti | 0.7 | 0.02 | 0.1 | 0.03 | 0.1 | 0.02 |
| V | 0.8 | 0.04 | 0.1 | 0.02 | 0.03 | 0.02 |
| Zn | 0.03 | 0.007 | 0.1 | 0.02 | 3.5 | 0.007 |

[a] K not detected.

[b] Average of 3 analyses.

[c] Boron concentration is a lower limit. The analytical method results in some leaching of boron from the sample.

TABLE III

COMPOSITION OF REACTANT AND CONSTRUCTION MATERIALS

Silicon Tetrachloride, CP Grade[a]

| | |
|---|---|
| B | 0.09 |
| Fe | 0.31 |
| P | 0.08 |
| Ti | 0.35 |
| V | 0.27 |

Sodium, Commercial Grade[b]

| | |
|---|---|
| B | 2.1 |
| Ca | 170. |
| K | 210. |

304 Stainless Steel[c]

| Cr, Fe, Ni | Principal |
|---|---|
| C | 450. |
| Co | 700. |
| Mn | 1740. |
| P | 230. |
| S | 70. |

[a] Concentrations in (atoms of impurity)/($10^6$ atoms of silicon)

[b] Concentrations in (atoms of impurity)/($10^6$ atoms of sodium)

[c] Concentrations in ppm (wt)

inevitable and the reflux column is not packed to prevent this, non-volatile chlorides could be delivered to the reactor. Misting of the sodium also undoubtedly occurs and in fact during the initial stages of the runs, reactor pressure pulses are observed which are attributed to the delivery of sodium droplets. Delivery of liquid sodium could result in the transfer of stainless steel components as well as boron and other non-volatile impurities in the sodium.

Because the purity of surfaces of our ingots might be adversely affected by startup and shutdown, we suggested a longer etch to LLL. However, analyses of samples before and after etching showed no systematic differences in purity levels. Also the use of various types of graphite and alumina collectors did not seem to affect purity in any discernible systematic way.

Since sodium is used to produce the silicon product in the AeroChem process, the samples were subjected to more analyses by plasma emission spectroscopy. Table IV shows the results of sodium analysis for several silicon samples. The sodium levels were $\approx$ 12 ppma or less. This is a significant improvement from the 600 ppma level found in the three minute run. The testing laboratory (PTL) performing the analysis believes that the sodium level is most likely not from the silicon sample itself but from ever-present contamination sources even during careful analysis. Thus, residual amounts of sodium in the silicon product do not appear to be a problem in the AeroChem process.

It had been anticipated that the product separation process would also be a purification process. For boron, it was expected that at least a factor of 20 could be obtained in the silicon product.[7] It was possible to determine some of the purification factors for some of the elements existing as impurities in silicon. We define the purification factor (Cp) in a manner very similar to segregation coefficients,[9] i.e.,

$$Cp = \frac{[V]}{[S]}$$

where [V] is the impurity concentration in the vapor phases (for both Si and NaCl) and [S] is the impurity concentration in the collected silicon (samples). The impurities in the vapor phase [V] were measured by collecting an unseparated sample of NaCl and Si products after condensation while the impurities in the solid phase are taken from Table II. The results of these measurements are given in Table V. As can be readily seen, the impaction separation process

TABLE IV

SODIUM ANALYSES OF SILICON PRODUCT

| Run | Collector Material[a] | Na Conc. (ppma) Princeton Testing Lab. | Na Conc. (ppma) Lawrence Livermore Lab.[b] |
|---|---|---|---|
| 3/4/80 | Alumina | 12 | --- |
| 3/6/80 | Graphite | 10.7 | --- |
| 4/10/80 | Graphite | 4.4 | 3.9 |
| 4/18/80 | Alumina | 12 | 19.7 |
| 4/22/80 | Alumina | 9.9 | 20.7 |
| 4/25/80 | Graphite | --- | 30.4 |

[a] All alumina collectors are Coors and all graphite collectors are Stackpole 2020 except the 4/10/80 run which is POCO DFP1.

[b] These numbers are based on LLL analysis of 5/20/80. The results presented in Table II are an average of three analyses.

TABLE V

TYPICAL PURIFICATION COEFFICIENTS

FOR JET IMPACTION PROCESS

| Element | Vapor Phase[a] Impurity Conc. ppma | Solid Phase[b] Impurity Conc. ppma | Cp[c] |
|---|---|---|---|
| Ca | 70 | < 0.4 | 200 |
| Mn | 50 | 0.06 | 800 |
| Fe | 500 | 0.5 | 1000 |
| Al | 200 | 0.8 | 300 |
| Mo | 3 | 0.5 | 6 |
| Cu | 130 | 0.03 | 4000 |

[a] Vapor phase impurities were obtained from the analysis of an unseparated silicon-salt mixture which was collected as a solid.

[b] The values are taken from Table II from the column listed "best".

[c] Cp = conc. in vapor/conc. in solid.

often purified the silicon by a factor of 100-1000. This is a significant result since it demonstrates that our separation/collection process is also a purification process. It should be emphasized that this process was not optimized and could be a potentially powerful purification technique.

No changes were made in the silicon test apparatus before producing samples for submission to JPL for evaluation. Thus, the first cut of samples produced by the AeroChem process show (1) no significant contamination by the Na reagent, (2) metal impurities sufficiently low that they would not affect solar cell performance for silicon purified by the Czchrolski technique for growing single crystals, and (3) only B and P remain at levels which may be detrimental to solar cell performance during some runs.

In summary, when one considers the multitude of potential impurity sources, the rather crude state of operation of the reactant vaporizers, and the limitation of run times to less than 90 min, the impurity levels are surprisingly low. Several of the samples produced are of "solar grade" quality (assuming additional purification in a subsequent processing step, e.g., single crystal growth). It is quite reasonable to expect, in fact, that refinements in the process would reduce impurities by factors greater than $10^3$ resulting in semiconductor grade product.

## VI. ENGINEERING AND ECONOMIC ANALYSES

This section presents a preliminary economic and engineering analysis for the AeroChem process. The cost estimate for production of silicon is \$10.18 $kg^{-1}$ silicon. The analysis presented here follows closely the analysis of the Battelle process given by Dr. Carl Yaws at the 13th JPL Project Integration Meeting (see also Ref. 10). The cost estimate determined for the AeroChem process is based on the following:

(i) The costs are for a 1000 MT $yr^{-1}$ demonstration plant.

(ii) The costs are in terms of 1975 dollars. To arrive at 1980 dollars, the 1975 dollars are multiplied by 1.4.

(iii) Prices for raw materials are taken from the January 1975 Chemical Reporter.

(iv) Labor costs and utilities rates are those used in Yaws' Battelle process analysis (Ref. 10).

(v) Other items for obtaining the cost per kg of silicon are based on the basic costs and are obtained using Yaws' multiplication factors.

(vi) Finally, the cost of major equipment at the present time depends heavily on comparison with similar equipment used in the Battelle process. Scaling of equipment costs is done using a 0.6 exponent. Major uncertainties at this time lie in the estimation of costs of some of these items, particularly the reactors.

The AeroChem process consists of (i) purification and vaporization of $SiCl_4$, (ii) vaporization of sodium metal, and (iii) reaction of $SiCl_4$ and sodium vapor, and collection of silicon (in 0.5 g pellets) and NaCl (in pellet or small ingot form). A flow chart for the AeroChem process is shown in Fig. 15. No electrolysis of the salt to recover sodium is currently considered. The reasons for this are: (i) Na recovery would complicate the process dramatically, (ii) first-cut cost estimates show a cost disadvantage to recovery, (iii) talks with sodium manufacturers are discouraging as to the practicality of doing salt electrolysis on this small a scale at reasonable costs, and (iv) since sodium is made electrolytically it tends to be reasonably pure (calcium being the major impurity).

The raw materials required for the process are listed and described in Table VI. It is assumed that 90% of the silicon produced is collected. (In some runs as much as 82% of the silicon produced was collected, so this is not an unreasonable goal.) The rest is assumed mixed with the salt byproduct and thus lost. The reactor is to be run with slight (1-3%) excess $SiCl_4$ to avoid having to treat and dispose of unreacted sodium. The thermodynamic efficiency is greater than 99% at stoichiometry but some additional losses (1 to 3%) of $SiCl_4$ are assumed in the 5% loss figure (item 1.d. of Table VI). No $SiCl_4$ would be recycled and the salt byproduct carrying with it 10% of the silicon will be disposed of with no financial gain or loss. From our most recent results these estimates appear conservative; the amount of $SiCl_4$ needed may well be 5% less than that quoted (15.8 lb instead of 16.7 lb).

In Table VII the utilities requirements are described. The major power requirement (6.1 kWh/kg Si) is for the sodium vaporization process. The steam requirements (2.a.) are obtained from Yaw's Battelle process analysis by taking the Battelle number multiplied by 0.68, the ratio of $SiCl_4$ flow through the AeroChem and Battelle $SiCl_4$ purification trains. The major questions regarding Table VII are whether the large amount of heat released in the process can be

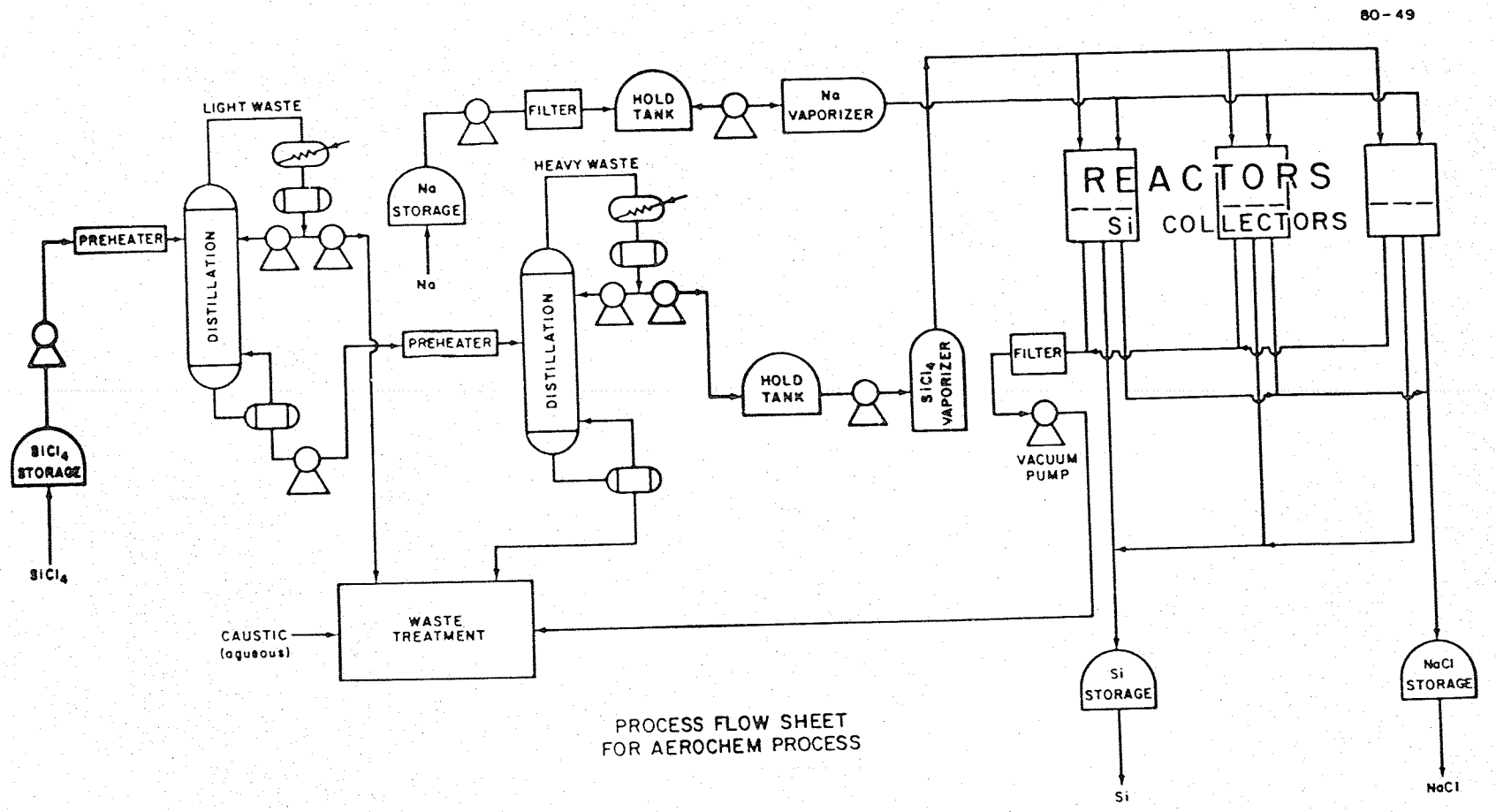


PROCESS FLOW SHEET
FOR AEROCHEM PROCESS

FIGURE 15 PROCESS FLOW SHEET FOR AEROCHEM PROCESS

TABLE VI

RAW MATERIAL REQUIREMENTS

| | Material | Cost/kg of Si |
|---|---|---|
| 1. | $SiCl_4$, 16.692 lb/kg at \$0.135/lb | \$2.252 |
| | a. $SiCl_4$ required at stoichiometry, 100% efficiency, 13.13 lb | |
| | b. 8% distillation loss, 1.335 lb | |
| | c. 10% loss due to Si collection inefficiency, 1.459 lb | |
| | d. 5% loss due to thermochemical inefficiencies and running slightly $SiCl_4$-rich, 0.768 lb | |
| 2. | Sodium metal, 8.033 lb/kg at \$0.1875/lb | 1.506 |
| | a. Na required at stoichiometry, 100% efficiency, 7.23 lb | |
| | b. 10% loss due to Si collection inefficiency, 0.803 lb | |
| 3. | Calcium hydroxide for waste disposal, 1.9 lb at \$0.015 lb | 0.029 |
| 4. | Argon, 4 SCF/kg at \$0.016/SCF | 0.064 |
| 5. | $N_2$, 7 SCF/kg at \$0.003/SCF | 0.021 |
| | Raw materials cost, 1975 dollars | \$3.873 |
| | Raw materials cost, 1980 dollars | \$5.422 |

TABLE VII

UTILITIES REQUIREMENTS

| | Cost/kg of Si |
|---|---|
| 1. Electricity, 9.06 kWh/kg at $0.0342/kWh | $0.310 |
| a. Sodium (8.03 lb) vaporization at 90% efficiency, 6.15 kWh | |
| b. $SiCl_4$ (15.36 lb) vaporization at 80% efficiency, 0.36 kWh | |
| c. Miscellaneous pumps, blowers, 2.0 kWh | |
| d. Sodium vapor delivery heaters, 0.05 kWh | |
| e. Reactor heaters (assumes using 2.8 kWh of heat generated by chemical reaction), 0.5 kWh | |
| 2. Steam, 7.8 lb at $0.00135/lb | 0.0105 |
| a. $SiCl_4$ purification, 6.5 lb | |
| b. Caustic storage heater, 0.3 lb | |
| c. Na storage tanks, 1.0 lb | |
| 3. Cooling water, 88 gal/kg at $0.09/Mgal | 0.0079 |
| a. $SiCl_4$ purification, 23 gal | |
| b. Reactor cooling, primarily NaCl condensation, 65 gal | |
| 4. Process water, 16 gal/kg at $0.405/Mgal | 0.0065 |
| a. Diluent for waste treatment, 16 gal | |
| 5. Credit for 12 kWh of heat generated by condensing and cooling salt byproduct from 900°C to room temperature | --- |
| Utilities cost, 1975 dollars | $0.335 |
| Utilities cost, 1980 dollars | $0.469 |

put to use in the plant and what trade-offs are involved in the purchase of equipment which would allow this to be done. The process requires an electrical energy input of about 9 kWh/kg Si with another 2.3 kWh/kg Si needed in the form of steam. The total heat release from reacting and cooling the products to near room temperature is about 16.5 kWh/kg Si. Of this, in this analysis we plan on using only the 2.8 kWh/kg Si liberated chemically in the reactor to provide the major source of heat needed to maintain a reactor temperature of 1500°C. The major heat release (8 kWh) occurs when the NaCl vapor made in the reactor is condensed, a process which will occur at 800°C to 900°C. The extent to which this high quality heat source can be used is uncertain. It needs a more detailed engineering study than we have been able to do to date. Therefore, this regenerative heat source will not be used here.

Labor costs are estimated assuming a total of six workers is needed; two workers are required to operate the $SiCl_4$ purification process, two to operate the reactors, one for product handling, and one for waste treatment. Since no workers are needed for electrolysis, our overall manpower requirement will be less than Battelle's.

For a first cut at getting major equipment costs we rely heavily on Table VIIA-1-5 of Yaws' 13th PIM presentation on the Battelle process. To get our costs we have modified this table as follows:

a. The $SiCl_4$ purification train required (with associated scrubbers) is similar to Battelle's, but smaller. We have to purify 32% less $SiCl_4$ per kg of Si produced.* The costs of our equipment are thus scaled down using a factor $(1.00 - 0.32)^{0.6} = 0.79$.

b. No $SiCl_4$ recovery from the reactor effluent is needed so no such equipment is included.

c. No electrolysis-related equipment is required.

d. No high-temperature heat exchangers to extract useful heat from molten NaCl are included in this analysis. Thus equipment corresponding to the Therminol system in the Battelle process is not included.

---

* This is in many respects a worst case assumption. The $SiCl_4$ purification train may be more extensive than needed if, for example, the heavy or light (or both) impurities tend to be separated out by the reaction and end up in the salt byproduct rather than in the silicon.

e. We envision having 15 small 10 kg $h^{-1}$ reactors* which produce Si, separate it from the NaCl at 90% efficiency, and produce $\approx 0.5$ g pellets of Si. The cost of each reactor is estimated to be about $25,000 for a total reactor cost of $375,000.

f. The sodium metal vaporizer requires 0.84 MW. Battelle's zinc vaporizer requires 0.61 MW. A factor of $(0.84/0.61)^{0.6} = 1.21$ has been used to scale our costs to $174,000 (from Battelle's $144,000) for this item.

g. Sodium storage facilities (50,000 gal at 100°C) are included at a cost of $50,000 to hold a two-week supply of Na.

h. Two 1000 cfm vacuum pumps are required at an estimated cost of $50,000. (The second pump serves as a backup.) These pumps assume that the argon requirements are as large as shown in Table VI. We believe this to be very conservative.

With these changes we obtain a cost for major process equipment of $1,001,000 (1975 dollars) or $1,414,000 (1980 dollars). The fixed capital investment is taken (from Yaws) to be 5.72 × (major process equipment cost) or $5,726,000 (1975 dollars) or $7,953,000 (1980 dollars).

From the costs thus developed for raw materials, utilities, labor, and major process equipment, Table VIII is obtained. A cost of silicon of \$7.27 $kg^{-1}$ (1975 dollars) or \$10.18 $kg^{-1}$ (1980 dollars) is projected for a 1000 MT $yr^{-1}$ AeroChem process.

## VII. CONCLUSIONS

During this contract the major tasks proposed in this program were completed. The main conclusions of this program are:

1) The jet impaction technique separates liquid silicon from NaCl vapor with efficiencies as high as 80%. This efficiency appears to be a function of temperature; however, the optimum conditions were not determined.

2) The production of 1/4 kg silicon ingots was demonstrated on a repeated basis.

---

* These small reactors would be slightly larger than one demonstrated in a 50 MT $yr^{-1}$ unit. The conservative assumption has thus been made that no savings are realized by scale-up of the reactors in going from a 50 MT $yr^{-1}$ unit to the 1000 MT $yr^{-1}$ plant.

TABLE VIII

TOTAL PRODUCT COST ESTIMATION

| | Cost/kg of Si |
|---|---|
| 1. Direct Manufacturing Cost (Direct Charges) | |
| a. Raw materials | $3.873 |
| b. Direct operating labor | 0.290 |
| c. Utilities | 0.335 |
| d. Supervision and clerical | 0.043 |
| e. Maintenance and repairs | 0.573 |
| f. Operating supplies | 0.114 |
| g. Laboratory charge | 0.043 |
| 2. Indirect Manufacturing Cost | |
| a. Depreciation | 0.573 |
| b. Local taxes | 0.114 |
| c. Insurance | 0.057 |
| 3. Plant Overhead | 0.309 |
| 4. Byproduct Credit | --- |
| 4a. Total Manufacturing Cost (1 + 2 + 3 + 4) | $6.305 |
| 5. General Expenses | |
| a. Administration | $0.378 |
| b. Distribution and sales | 0.378 |
| c. Research and development | 0.189 |
| 6. Total Product Cost (1975 dollars) | $ 7.27 |
| Total Product Cost (1980 dollars) | $10.18 |

3) The resulting silicon product is free ( < 10 ppma) from the sodium reactant. Other impurities are minimal ( < 1-10 ppma), but more work is needed to improve these levels.

4) The jet impaction technique has been demonstrated to purify the silicon product by more than a factor of $10^3$ in some cases.

5) All major design flaws or equipment problems were overcome. No insurmountable or recurring difficulties were encountered. The silicon test apparatus ran dependably for periods as long as 1 1/2 hours as limited by reactant supply reservoirs.

6) Materials of construction for the reactor/collector can be made from graphite. Impregnated graphite, graphite coated with silicon, SiC, and alumina were found to be satisfactory collection vessel materials. Untreated graphite can be used as a collection vessel by carefully maintaining the temperature below the m.p. of Si.

7) The projected cost of the silicon from the AeroChem process is $10.18/kg Si (1980$).

In summary, we have demonstrated that the AeroChem process is feasible for the production of silicon. It appears capable of producing silicon at a cost well below the Task I goals. No sodium is present in the product so the potential for producing very pure silicon is high. More work is, however, needed to reduce impurity levels in the silicon product.

## VIII. NEW TECHNOLOGY

The basic process described in this report has been identified as New Technology. AeroChem filed for U.S. patent on 20 October 1980 and disclosed to JPL on 25 November 1980 with a petition for waiver of domestic rights.

# IX. REFERENCES


1. Miller, W.J., "Silicon Halide-Alkali Metal Flames as a Source of Solar Grade Silicon," First Quarterly Report, AeroChem TN-178, September 1977.

2. Miller, W.J., "Silicon Halide-Alkali Metal Flames as a Source of Solar Grade Silicon," Second Quarterly Report, AeroChem TN-182, December 1977.

3. Olson, D.B. and Miller, W.J., "Silicon Halide-Alkali Metal Flames as a Source of Solar Grade Silicon," Third Quarterly Report, AeroChem TN-187, ERDA/JPL 954777-78/3, March 1978.

4. Olson, D.B. and Miller, W.J., "Silicon Halide-Alkali Metal Flames as a Source of Solar Grade Silicon," Fourth Quarterly Report, AeroChem TN-192, DOE/JPL 954777-78/4, June 1978.

5. Olson, D.B. and Miller, W.J., "Silicon Halide-Alkali Metal Flames as a Source of Solar Grade Silicon," Fifth Quarterly Report, AeroChem TN-199, DOE/JPL 954777-78/5, October 1978.

6. Olson, D.B. and Gould, R.K., "Silicon Halide-Alkali Metal Flames as a Source of Solar Grade Silicon," Seventh Quarterly Report, AeroChem TN-205, DOE/JPL 954777-79/7, April 1979.

7. Olson, D.B., Miller, W.J., and Gould, R.K., "Silicon Halide-Alkali Metal Flames as a Source of Solar Grade Silicon," Final Report, AeroChem TP-395, DOE/JPL 954777-80/8, January 1980.

8. Blocher, J.M., Jr. and Browning, M.F., "Evaluation of Selected Chemical Processes for Production of Low-Cost Silicon. Phase I," Sixteenth/ Seventeenth Quarterly Progress Report, Battelle Columbus Laboratories, DOE/JPL 954339-80/16, 17, 7 March 1980.

9. See, for example, Streetman, B.G., Solid State Electronic Devices (Prentice Hall, Englewood Cliffs, NJ, 1980).

10. Yaws, C.L. and Li, K-Y., "Process Feasibility Study in Support of Silicon Material Task I," Seventeenth Quarterly Report, DOE/JPL 954343-80/17, December 1979.

PHASE II

# PHASE II

## I. INTRODUCTION

The thermal decomposition of silane is one of the processes currently being considered by JPL as a source of cheap solar grade silicon. The objective of the work in Phase II of this contract was to provide data to support production process development by characterizing the kinetics and mechanism of the formation and growth of silicon particles from the decomposition of silane at process temperatures. The experiments were aimed at determining the rates at which gas-phase species form silicon particle precursors, the time required for silane decomposition to produce silicon particles, and the competing rate of growth of silicon seed particles injected into a decomposing silane environment.

The kinetics of monosilane pyrolysis were first studied by Hogness et al[1] and later by Stokland,[2] using static methods and manometric rate measurements. Hogness et al report that the only products of the reaction were silicon and hydrogen, and that no disilane was formed. Consequently, they interpreted their kinetic measurements on the assumption of a constant stoichiometry of

$$SiH_4 \rightarrow Si + 2H_2 \qquad (1)$$

Stokland, on the other hand, detected disilane as a reaction product. He suggested the occurrence of

$$2SiH_4 \rightarrow Si_2H_6 + H_2 \qquad (2)$$

A thorough investigation of monosilane decomposition was made by Purnell and Walsh.[3] They were able to monitor the reaction products using gas chromatography. They suggest two possible mechanisms

$$\left.\begin{aligned} SiH_4 &\rightarrow SiH_2 + H_2 \\ SiH_2 + SiH_4 &\rightleftarrows Si_2H_6 \\ SiH_2 + Si_2H_6 &\rightleftarrows Si_3H_8^{\bullet} \end{aligned}\right\} \qquad (3)$$

or

$$\left.\begin{aligned} SiH_4 &\rightarrow SiH_3^{\bullet} + H \\ H + SiH_4 &\rightleftarrows H_2 + SiH_3 \\ SiH_3^{\bullet} + SiH_4 &\rightleftarrows Si_2H_6 + H \\ 2SiH_3^{\bullet} &\rightarrow Si_2H_6 \end{aligned}\right\} \qquad (4)$$

More recent studies by several workers support the mechanism described by Eq. (3).[4,5] Unambiguous experimental evidence confirmed this mechanism in the study by Neudorfl et al.[6]

The early workers found[1-3] a powdered deposit on the walls of the reaction vessel used for the experiments. This powdered deposit turned to a metallic-like mirror upon heating for several minutes. Purnell and Walsh found that the ratio of H/Si changed from 2 to less than 0.5 if the powdered product was heated for several minutes. They speculated that the origin of this powdered product having the empirical formula $(SiH_2)_n$ is

$$SiH_2 + Si_{n-1}H_{2n} \rightarrow Si_nH_{2n+2}$$
$$Si_nH_{2n+2}\ (gas) \rightarrow \text{wall product} \qquad (5)$$

Such steps imply that the higher silanes are formed in the pyrolysis of monosilane by successive insertion of $SiH_2$ or $SiH_3$ into lower silanes until eventually a sufficiently long one is formed. It diffuses to the wall and condenses.

A possible alternative is that the silene species continuously condense together in a reaction such as

$$SiH_2 + (SiH_2)_{n-1} \rightarrow (SiH_2)_n$$
$$(SiH_2)_n \rightarrow \text{wall product} \qquad (6)$$

The presence of $(SiH_2)_n$ as an intermediate shows that in the pyrolysis of monosilanes there is a greater tendency for Si-Si bonds to be formed than to be broken. Finally, the decomposition of the solid silicon hydride is described by

$$(SiH_2)_n \rightarrow (SiH_x)_n + (1 - \tfrac{1}{2}x)\ H_2 \qquad (7)$$

The similarities of the final product to amorphous silicon produced from the low pressure gas discharge decomposition of silane is striking. The mechanism of formation of amorphous silicon produced by gas discharge may be similar to the mechanism of formation of the solid powdered product produced by the thermal decomposition of silane.

Little work has been done on the growth of silicon particles produced from the thermal decomposition of silane. Tabayashi and Bauer[7] studied the formation and growth of liquid silicon droplets formed by the decomposition of

silane in a shock tube and the time resolved detection of small (0.1 μm diam) droplets. Levin[8] proposed a mechanism of silicon particle growth produced in a free space reactor. The need for real-time particle growth studies is apparent. Thus, the ability to monitor the growth of silicon particles formed either by homogeneous or heterogeneous nucleation and to observe the reaction products in situ could prove useful in understanding the growth mechanism of silicon particulates formed from silane decomposition.

The objective of the work in Phase II of this contract was to characterize the kinetics and mechanism of the formation and growth of silicon particles produced from the thermal decomposition of silane. The experiments were aimed at determining the rates at which gas-phase species form silicon particle precursors, the time required for silane decomposition to produce silicon particles, and the competing rate of growth of silicon seed particles injected into a decomposing silane environment.

The effort on this contract comprised:

1. Construction of a high-temperature fast-flow reactor (HTFFR) and assembly of diagnostic equipment appropriate for studying the rate of decomposition of $SiH_4$ and the rate of formation and growth of Si particles.
2. Particle formation studies to determine the time required for $SiH_4$ decomposition to proceed to the stage where Si particle formation occurs.
3. Particle growth studies to determine the rate of growth of silicon seed particles injected into a decomposing $SiH_4$ environment.
4. Decomposition studies to determine the rate at which gas-phase species react to form Si particle precursors.
5. Data interpretation to apply to the performance of processes for producing Si from $SiH_4$.

# II. TECHNICAL DISCUSSION

## A. HTFFR APPARATUS FOR MONITORING PARTICLE GROWTH

For this contract, the AeroChem high-temperature fast-flow reactor (HTFFR), Fig. 1, was adapted so that heterogeneous chemical reactions, such as the thermal decomposition of silane to form particulates could be studied. With this apparatus, the rates at which gas-phase species form silicon particle precursors, the time required for silane decomposition to produce silicon particles, and the competing rate of growth of silicon seed particles injected into a decomposing silane environment were studied. The modified apparatus allows several light scattering techniques to be used for determining the average size or the size distribution of particles formed during the course of silane decomposition.

Particle growth was monitored at the HTFFR observation plane as a function of the time the silane gas resided in the uniformly heated reaction zone. This time was varied by positioning a cooled inlet at differing distances upstream of the observation window. For example, at a gas velocity of $10^3$ cm $s^{-1}$ and at various positions ranging from 0 to 30 cm upstream of the observation plane, the silane resided in the reaction zone for between 0 and 30 ms. A wide range of contact times was accessible by changing the gas velocity as well as the inlet position.

The flow reactor portion of the HTFFR has been described previously.[9] It consists of a 2.5 cm i.d. alumina reactor wound with 0.040 in. molybdenum resistance wire in three contiguous, independently-powered zones. Because the experiments involved a reducing atmosphere, and because rigorous leak prevention steps were taken, it was possible to use molybdenum resistance heaters instead of the Pt/Rh normally used. The reactor tube was insulated with zirconia insulation and about 1 kW of power applied to each heater section enabled the temperature inside the HTFFR to easily reach 1800 K. A movable Pt/10% Rh thermocouple allowed the temperature throughout the reactor tube to be monitored.

Silane gas entered the reactor tube through a movable water-cooled inlet shown in Fig. 2. The cooled inlet entered from the bottom and could be positioned at varying distances from the observation plane. The useful length of the reactor (for kinetic measurements) was the uniform temperature zone (controlled by adjusting the current flow to the resistance heaters) extending

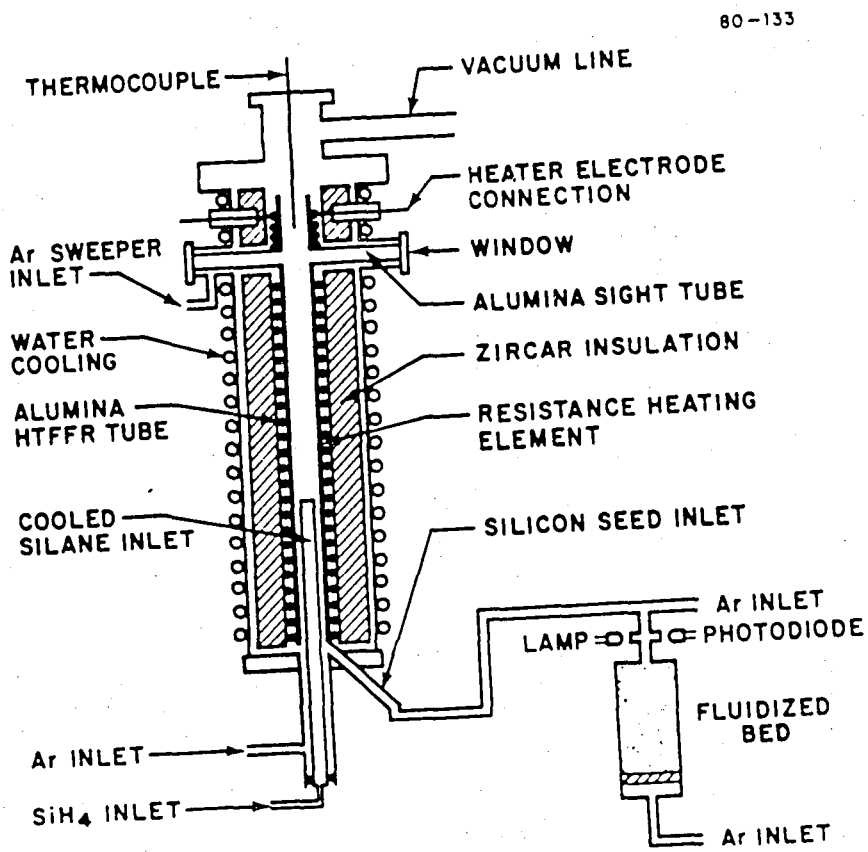


FIGURE 1 HIGH TEMPERATURE FAST FLOW REACTOR FOR MEASUREMENTS OF Si PARTICLE FORMATION AND GROWTH KINETICS

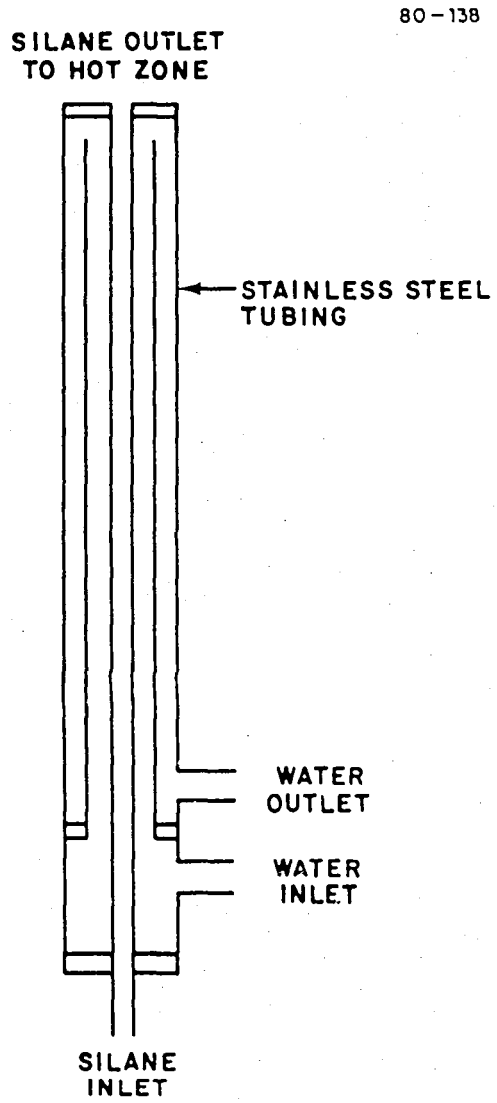


FIGURE 2 SCHEMATIC DIAGRAM OF WATER-COOLED INLET FOR INTRODUCING SILANE TO HTFFR

about 30 cm upstream of the observation ports. The cooled inlet was tested and shown to deliver room-temperature silane gas to any point in the reaction zone when that zone was at > 1500 K. Silane and argon buffer gas were metered into the reactor through calibrated orifices.

Four 1 cm diam holes at 90° to one another were located at the HTFFR observation plane. Through these ports various optical diagnostics were applied as silane was decomposed in a controlled fashion. Figure 3 shows the details of the observation plane as set up for the turbidity/90° scattering measurements used for initial tests. A 1 mW Spectra Physics model 113 He-Ne laser beam or a 0.1 W Spectra Physics model 162A-07 argon ion laser beam, chopped at 1000 Hz passed through a beam splitter to provide a measurement of $I_o$. The laser beam entered the HTFFR through a flat window (or a lens which focused the beam to the center of the reactor tube). Light baffles, constructed from graphite discs with 0.6 cm diam holes and spaced 1 cm apart, defined the optical paths and eliminated unwanted light scattering. The laser beam exited the HTFFR through a Brewster angle window mounted on a Wood's horn to prevent back reflections of the laser beam. Detector A (Fig. 3) was a trialkali phototube (RCA 5845) which measured the scattered He-Ne or $Ar^+$ laser light at 90° to the direction of the laser beam. Detector B (for turbidity) and the detector for $I_o$ were both silicon photodiodes (Molectron power meter T3-02-DW).

A fluidized bed feed system (Fig. 4) was built to inject Si seed particles into the reactor. Before entering the HTFFR, a portion of the diluent gas flow (Ar or $N_2$) was diverted through the bed to fluidize it; some Si particles were suspended above the bed and entrained in this gas flow for transport to the HTFFR. The fraction of the total gas flow that passed through the bed determined the particle concentration entering the HTFFR. A calibrated optical extinction monitor at the output of the bed was used to measure the particle concentration in the flow stream. The fluidized bed was tested successfully with 150 μm diam Si particles and was used with 5 μm diam Si particles during the seeding experiments.

To measure the amount of undecomposed silane gas, a long path (97 cm) absorption cell was connected near the exhaust of the HTFFR. The IR absorption optical system (see Fig. 5) consisted of a Globar light source (a resistively heated SiC rod) using a pinhole collimator combined with two planoconvex $CaF_2$ lenses, a 1 m absorption cell with $CaF_2$ windows, and a PbSe detector with

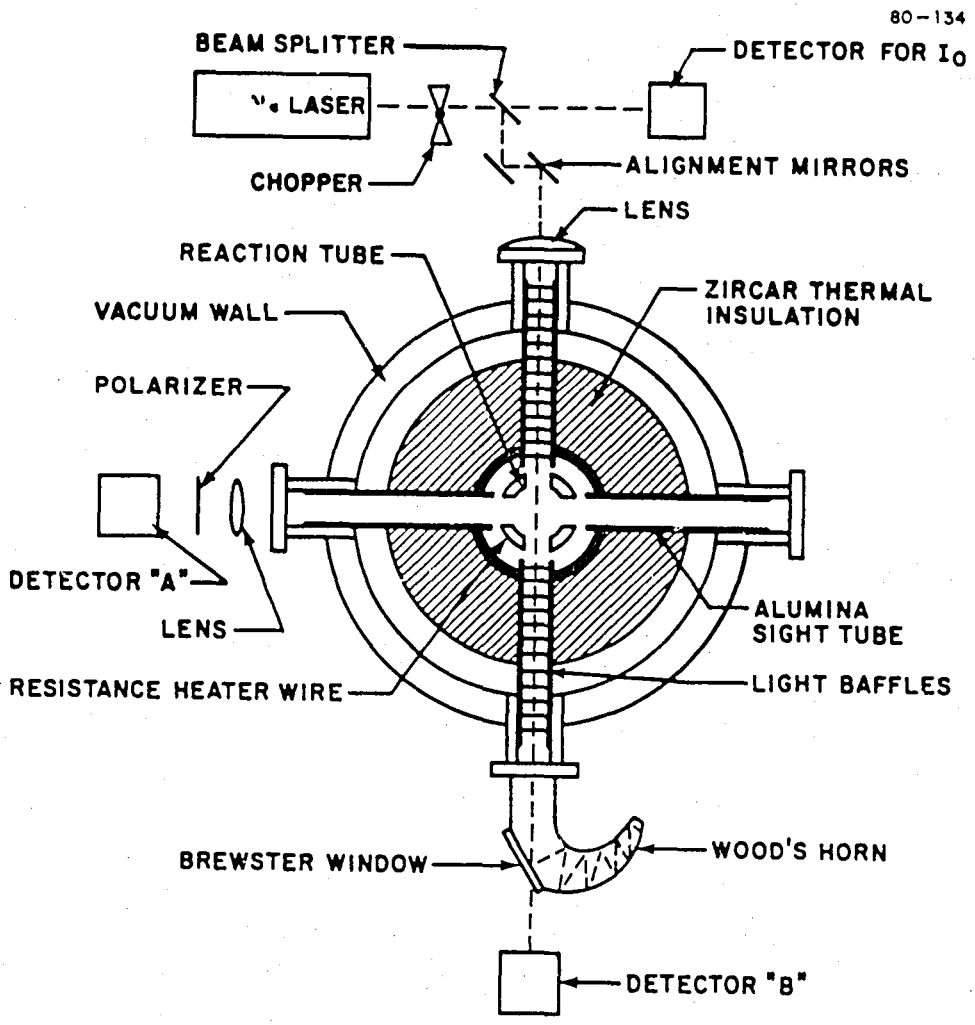


FIGURE 3 OBSERVATION PLANE OF HTFFR FOR MEASUREMENTS OF PARTICLE FORMATION AND GROWTH KINETICS

Detector A for 90° scattering; Detector B for turbidity/forward scattering.

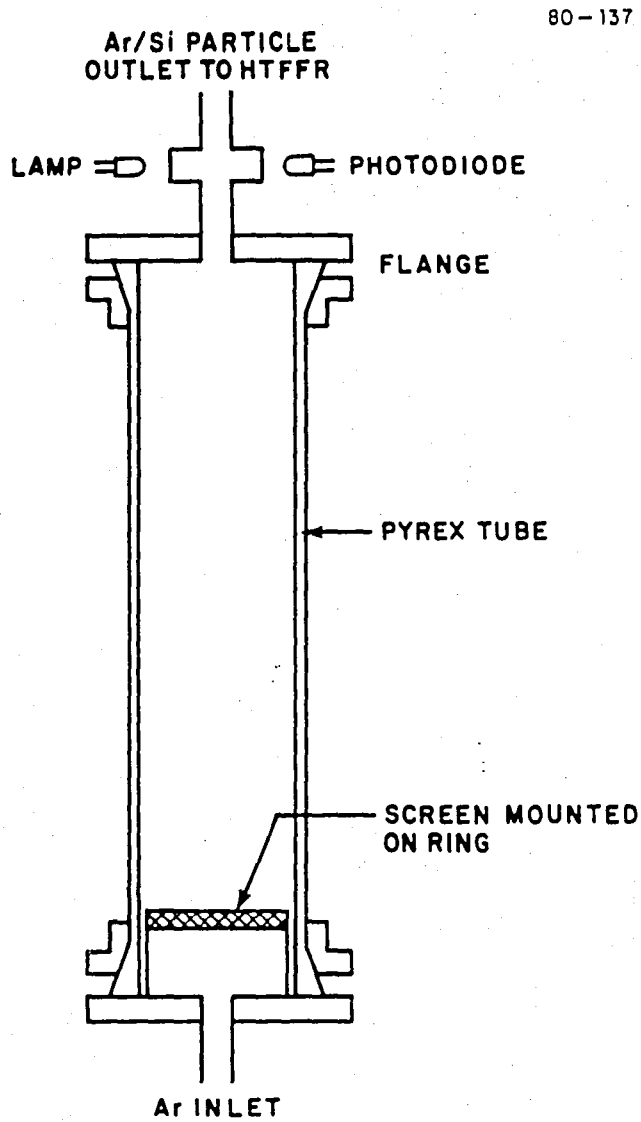


FIGURE 4 FLUIDIZED BED FEED SYSTEM FOR ADDING PARTICULATES TO GAS FLOW

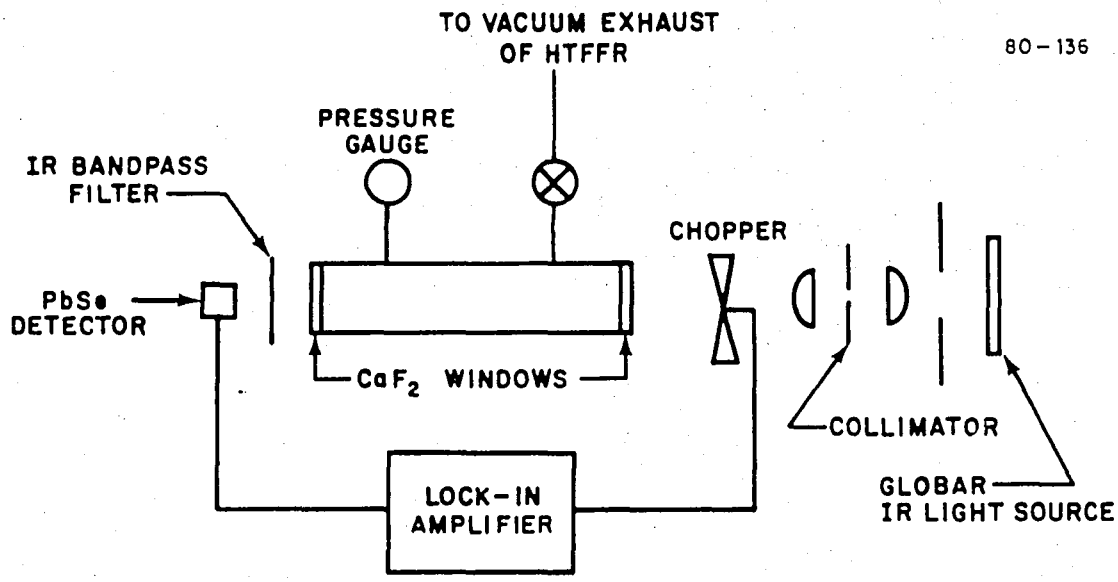


FIGURE 5 IR ABSORPTION SYSTEM FOR MEASUREMENTS OF RESIDUAL SILANE EXITING THE HTFFR

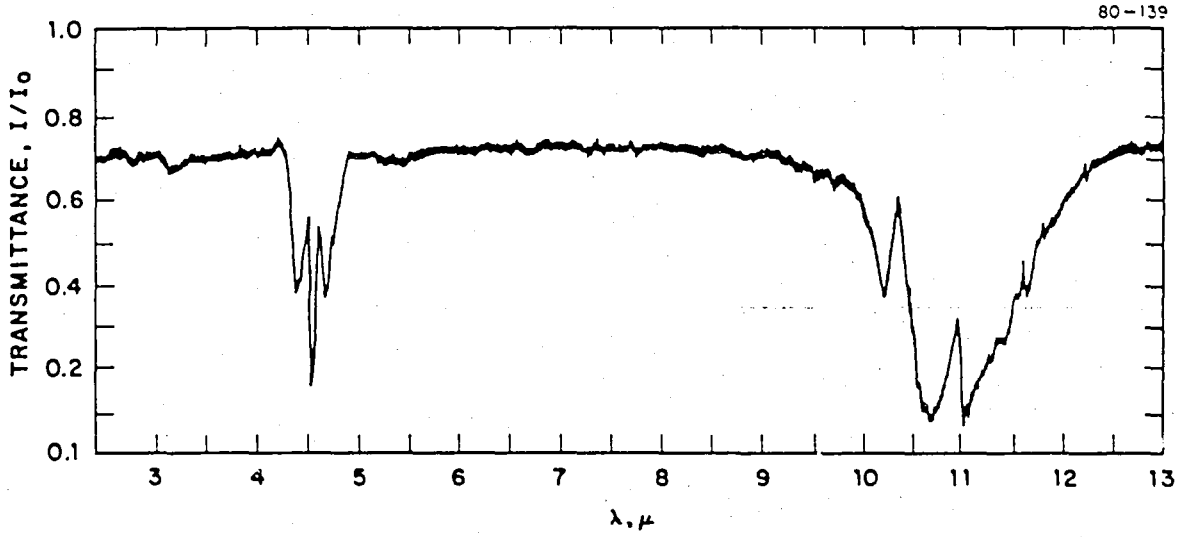


FIGURE 6 INFRARED ABSORPTION SPECTRUM OF SILANE

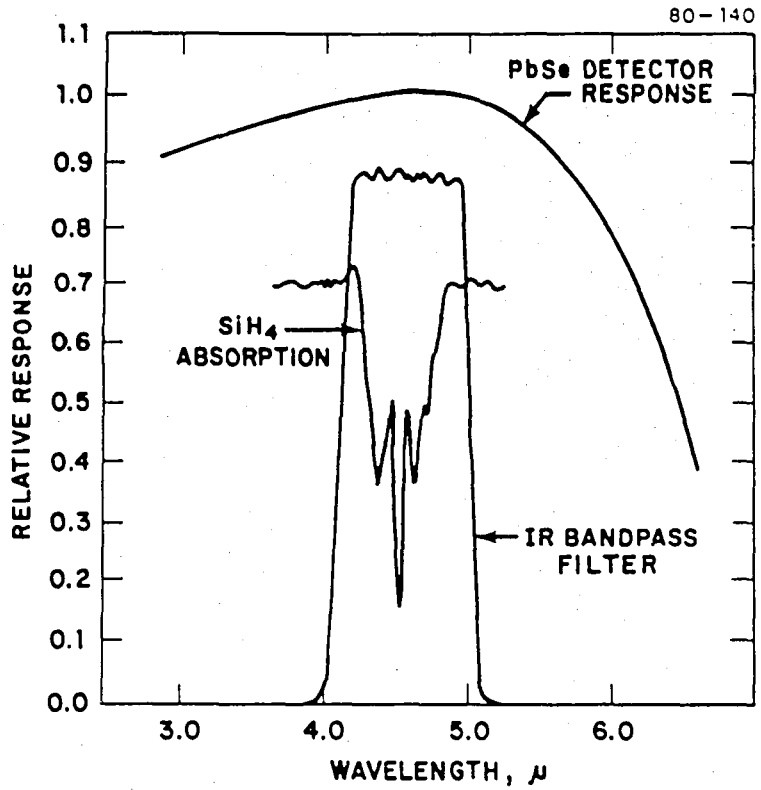


FIGURE 7 PbSe DETECTOR AND IR BANDPASS FILTER CHARACTERISTICS COMPARED TO SILANE ABSORPTION SPECTRUM IN THE 3.0-6.0 μm REGION

a 4.2 to 4.8 μm bandpass filter. The light source was chopped and the signal was detected with a lock-in amplifier.

The infrared absorption of silane is shown in Fig. 6. The 4-5 μ absorption band was chosen for the absorption measurements primarily because this region is easily accessible by common IR detectors and the optics could be made from $BaF_2$ or $CaF_2$, relatively inexpensive and durable materials. The PbSe detector (No. 5055 IR Industries) has its peak sensitivity in the 4-5 μ region and the response is nearly flat as shown in Fig. 7. The optical bandpass filter spans several features of the absorption spectrum. It was anticipated that the effect of this structure would be somewhat averaged and the absorption would not deviate too severely from Beer's law. Three calibration runs were made by filling the IR absorption cell with silane gas at various pressures from 0.1 to 20 Torr (at 293 K) and measuring the corresponding signal outputs from the PbSe detector. All pressures were measured with a Wallace

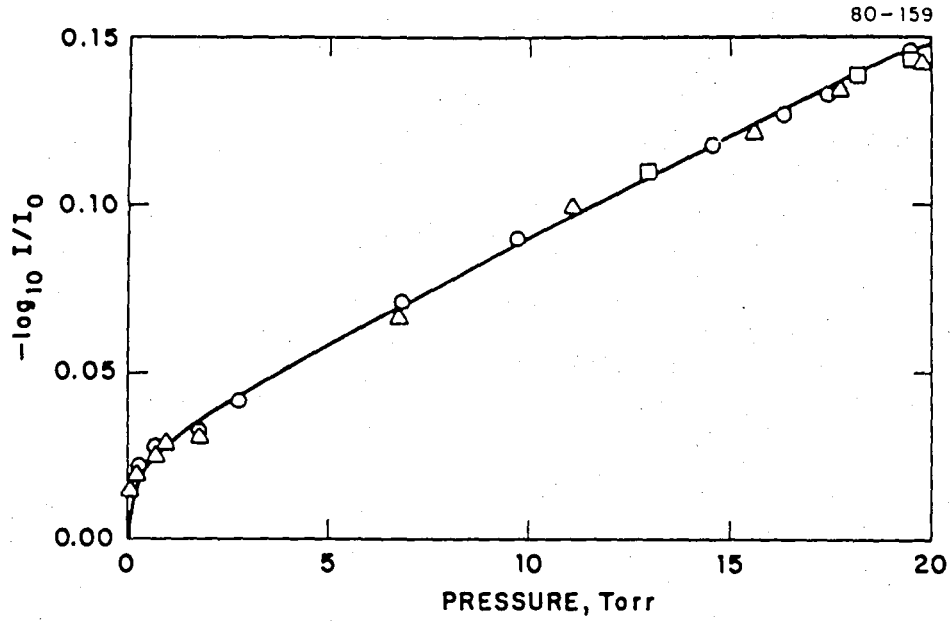


FIGURE 8 CALIBRATION CURVE FOR SILANE INFRARED ABSORPTION SYSTEM

Path length = 97 cm, 4.2-4.8 μm bandpass, PbSe detector. Silane pressure measured at 293 K.

and Tiernan pressure gauge. The data shown in Fig. 8 were taken at a Globar source temperature of ≈ 1500 K. To reduce the data in Section II.D, the pressure of silane was converted to silane concentration. In addition, these data were obtained in the presence and absence of several hundred Torr of argon. Thus, the argon pressure did not noticeably affect the absorption bands of $SiH_4$ at the 4-5 μ wavelength region.

## B. LIGHT SCATTERING RESULTS

The Mie theory is a formal solution of Maxwell's equations for the scattering of electromagnetic radiation by spherical homogeneous particles of arbitrary size. The theory is fully explained in several references;[10,11] hence, only the relevant expressions will be presented here. The results for the scattering and extinction cross sections are

$$C_{scatt} = \frac{\lambda^2}{2\pi} \sum_{n=1}^{\infty} (2n+1) \left( |a_n|^2 + |b_n|^2 \right) \qquad (8)$$

$$C_{ext} = \frac{\lambda^2}{2\pi} \sum_{n=1}^{\infty} (2n+1)\ \mathrm{Re}(a_n + b_n) \tag{9}$$

for the light of wavelength $\lambda$ incident on a sphere of radius r. The Mie coefficients $a_n$ and $b_n$ are complicated expressions involving spherical Bessel functions and their derivatives and are functions of the complex index of refraction m and the size parameter $x = 2\pi r/\lambda$.

For convenience, the cross sections $C_{ext}$ and $C_{scatt}$ are often expressed as the efficiencies $Q_{ext}$ and $Q_{scatt}$ defined as the ratio of the Mie cross section to the geometrical cross section ($\pi r^2$), i.e.,

$$Q_{ext} = \frac{C_{ext}}{\pi r^2} \tag{10}$$

and

$$Q_{scatt} = \frac{C_{scatt}}{\pi r^2} \tag{11}$$

When these efficiencies are plotted as a function of the particle size parameter they often exhibit an oscillatory behavior which converges to a value of 2. The oscillatory behavior is attributed to light interference or diffraction effects which are observed in the far field. The convergence to a value of 2 is due both to light being removed geometrically (the particle shadow) and to light being removed by interference or diffraction effects.

The Mie oscillations are distinct functions of the particle size and they thus form the basis for determining particle size. They were used by Vietti and Schuster[12] to determine the sizes of water droplets formed in cloud chamber experiments. Experimentally, they obtained Mie oscillations in the scattered light intensity as a function of time as the water droplets increased in size. Since each peak or valley in the scattered light intensity was characteristic of a particle size, the particle size as a function of time was determined.

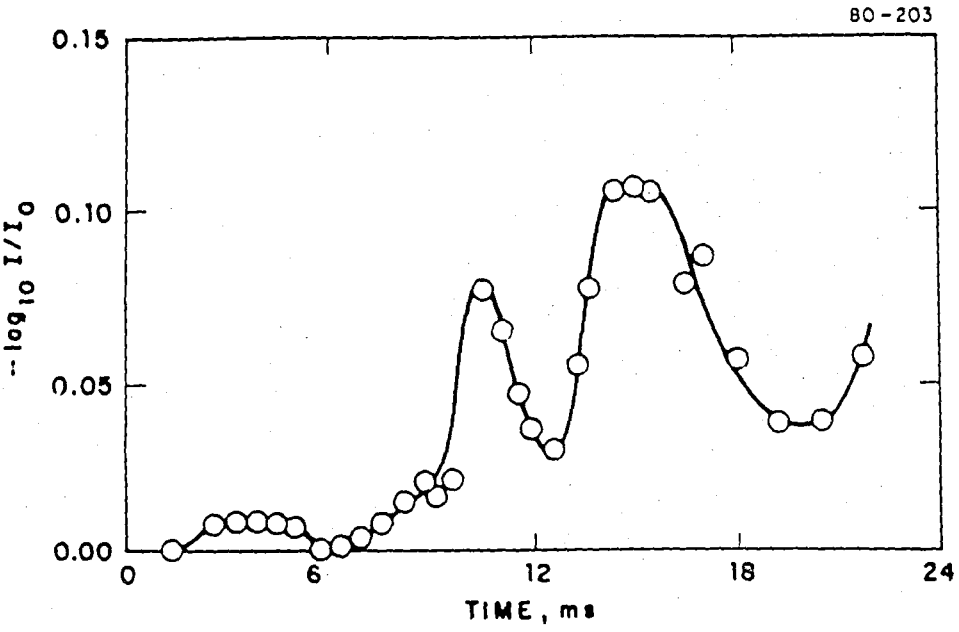


FIGURE 9 MIE RESONANCE PEAKS IN RAW EXTINCTION DATA

We anticipated the observation of Mie oscillations in both the light extinction and light scattering data obtained with our HTFFR apparatus. Increasing the residence time of the silane gas in contact with the hot zone of the HTFFR (by varying the position of the cooled silane inlet) was expected to increase the size of the silicon particles produced from the thermal decomposition of silane. Unlike the cloud chamber experiments the flow tube method used here establishes an independent time base due to the flow itself. Thus we could hold the particles in the observation zone in a steady-state fashion to perform experimental diagnostics on a preselected particle size.

During the initial experiments several important results were obtained. The observation of distinct Mie oscillations in both the extinction and scattering data indicated that particles formed from the gas phase had grown to radii greater than $\approx 0.05$ μm. This conclusion was also supported by the simultaneous observation that the scattered laser light at 90° was depolarized.

Representative extinction data are plotted in Fig. 9 as a function of residence time, showing the distinctive Mie oscillations. These results were obtained at 1173 K, an argon bath pressure of 200 Torr, a $SiH_4$ flow rate of $2.5 \times 10^{-5}$ mol $s^{-1}$ and a flow velocity of 500 cm $s^{-1}$. The y-axis of this plot is proportional to the efficiency $Q_{ext}$ as defined by Eq. (10). The x-axis of the plot is the residence time in the HTFFR (distance/velocity). The

positional dependence of the oscillations shows directly the steady-state nature of the experiments and demonstrates that the x-axis is also proportional to the particle size. For the conditions of Fig. 9, the time required to observe the first peak of the Mie oscillations was $\approx 2.5$ ms. The appearance of additional peaks indicates that the particles continued to grow for $\approx 20$ ms.

Another observation of great importance is that results like those shown in Fig. 9 demonstrate that the particles formed have a monodisperse size distribution. This is generally assumed to be the case when Mie oscillations are observed in light extinction and scattering data. Vietti and Schuster[12] showed that the sharpness of the peaks is directly related to the standard deviation of the normal distribution of sizes which was assumed in their work. When the standard deviation had a value of 2, the Mie oscillations disappeared. Thus, the Mie oscillations shown in our work could be compared with computer calculations to determine the exact size distribution of the particles produced.

Other preliminary conclusions and speculations can be drawn from the initial data. It seems likely that the observed particle growth (from $r \approx 0.05$ μm upward) results from gas-particle interactions rather than agglomeration of small particles because silicon is solid at 1173 K and because agglomeration would be expected to be "slow" under the present conditions. Growth of particles prior to the appearance of the Mie oscillations (in the case of Fig. 9, before 2.5 ms) could probably also be observed using Rayleigh scattering methods (which were beyond the scope of the present work). It is likely that much of the particle growth in these early stages is the result of homogeneous processes and agglomeration of small particles and we therefore preliminarily concluded that the time domain for the observation of two different particle growth regimes could be defined.

Because the Mie oscillations observed in the scattering and extinction data were used to determine the size of the particles, their nature was examined in detail. Several peaks were not observed (missed) when the cooled inlet was moved in 1.0 cm increments. Detailed ripple structure was found when the cooled inlet was moved in 0.1 cm increments. All of the Mie oscillations, but not the ripple structure, were observed when the cooled inlet was moved in 0.5 cm increments. Thus, the degree of structural detail measured in the oscillations could be regulated by controlling the increments

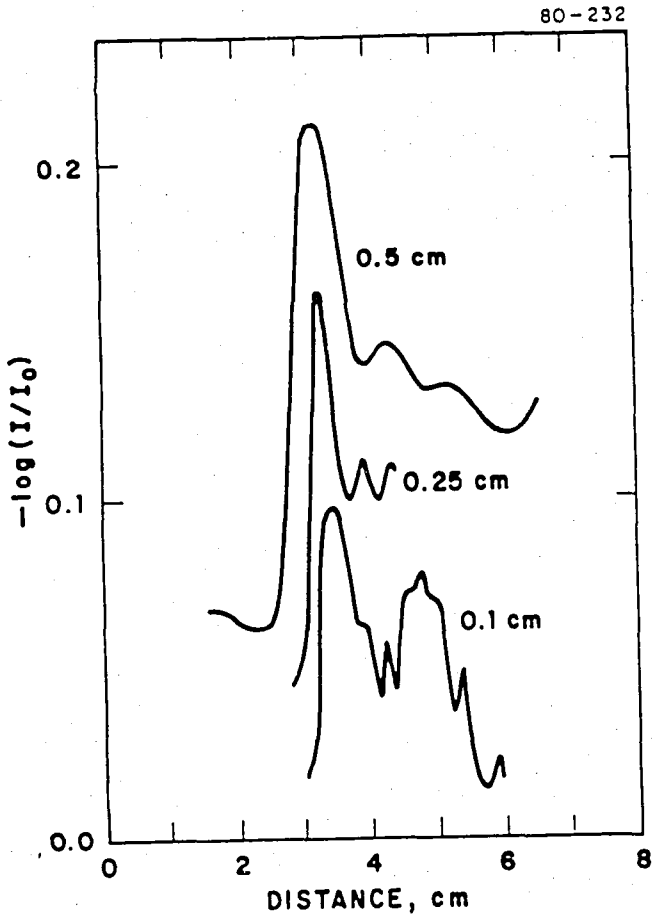


FIGURE 10 INCREASE IN THE STRUCTURE OF THE MIE OSCILLATIONS IN EXTINCTION DATA AS THE POSITION INCREMENTS OF THE COOLED INLET ARE DECREASED

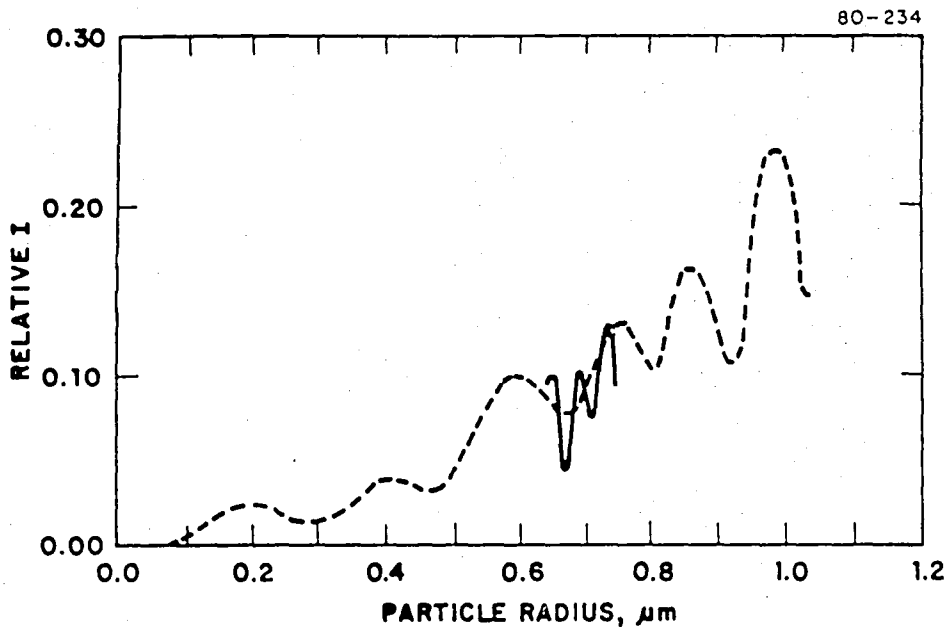


FIGURE 11 RESULTS OF MIE THEORY CALCULATIONS WHICH SHOW THE RIPPLE STRUCTURE (SOLID LINE) IN THE MIE OSCILLATIONS (DOTTED LINE)

in which the position of the cooled inlet was changed. Figure 10 illustrates this for extinction data. To confirm that the detailed structure was not an artifact, computer calculations using the Mie code were made. The dotted line shown in Fig. 11 is the predicted Mie oscillation while the solid line is the detailed ripple structure also predicted by using a finer calculational grid. Thus, the observed ripple structure is predicted by theory and the experimental observation was assumed to be real. Fortunately, this complex structural detail was not needed for determining particle size.

The detailed considerations of the Mie oscillations thus established that the positions of the gross features were directly related to particle radii. Computer calculations using Mie scattering theory were then made for the He-Ne laser wavelength of 632.8 nm, a refractive index of m = 3.44-0.02i, and a particle number density of $10^8$ particles $cm^{-3}$. A delta function was used to simulate a monodisperse particle size distribution. To obtain the complex index of refraction for silicon, we used the absorption spectrum for Si obtained by Dash and Newman[13] to calculate the extinction index, k, from

$$k = \frac{\lambda\alpha}{4\pi} \tag{12}$$

where $\alpha$ is the absorption coefficient and $\lambda$ is the wavelength of light.

Figure 12 shows the results of this calculation at the lasing wavelengths for He-Ne and argon ion lasers, the two light sources used. The quantities calculated were the extinction and the scattering efficiencies and the differential scattering cross section as a function of angle (to obtain the scattered light intensity at 90° as a function of particle radius). Figure 13 shows the results for the relative scattered light intensity at 90° as a function of radius; the maximum of the first peak occurs at $r \approx 0.2$ μm. The peak of the sixth Mie oscillation occurs at $r \approx 0.95$ μm. Thus, based on this calculation, the positions of the Mie oscillations obtained as a function of residence time in the HTFFR apparatus are now calibrated for various silicon particle sizes. This is shown in Fig. 14 for 90° scattering data obtained at 200 Torr, 1173 K, a $SiH_4$ flow rate of $4.5 \times 10^{-5}$ mol $s^{-1}$, and a buffer gas velocity of 500 cm $s^{-1}$. Directly measured particle sizes obtained from SEM of silicon samples collected at various cooled inlet positions agree with the above calculations to within a few percent. This confirmation made it possible to be confident that simply counting the observed Mie oscillations and comparing them with the calculated curves (e.g., Fig. 13) was a valid means for determining the particle sizes.

The behavior of the Mie oscillations was also investigated in the region where the extinction efficiency approaches a value of 2. This occurs in the size region where the circumference of the particle is ≈ 10 times the probing wavelength. For 632.8 nm, this corresponds to a particle radius of 1.0 μm. For small attenuation the attenuated light intensity has a quadratic dependence on the particle radius (see Appendix A for a derivation):

$$I/I_o = 1 - (2\pi n\ell)r^2 \qquad (13)$$

where n is the particle number density and $\ell$ is the optical path length. Preliminary investigation of the extinction data for particle radii greater than 1 μm showed no obvious quadratic dependence of the attenuated light intensity on particle size. The implication of this result is that the particle number density is decreasing with increasing residence time in the HTFFR flow tube. Qualitatively, this conclusion is reinforced by the apparent decrease in both extinction and scattering intensities (cf. Fig. 14--the intensity is dependent upon n) with increasing residence time.

The conclusions about the growth of silicon particles produced by the thermal decomposition of silane are:

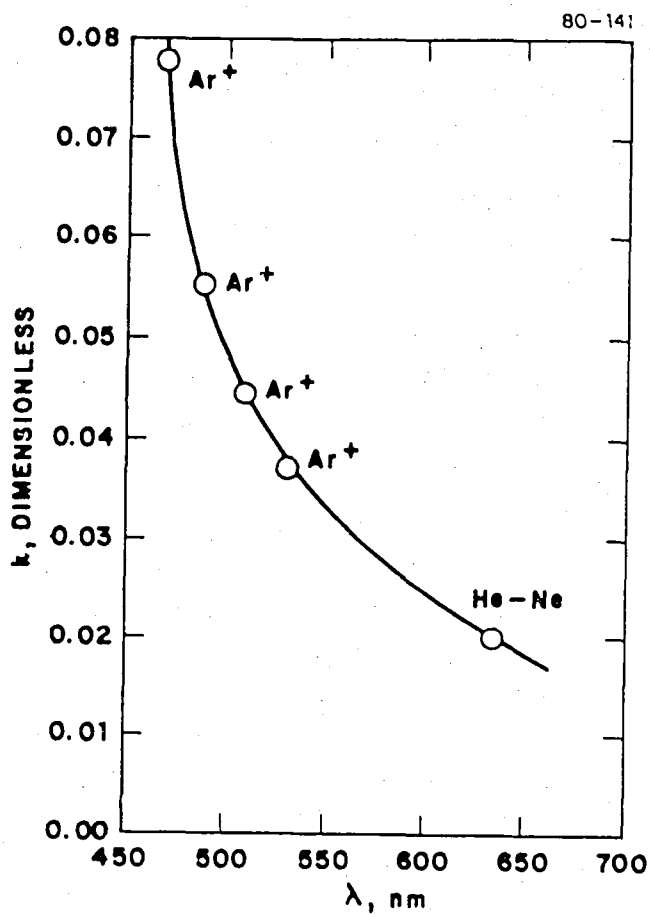


FIGURE 12 CALCULATED VARIATION OF EXTINCTION INDEX OF Si PARTICLES WITH WAVELENGTH

Points are wavelengths of lines emitted by the diagnostic lasers.

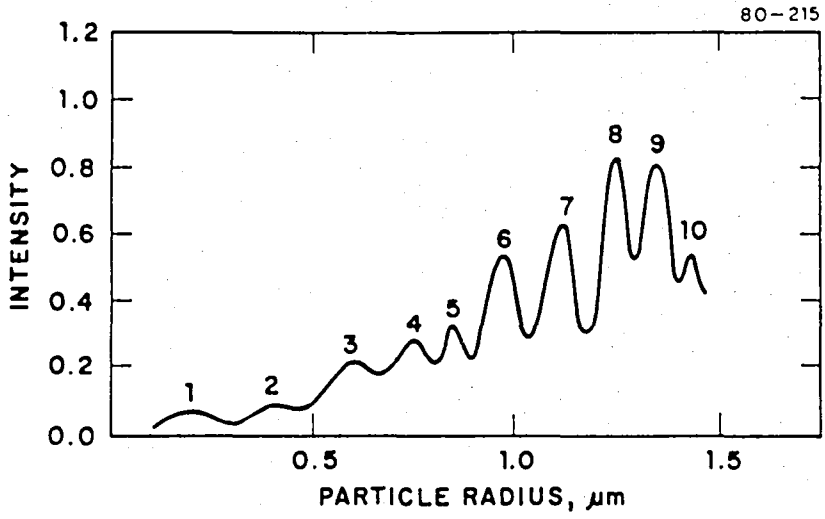


FIGURE 13 CALCULATED SCATTERED LIGHT INTENSITY AT 90° USING MIE THEORY

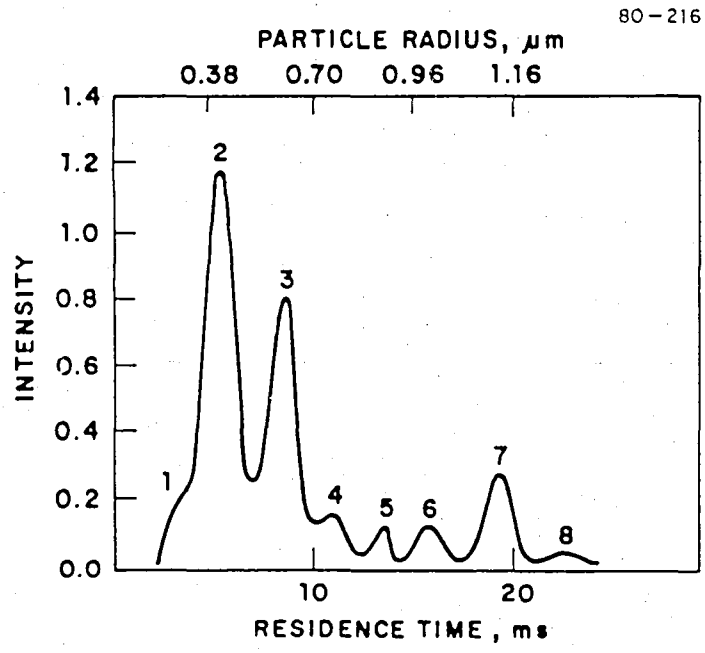


FIGURE 14 EXPERIMENTAL SCATTERED LIGHT INTENSITY AT 90° OBTAINED AT P = 200 TORR, T = 1173 K, AND $v = 500\ cm\ s^{-1}$

1. An initial growth of the particles occurs in an induction period of approximately 1 to 2 ms at 1200 K producing particles less than 0.05 μm radius.
2. The bulk of particle growth occurs in 1-20 ms after the induction period. The particles grow to ≈ 1 μm or larger in this period at a temperature of 1200 K.
3. The calibration of the Mie oscillations by Mie theory calculations agrees well with the determination of particle size by SEM.
4. The sharpness of the peaks in the Mie oscillations means that the particles have a highly monodisperse size distribution.
5. The decrease in both extinction and scattering intensities with residence time, and the lack of a quadratic dependence in the large particle radius attentuation data suggest a decrease in the particle concentrations with increasing residence time.

## C. PARTICLE GROWTH RATES

To obtain information about the particle formation and growth rates, light scattering data were obtained for total pressures of 120, 200, and 350 Torr and at temperatures of 873, 1173, and 1473 K. The best data were produced when the 514.5 nm $Ar^+$ laser line was used as the light source. This is because the Mie oscillations were more distinct at this wavelength. The Mie oscillations obtained with the 632.8 nm He-Ne laser were not as distinct. Consequently, little difference was observed in the particle growth rates for some of the 120 and 200 Torr data obtained using the He-Ne laser. Particle sizes were extracted by comparison with the computer calculations. The data given in Figs. 15-19 plot the particle growth rate as a function of time for the pressures 120, 200, and 350 Torr at temperatures of 873, 1173, and 1473 K. The data given in Figs. 20-22 plot the particle growth rate as a function of time for the temperatures 873, 1173, and 1473 K at pressures of 120, 200, and 350 Torr.

One general feature in all the data is apparent. The particle radius growth rate decreased with increasing residence time because the silane was being depleted while its mass deposition rate (proportional to $r^3$) was increasing. Thus, only the initial linear portion of the plots was used to obtain the particle

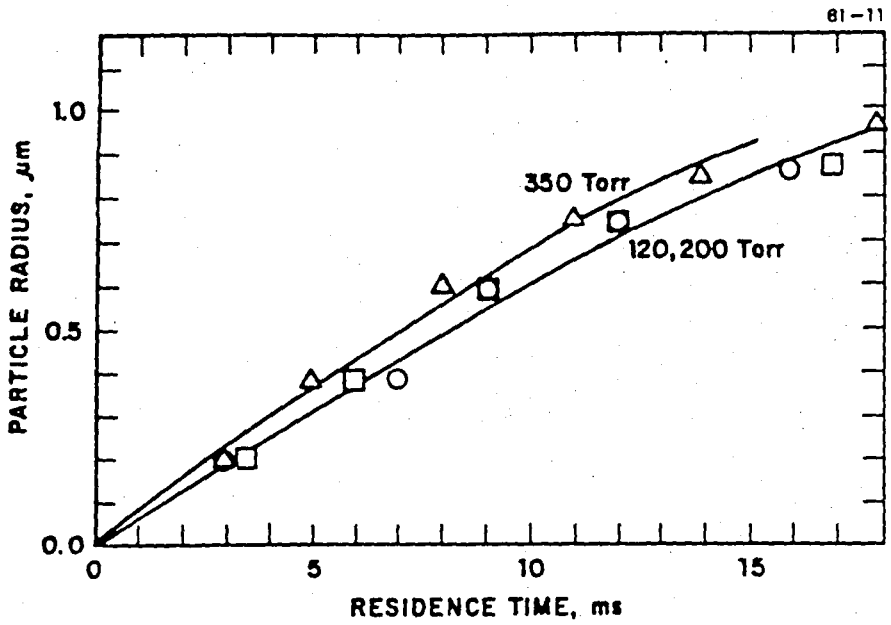


FIGURE 15 SILICON PARTICLE GROWTH RATES AT 873 K

Probe λ = 632.8 nm. Argon buffer gas pressures:
△-350 Torr, □- 200 Torr, ○- 120 Torr.

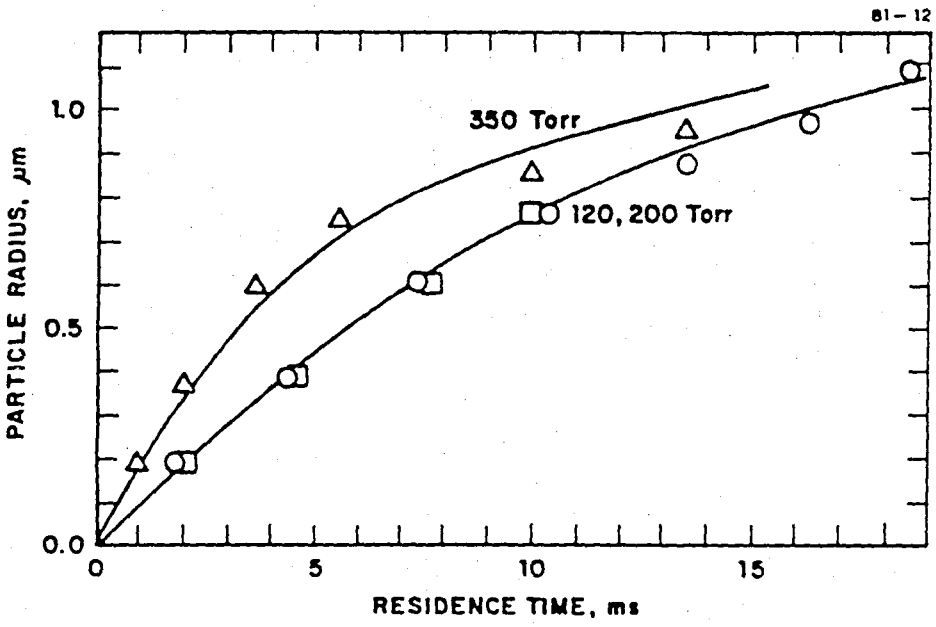


FIGURE 16 SILICON PARTICLE GROWTH RATES AT 1173 K

Probe λ = 632.8 nm. Argon buffer gas pressures:
△-350 Torr, □- 200 Torr, ○ - 120 Torr.

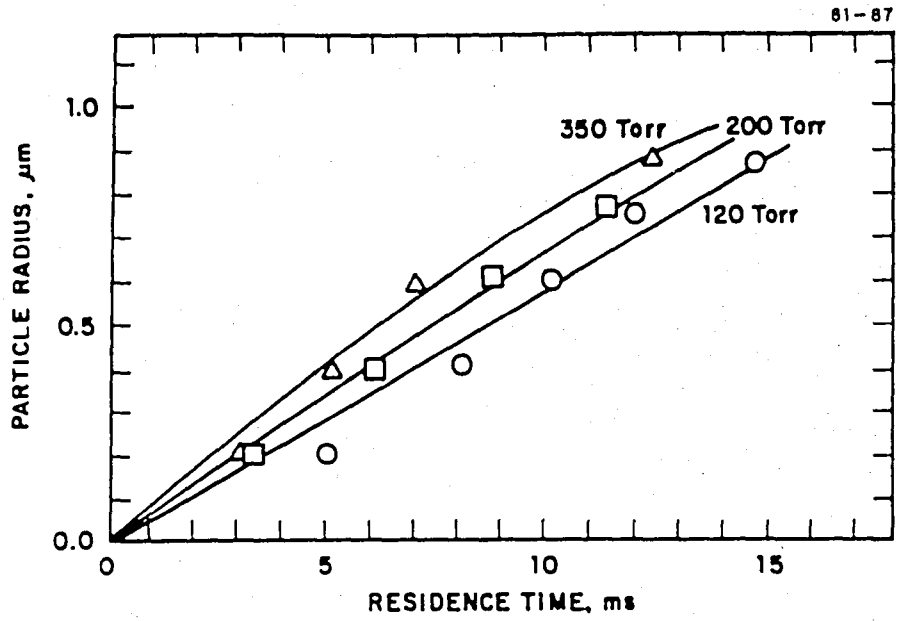


FIGURE 17 SILICON PARTICLE GROWTH RATES AT 873 K

Probe λ = 514.5 nm. Argon buffer gas pressures:
△-350 Torr, □- 200 Torr, ○- 120 Torr.

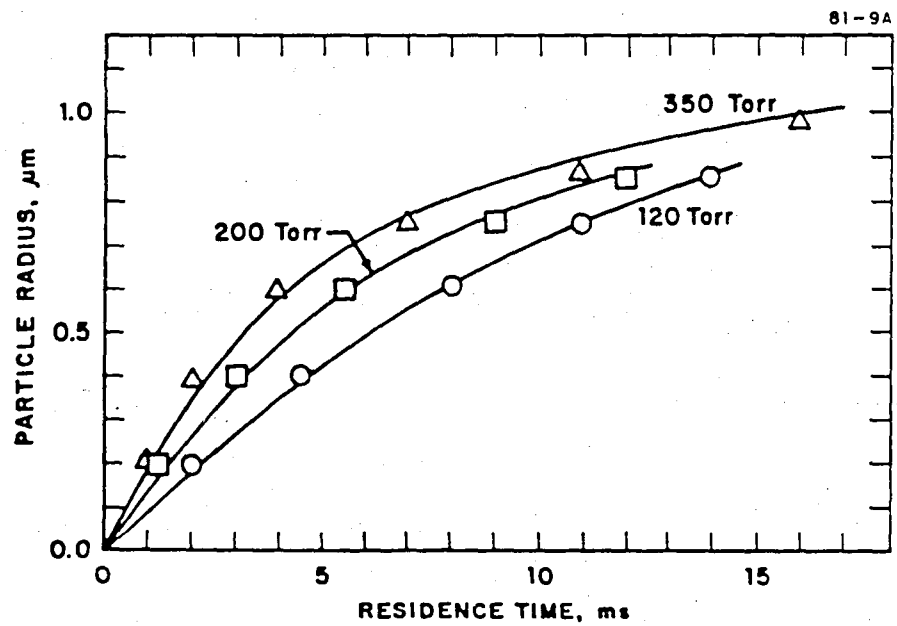


FIGURE 18 SILICON PARTICLE GROWTH RATES AT 1173 K

Probe λ = 514.5 nm. Argon buffer gas pressures:
△-350 Torr, □- 200 Torr, ○- 120 Torr.

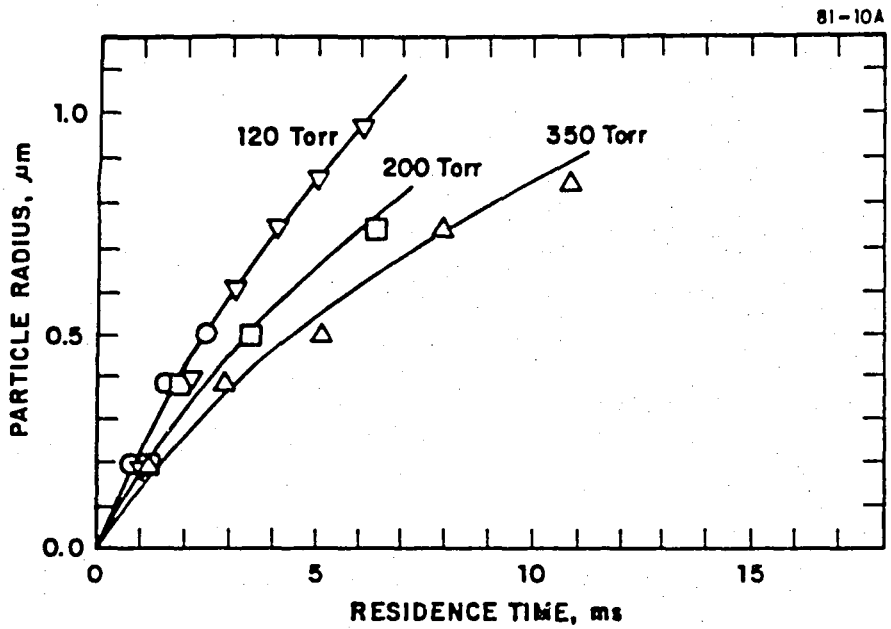


FIGURE 19 SILICON PARTICLE GROWTH RATES AT 1473 K

Probe λ = 632.8 nm. Argon buffer gas pressures: △ 350 Torr, □ 200 Torr, ○ 120 Torr; data at 120 Torr were also obtained at 514.5 nm - ▽

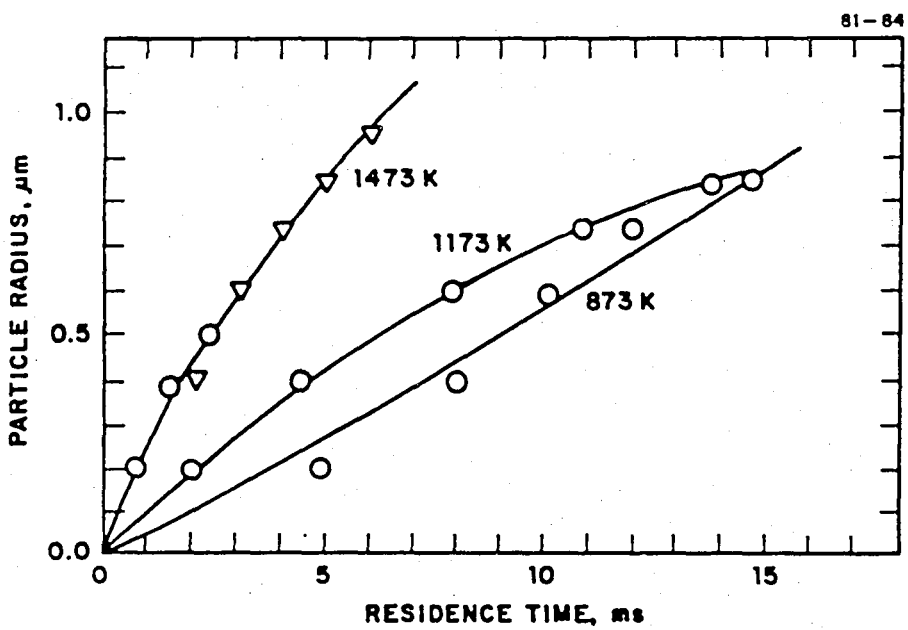


FIGURE 20 SILICON PARTICLE GROWTH RATES AT AN ARGON BUFFER GAS PRESSURE OF 120 TORR

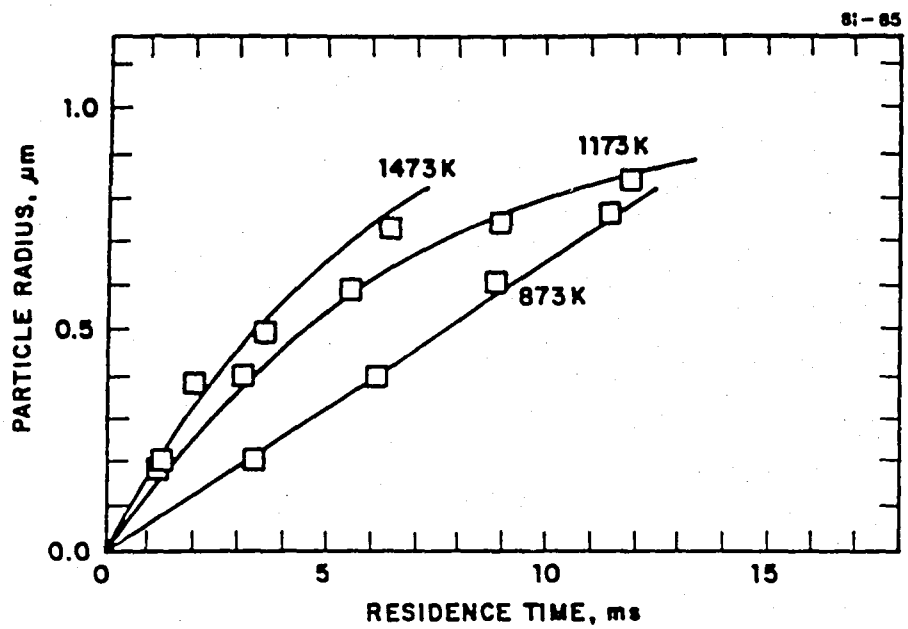


FIGURE 21 SILICON PARTICLE GROWTH RATES AT AN ARGON BUFFER GAS PRESSURE OF 200 TORR

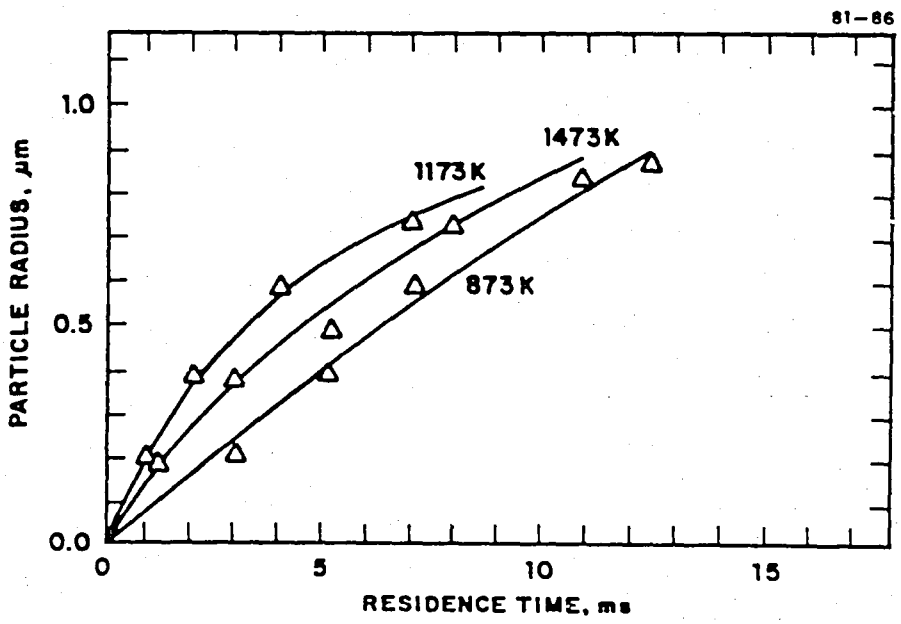


FIGURE 22 SILICON PARTICLE GROWTH RATES AT AN ARGON BUFFER GAS PRESSURE OF 350 TORR

rate ($k_r$ = dr/dt) for each of the pressures and temperatures listed above. These growth rates are summarized in Table I below:

TABLE I

SILICON PARTICLE GROWTH RATES OBTAINED FROM LIGHT SCATTERING DATA

| Pressure (Torr) | λ (nm) | $k_r$ at 873 K (μm $ms^{-1}$) | $k_r$ at 1173 K (μm $ms^{-1}$) | $k_r$ at 1473 K (μm $ms^{-1}$) |
|---|---|---|---|---|
| 120 | 514.5 | 0.055 | 0.084 | 0.225 |
| 120 | 632.8 | 0.058 | 0.092 | 0.225 |
| 200 | 514.5 | 0.069 | 0.124 | 0.16 |
| 200 | 632.8 | 0.064 | 0.084 | 0.16 |
| 350 | 514.5 | 0.078 | 0.176 | --- |
| 350 | 632.8 | 0.072 | 0.164 | 0.12 |

Several trends in the particle growth rates can be seen. Increasing the temperature increased the particle growth rate at argon pressures of 120 and 200 Torr. At 350 Torr, the particle growth rate showed a decrease at 1473 K. Increasing the pressure also increased the particle growth rate except at 1473 K were the growth rate decreased with increasing pressure. The anomalous results at 1473 K may suggest a different growth mechanism but they should be replicated before making further conclusions.

Figure 23 is an Arrhenius type plot of ln $k_r$ vs the reciprocal temperature. Because of the peculiarities at 1473 K, linear plots were not obtained. The breaks in the lines suggested by the 1173 K data may imply that two kinetic processes are occurring which become more apparent with increasing temperature. To properly evaluate these results more experimental work is needed.

Another experiment which provides information about particle growth rates is to vary the silane concentration. The relative intensity of scattered light was plotted as a function of silane concentration (varied over a factor of 10). This experiment was performed at 1173 K and 200 Torr by following the growth of particular oscillation peaks. The vertical axis in Fig. 24 gives the scattered light intensities for the second and third oscillation peaks which correspond to radii of 0.4 and 0.6 μm, respectively. Figure 25 gives the results for a large particle radius of 1.0 μm where the Mie oscillations are small and less distinct. The scattered intensity in these peaks is proportional to the number of particles and the size of the particles.

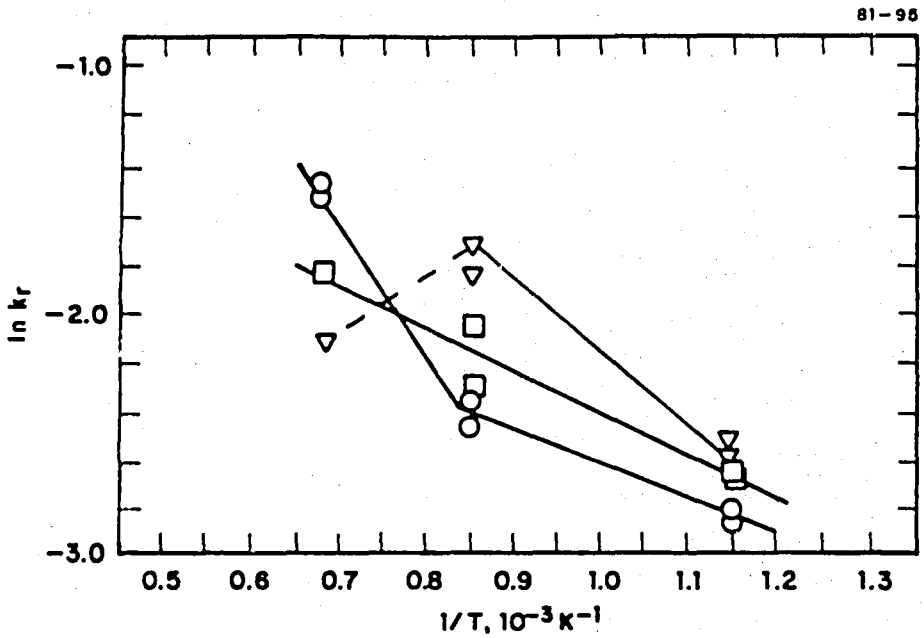


FIGURE 23 ARRHENIUS TYPE PLOT OF SILICON PARTICLE GROWTH RATES AT THREE PRESSURES

○ = 120 Torr; □ = 200 Torr; ▽ = 350 Torr. Two data points at each temperature are for different light scattering wavelengths (cf. Table I).

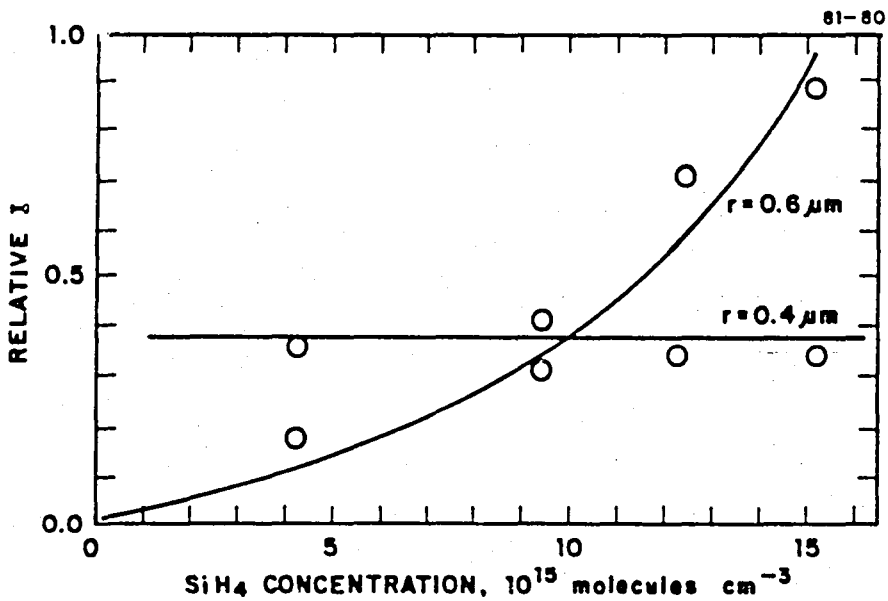


FIGURE 24 PLOT OF INTENSITY OF TWO DIFFERENT MIE OSCILLATION PEAKS CORRESPONDING TO TWO DIFFERENT PARTICLE RADII AS A FUNCTION OF SILANE CONCENTRATION AT 1173 K AND 200 TORR

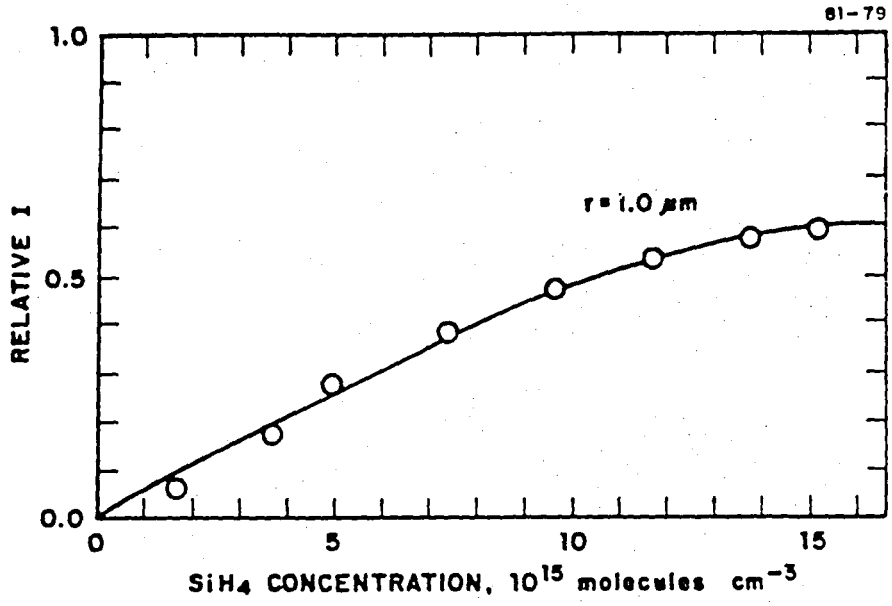


FIGURE 25 PLOT OF RELATIVE SCATTERED LIGHT INTENSITY AT 90° AS A FUNCTION OF SILANE CONCENTRATION FOR PARTICLES OF $r \approx 1.0$ μm

Thus, for a constant radius, the intensities indicate a change in the number of particles of a fixed radius. The time position of the oscillation peaks did not change with increasing silane concentration. This means that the rate of growth to that size did not change (within experimental error) with increasing silane concentration. The number of particles of r = 0.4 μm did not change with increasing silane concentration. However, the number of silane particles appears to reach an asymptotic value for the larger radii ( r = 0.6 μm and r = 1.0 μm). Thus, for the up to 1-2 μm radii particles observed here, there appears to be no limit to the size of particles which can be grown, but the number of the particles produced may be limited. The conclusions of the particle formation and growth studies are as follows:

1. Increasing the temperature from 873-1473 K at given bath gas pressures increases the particle growth rate. At 350 Torr and 1473 K there was a decrease in the observed particle growth rate.
2. Increasing the bath gas pressure at a constant temperature apparently increases the particle growth rate at 1173 K while the reverse appears true at 1473 K.
3. Increasing the initial silane concentration at a given pressure and temperature does not affect the particle growth rate.
4. Increasing the silane concentration increases the concentration of larger particles to a limiting value of the particle concentration.

## D. PARTICLE COLLECTION STUDIES

Particles produced by the thermal decomposition of silane in the HTFFR tube were collected in the observation zone for:

1. Scanning electron micrographs, to provide a verification of the Mie theory calculations used to calibrate the particle sizes determined from the light scattering data.
2. Some information on the morphology of the particles produced by the thermal decomposition of silane under controlled reaction conditions.
3. A semiquantitative estimate of particle concentration.

The silicon particles were collected at a bath gas pressure of 200 Torr, gas velocity of 500 cm $s^{-1}$, and temperatures of 873, 1173, and 1473 K, for various silane residence times in the HTFFR tube.

Experimentally, a 1/4 in. diam stainless steel tube was placed in the observation zone through one of the observation ports of the HTFFR apparatus (see Fig. 26) and some of the particle-laden gas stream was withdrawn through

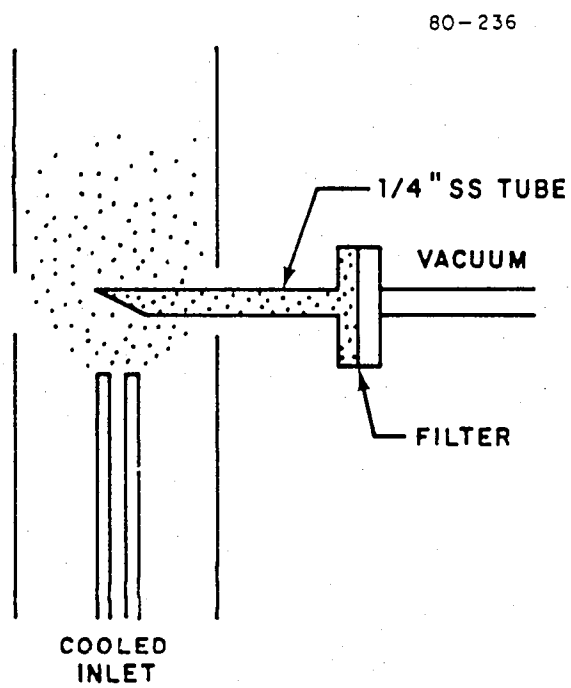


FIGURE 26 COLLECTION OF PARTICLES PRODUCED BY THE THERMAL DECOMPOSITION OF SILANE

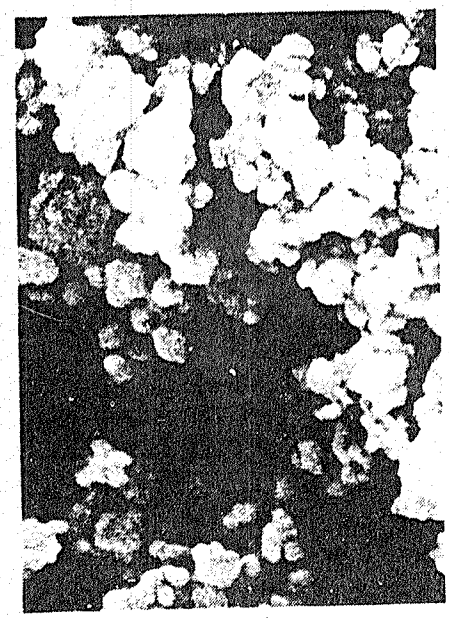

FIGURE 27 SEM OF SILICON PARTICLES THAT ARE ≈ 0.25 μm IN RADIUS

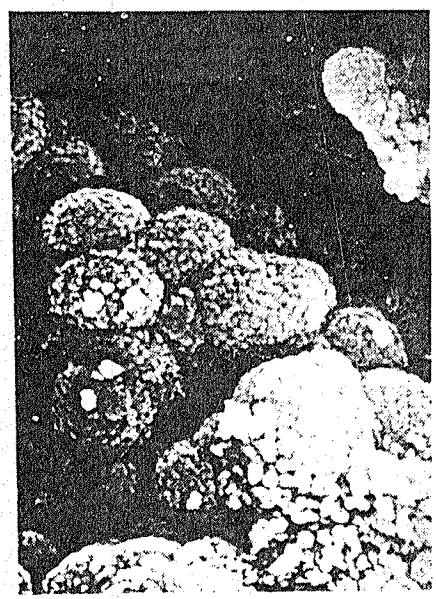

FIGURE 28 SEM OF SILICON PARTICLES THAT ARE ≈ 0.9 μm IN RADIUS

an external paper filter on which particles collected. Although it is perfectly adequate to provide samples for SEM sizing and morphology analysis this configuration is not ideal for particle concentration measurements. For more than the semiquantitative information desired here, a sampling cone designed to collect particles in the observation zone without disturbing the streamline flow of the gas is needed.

The SEMs (see Figs. 27 and 28) of the particles collected at residence times of 3 ms and 16 ms for the conditions of 200 Torr and 1173 K revealed that the particles were spherical in shape and monodisperse in size distributions, highly consistent with the light scattering observations. The radii of the particles from SEM ($\approx 0.25$ μm at 3 ms and $\approx 0.9$ μm at 16 ms) were in good agreement with results obtained from the light scattering measurements. The most interesting feature is that both the samples appear to consist of many smaller particles having radii $\approx 0.05$ μm. This observation, combined with the light scattering results, suggests an empirical model to explain both the homogeneous and heterogeneous particle growth kinetics; this is presented in Section II.H of this report.

## E. SEEDED PARTICLE STUDIES

To further understand the particle growth process, silicon seed particles were injected into the decomposing silane environment. The particles were injected into the HTFFR using a fluidized bed attachment as shown in Fig. 4. The particles were then collected using the procedure shown in Fig. 26. Two types of seed particles were used. A commercial sample obtained from Goodfellow Metals was composed of irregularly shaped silicon particles less than 5 μm in diameter. A second sample which had been produced using a free space reactor was obtained from JPL. These particles were $\approx 0.1$-$0.2$ μm in diameter.

The particles were subjected to temperatures of 873, 1173, and 1473 K at a constant pressure ($\approx 30$ Torr) and constant silane concentration ($\approx 1 \times 10^{16}$ molecule $cm^{-3}$). The seed particles were collected in the presence and in the absence of silane gas at a constant residence time of 10 ms and selected runs were subjected to scanning electron microscopy. The two temperature extremes of 873 K and 1473 K were chosen for the JPL and the nominal 5 μm seed samples.

Figure 29 is the SEM (3000x or 1 cm = 3.3 μm) for the nominal 5 μm diam particles which were collected after passing through a decomposing silane environment at 873 K. The original seed particles are no longer visible. Particle agglomerates (≈ 2 to 2.5 μm in diam) appear to cover the seed particles These particle agglomerates are composed of smaller 0.1 μm diam particles in a fashion similar to those displayed in Fig. 27. Large aggregates could be observed in other SEMs taken at lower magnification. They varied in size from 5 to 15 μm in diameter. Since individual large aggregates cannot be directly associated with an original seed particle size (the size distribution of the 5 μm particles varied widely), a growth rate could not be determined.

It appears that small 0.1 μm particles (on the 5 μm seed particles) grow to ≈ 2.0 μm diam in 10 ms. This corresponds roughly to the size of particles grown in the HTFFR for these conditions in the absence of seed particles. Both the 0.1 μm particles and the ≈ 2.0 μm particles appear in the photographs (Fig. 29) to have collected on the ≈ 5 μm seed particles. The actual size of the largest particles is unclear. The evidence for agglomeration is, however, apparent. Figure 30 shows the results for nominal 5 μm seed particles injected at 1473 K. The distinct particle shapes are ≈ 3 to 3.5 μm in radius. These particles are larger than those shown in Fig. 29 and they do not appear to be composed of smaller 0.1 μm particles. Again the original seed particles cannot be seen. Estimates of the ultimate particle diameters (seed + smaller agglomerates) are ≈ 10 to 15 μm. The smoothness of the distinct 3-3.5 μm particles may imply that vapor deposition rather than agglomeration is predominate. A combination of the two processes seems the most likely scenario.

Figure 31 shows the JPL-supplied seed particles which were subjected to a temperature of 873 K. Little growth seems to have occurred and no evidence of agglomeration is apparent. These particles are approximately 0.1 to 0.2 μm in diameter. However, Fig. 32 shows that the free space reactor seed particles have grown to ≈ 1.0 to 1.2 μm in diameter at 1473 K. This corresponds to a growth rate of ≈ 0.08-0.1 μm $ms^{-1}$. Again, there seems to be no evidence for agglomeration.

The conclusions of the seeded particle studies are:

1) Little growth occurs at 873 K while the particles grow at ≈ 0.04 to 0.05 μm in radius per millisecond at 1473 K.
2) There is little visual evidence for agglomeration at 1473 K, although some agglomeration may take place at 873 K.

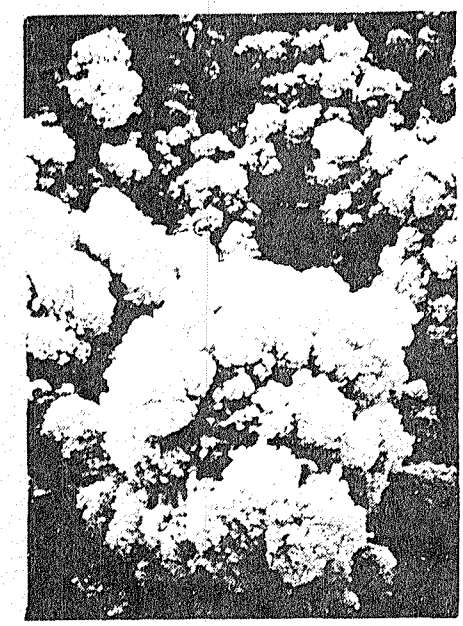

FIGURE 29 SEM (3000x) OF COLLECTED SILICON SEED PARTICLES (5 μm) EXPOSED TO DECOMPOSING SILANE ENVIRONMENT

T = 873 K, P = 30 Torr, residence time = 10 ms, initial $SiH_4$ concentration = $1 \times 10^{16}$ molecule $cm^{-3}$.

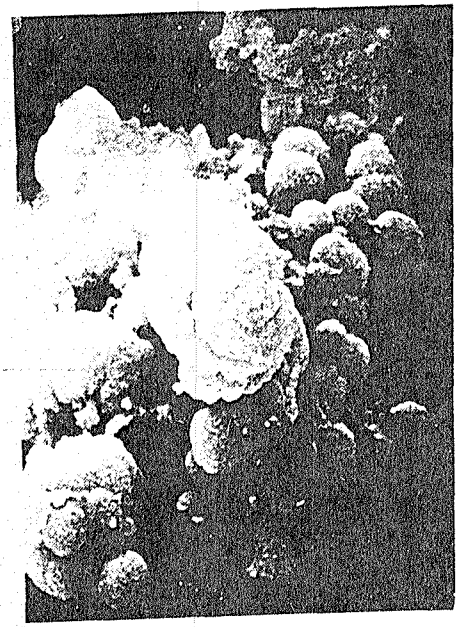

FIGURE 30 SEM (3000x) OF COLLECTED SILICON SEED PARTICLES (5 μm) EXPOSED TO DECOMPOSING SILANE ENVIRONMENT

T = 1473 K, P = 30 Torr, residence time = 10 ms, initial $SiH_4$ concentration = $1 \times 10^{16}$ molecule $cm^{-3}$.

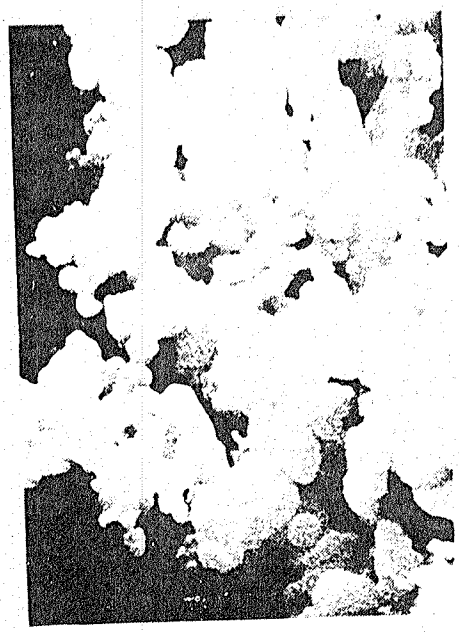

FIGURE 31 SEM (10,000x) of COLLECTED SILICON SEED PARTICLES (JPL SAMPLE) EXPOSED TO DECOMPOSING SILANE ENVIRONMENT

T = 873 K, P = 30 Torr, residence time = 10 ms, initial $SiH_4$ concentration = $1 \times 10^{16}$ molecule $cm^{-3}$.

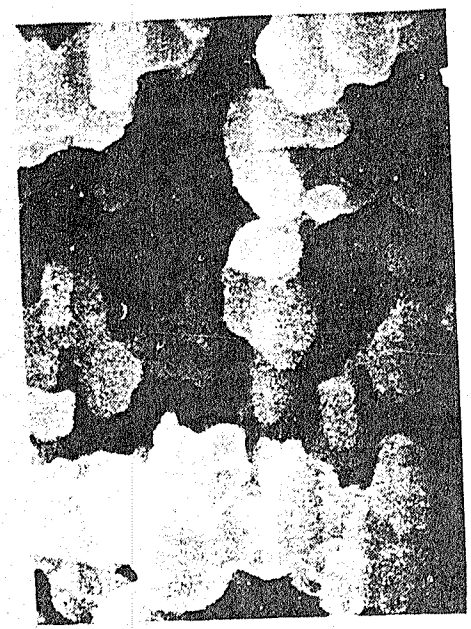

FIGURE 32 SEM (10,000x) OF COLLECTED SILICON SEED PARTICLES (JPL SAMPLE) EXPOSED TO DECOMPOSING SILANE ENVIRONMENT

T = 1473 K, P = 30 Torr, residence time = 10 ms, initial $SiH_4$ concentration = $1 \times 10^{16}$ molecule $cm^{-3}$.

## F. SILANE DECOMPOSITION STUDIES

The fraction of silane decomposed as a function of residence time was measured for the temperatures of 873, 1173, and 1473 K and for the pressures of 120, 200, and 350 Torr. The initial concentration of silane was kept constant at $0.96 \times 10^{16}$ cm$^{-3}$ for all of these experiments. To obtain a constant silane concentration a constant flow velocity of 500 cm s$^{-1}$ was used for these experiments. The velocity is given by

$$v = \frac{F}{A} \cdot \frac{T_{reac}}{P_{reac}} \cdot \frac{P_{STP}}{T_{STP}} \tag{14}$$

Here, F is the total gas flow rate, A is the flow tube cross sectional area (5.07 cm$^2$), $T_{reac}$ and $P_{reac}$ are the temperature and pressure of the reactor, and $T_{STP}$ and $P_{STP}$ are STP temperature and pressure. The silane concentration in the flow tube at temperature $T_{reac}$ ($[SiH_4]_o$) is given by

$$[SiH_4]_o = 9.65 \times 10^{18} \frac{P_{reac}}{T_{reac}} \left[\frac{F_1}{F_1 + F_2}\right] \tag{15}$$

The flow rate of silane is given by $F_1$ and the flow rate of argon is given by $F_2$. Thus, the term $F_1/F_1 + F_2$ is the mole fraction of silane present in the flow tube. To keep $[SiH_4]_o$ constant, this mole fraction must be changed. The amount of silane entering the flow tube was kept constant at 1 cm$^3$ s$^{-1}$ and the argon flow was adjusted to keep the gas velocity constant as the temperature and pressure were changed. The mole fraction but not the silane concentration measured in the long path absorption cell was the same as in the HTFFR tube, since the gas had cooled to approximately room temperature.

Since a portion ($\approx$12 cm) of the flow tube remained heated above the observation zone, this posed a problem in correlating this data to the particle growth rates. At a gas velocity of 500 cm s$^{-1}$, the position of the observation zone thus corresponded to a residence time of 24 ms. To obtain decomposition data at earlier times we increased the gas velocity to 1000 cm s$^{-1}$ and moved the cooled inlet above the observation zone data and thus obtained data down to 9.5 ms residence time.

The results of the silane decomposition measurements for 873 K and 1173 K are shown in Figs. 33 and 34, respectively. All of the data indicate an initial (residence time $\leq$ 10 ms) rapid increase in the rate of silane decomposition followed by a leveling-off. The exact nature of the initial

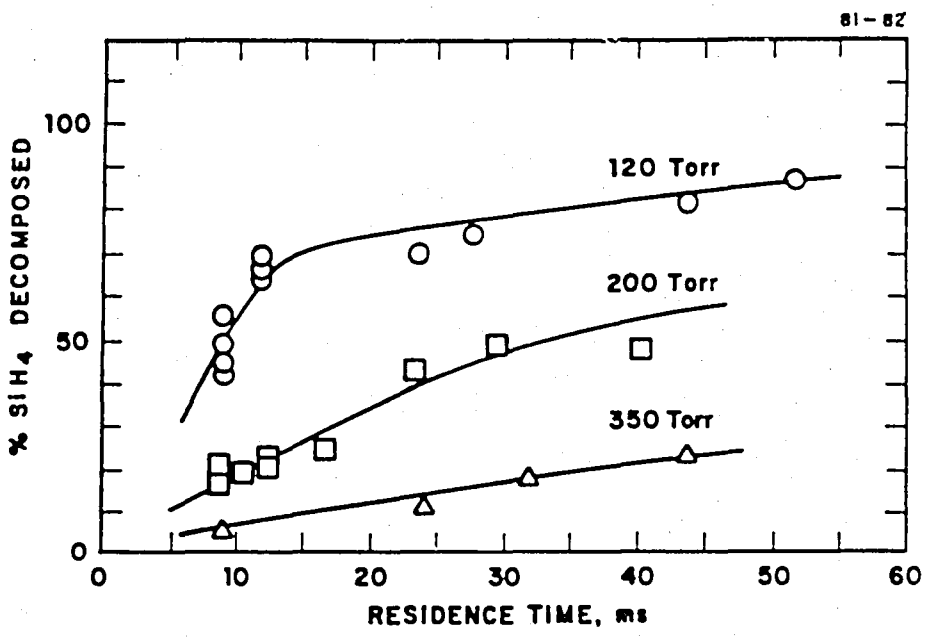


FIGURE 33 SILANE DECOMPOSITION AS A FUNCTION OF RESIDENCE TIME AT 873 K FOR VARIOUS ARGON BUFFER GAS PRESSURES

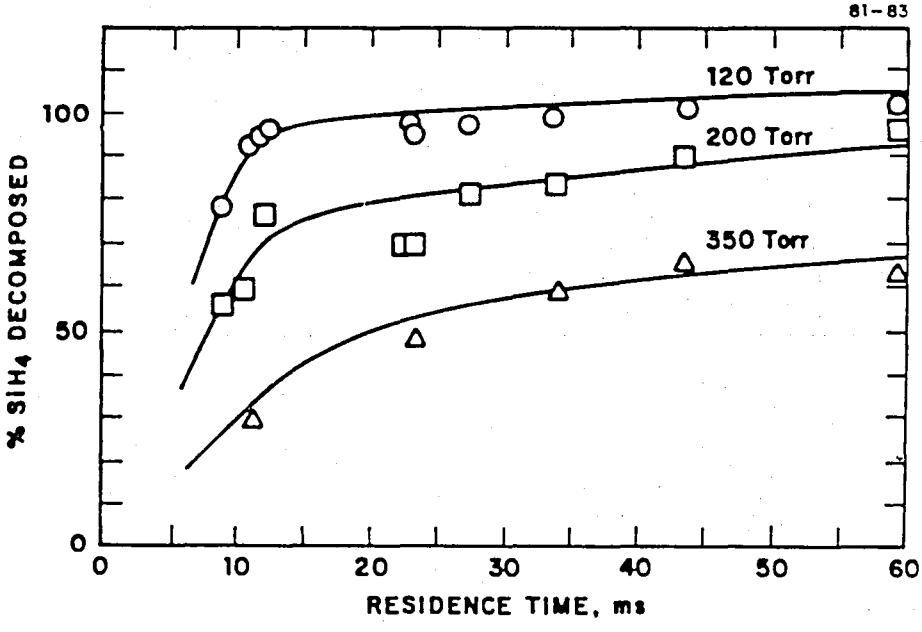


FIGURE 34 SILANE DECOMPOSITION AS A FUNCTION OF RESIDENCE TIME AT 1173 K FOR VARIOUS ARGON BUFFER GAS PRESSURES

increase could not be determined under the experimental conditions used due to apparatus pump speed limitations. The apparent inverse pressure dependence of the decomposition is presently unexplained; it seems reasonable to assume that all of the decomposition curves will eventually reach 100%. These two aspects of the decomposition measurements carry over into the calculations of particle density discussed in the following Section (II.G).

## G. PARTICLE CONCENTRATION STUDIES

The particle concentrations produced by the thermal decomposition of silane were determined as a function of time from the measured particle sizes combined with a measurement of the fraction of silane decomposed. The collection studies provided a semiquantitative check on the primary measurement. Both methods assumed that the particles were silicon. If the particles were $(SiH_2)_n$ polymers, a seven percent error would be introduced. However, the stoichiometry was probably something between pure Si and $(SiH_2)_n$ polymers, making this error considerably less. Both methods are also based on the assumption that a sphere of radius R is composed of smaller spheres of radius r(= 0.05 μm) considered to be in a close packing geometry.

The number of silicon atoms in a silicon sphere of radius r is given by

$$N_{Si}(r) = \frac{4/3\pi r^3}{V_{Si}} = \frac{4/3\pi r^3}{M/\rho N} \tag{16}$$

where $V_{Si}$ is the volume of a silicon atom calculated from the density of silicon ($\rho$), Avogadro's number (N), and the molecular weight of Si (M = 28 g $mol^{-1}$). The number of radius r spheres contained in a larger sphere of radius R is given by

$$N_r(R) = \left((4/3\pi R^3)/(4/3)\pi r^3)\right) \cdot 0.74 \tag{17}$$

The factor 0.74 accounts for hexagonal close packing of the smaller spheres. Thus, the number of silicon atoms in the spheres of radius R is

$$N_{Si}(R) = N_r(R) \cdot N_{Si}(r) = 0.74 \cdot (4/3\pi R^3) \cdot (\rho N/M) \tag{18}$$

To obtain the particle concentration, n(R) from the fraction of $SiH_4$ decomposed (method 1) the following mass balance expression is used:

$$n(R) = \frac{[SiH_4]_o f}{N_{Si}(R)} \tag{19}$$

where f is the fraction of silane decomposed (f values are taken from the curves of Figs. 33 and 34 and thus contain a pressure dependence and an early time ($\leq$ 10 ms) uncertainty) and $[SiH_4]_o$ is the initial silane concentration. The numerator represents the total number of silicon atoms available from the decomposition of silane and the denominator represents the number of atoms in a silicon sphere of radius R which is composed of smaller spheres of radius r.

Equation (9) was used to calculate the particle concentration as a function of residence time for the temperatures 873 and 1173 K and the pressures 120, 200, and 350 Torr. Insufficient particle growth data were available at 1473 K; thus no particle concentrations were determined at this temperature. Figures 35 and 36 show the calculated particle concentration as a function of residence time. The data and calculations for these plots are given in Appendix B. The dotted lines in the curves represent results based on straight line extrapolation (from 9.5 ms) to the origin in the silane decomposition data of Figs. 33 and 34.

The straight line plots of the reciprocal of the particle concentration vs residence time (Figs. 37 and 38) are consistent with a second order process for the decrease in the particle concentration. The slopes of these straight lines (the rate constants) are $\approx 10^{-3}$ cm$^3$ s$^{-1}$. However, typical coagulation constants for 0.1-1.0 μm radius smoke and aerosol particles at atmospheric pressure and room temperature are $10^{-10}$ to $10^{-9}$ cm$^3$ s$^{-1}$. While the reduced pressure and increased temperature in the HTFFR reactor should increase the coagulation rates, these effects would not produce an increase of six to seven orders of magnitude. Thus it seems unlikely that coagulation is causing the apparent decrease in particle concentration. The results may indicate that the density of the silicon particles is changing dramatically as the particles grow (the calculations assumed a constant value of 2.44 g cm$^{-3}$). These unexplained results emphasize the need for measurements of the particle concentration by more direct methods such as a forward light scattering technique.

During the preliminary experiments, the collection method (cf. Fig. 26, Section II.D) was used to make a crude estimate of the particle concentration. The following expression/calculation was used:

$$n = n_{atoms}/N_{Si}(R) \qquad (20)$$

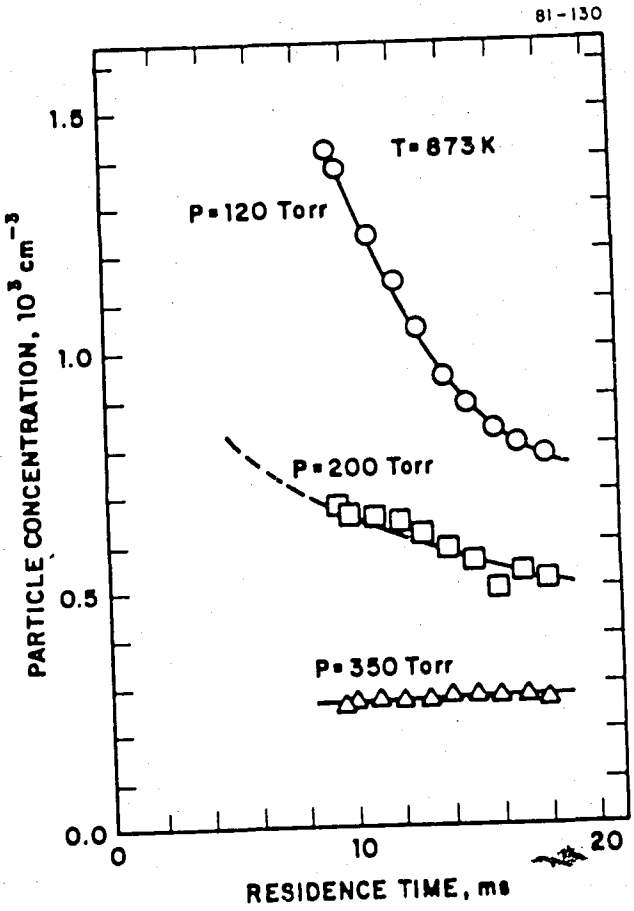


FIGURE 35 PARTICLE CONCENTRATION VS RESIDENCE TIME AT 873 K FOR VARIOUS ARGON BUFFER GAS PRESSURES

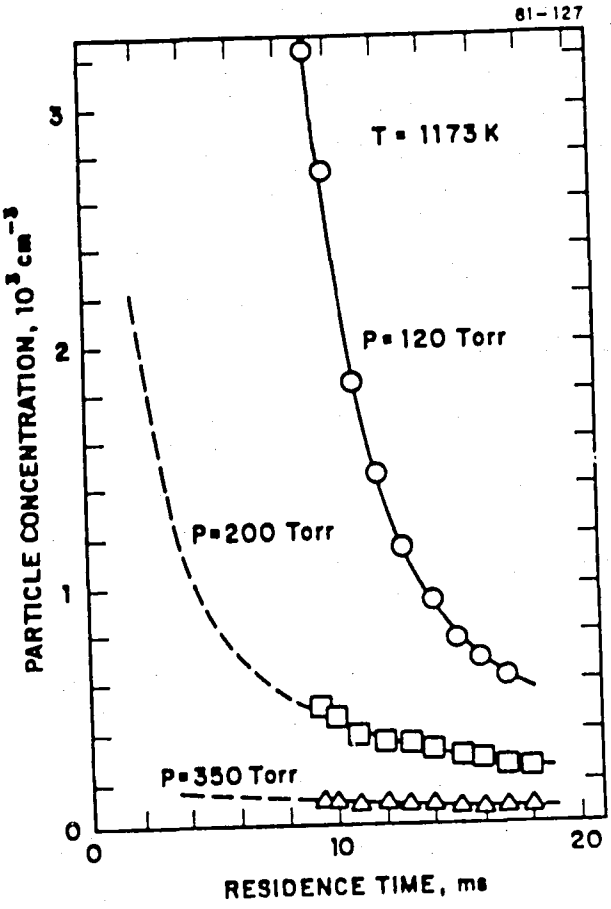


FIGURE 36 PARTICLE CONCENTRATION VS RESIDENCE TIME AT 1173 K FOR VARIOUS ARGON BUFFER GAS PRESSURES

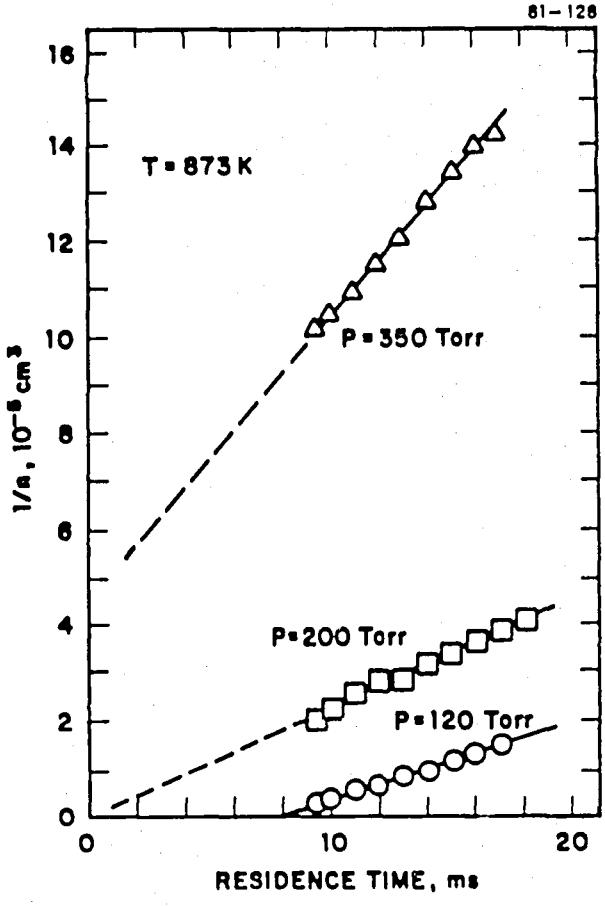


FIGURE 37 INVERSE OF PARTICLE CONCENTRATION VS RESIDENCE TIME AT 873 K

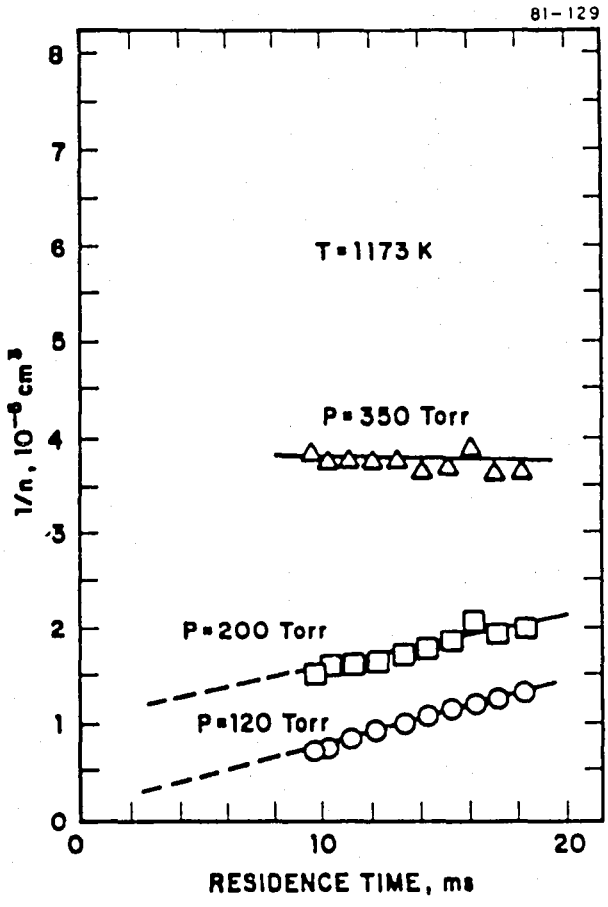


FIGURE 38 INVERSE OF PARTICLE CONCENTRATION VS RESIDENCE TIME AT 1173 K

Equation (18) gives a value for $N_{Si}(R)$ and $n_{atoms}$, the number of silicon atoms collected, is given by:

$$n_{atoms} = \left(\frac{w}{\Delta t}\right)\left(\frac{N}{M}\right)\cdot\frac{1}{va} \qquad (21)$$

where w is the mass collected in the time $\Delta t$, from a flow of velocity v impinging on a collecting tube of cross section area a ($\approx 0.32$ cm$^2$ in these experiments). Results obtained using the collection method (method 2) are displayed in Table II for the conditions $[SiH_4]_o = 1 \times 10^{16}$ cm$^{-3}$, P = 200 Torr, v = 500 cm s$^{-1}$.

TABLE II

PARTICLE CONCENTRATION IN HTFFR MEASURED BY COLLECTION

| T (K) | Residence Time (ms) | Particle Radius (μm) | n(R) (cm$^{-3}$) |
|---|---|---|---|
| 873 | 6 | 0.52 | $1.1 \times 10^3$ |
| 1173 | 3 | 0.25 | $2.7 \times 10^5$ |
| | 16 | 1.00 | $(2.7\text{-}3.3) \times 10^4$ |
| | 22 | 1.27 | $2.8 \times 10^4$ |
| 1473 | 6 | 0.60 | $9.9 \times 10^3$ |

Qualitatively, these results agree with those obtained from the fraction of silane decomposed, namely, the particle concentration decreased dramatically with time.

The conclusions of the particle concentration studies are:

1) The particle concentration reaches a very high initial value and is depleted by a second order mechanism, but this growth process does not appear to be coagulation.
2) Decreasing the pressure and temperature increases the particle concentration.

## H. PRELIMINARY MODEL

The scanning electron micrographs obtained on the collected particles indicated a cellular structure where the larger spheres were composed of many smaller 0.05 μm spheres. Nearly 100 small (0.05 μm radius) spheres are required to form a larger sphere 0.25 μm in radius (assuming hexagonal close packing of the spheres), and 4300 small spheres are required for a particle having a radius of 0.9 μm. This observation, combined with the present experimental results,

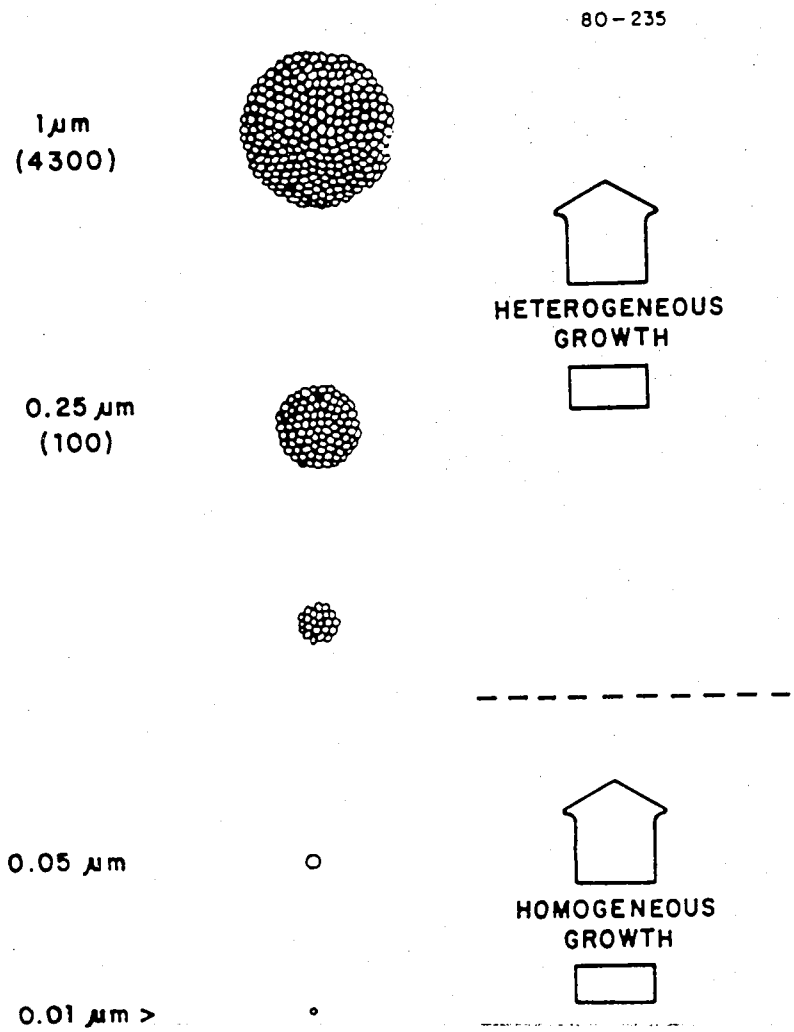


FIGURE 39 SCHEMATIC DRAWING REPRESENTING THE GROWTH OF SILICON PARTICLES PRODUCED BY THE THERMAL DECOMPOSITION OF SILANE

suggests a speculative model comprising both the homogeneous and heterogeneous particle growth kinetics.

Initial growth of the silicon particles began with the homogeneous nucleation of Si atom or $SiH_2$ molecules resulting from the thermal decomposition of silane. The particles continued to grow as spheres until they reached radii of approximately 0.05 μm. The mechanism of growth for these small spheres probably includes coagulation as suggested by Bauer and coworkers[7] and by Levin.[8] This growth is limited by a currently unknown mechanism which may be related to conditions that terminate the polymerization of $SiH_2$ species. This is the basis of the homogeneous particle growth process and the present results indicate that this growth is fast ($<$ 1 ms).

The continued growth of the small particles is then described by unknown heterogeneous processes which require several milliseconds for the spheres to grow to radii of $\approx$ 1.0 μm.

Speculation based on preliminary results indicates that this process proceeds by a condensation mechanism. However, a simple gas-particle condensation mechanism cannot account for the decrease in the particle concentration as a function of time, and as shown in Section II.G, a coagulation mechanism is unlikely because it would require physically unrealistic rate constants to account for the observations. Thus, the exact nature of the growth process remains unknown. In principle, this growth can continue indefinitely provided sufficient $SiH_4$ is present. Thus, the homogeneous process is described by a rapid growth of one sphere and the heterogeneous process is described by a slower growth of many small spheres from the surface of the "seed" sphere as depicted in Fig. 39.

## I. ATOMIC AND MOLECULAR DECOMPOSITION SPECIES

Attempts were made to observe Si atoms and SiH, $SiH_2$, and $Si_2H_6$ molecular species which may result from the thermal decomposition of silane. A resonance absorption technique was used to probe for Si atoms and a laser resonance fluorescence technique was used to probe for the various molecular species. No conclusive results were obtained from these experiments.

To probe for the Si atoms, the existence of particles makes an observation experiment difficult. This is because the amount of light scattered by the particles will be much greater than the light absorbed by any silicon

atoms present. This difficulty was overcome by probing for silicon by using two wavelengths (251.6 and 288.2 nm) of the resonance lamp. The 251.6 nm resonance line results from a 4 $^3P$-3 $^3P^o$ transition where the 3 $^3P$ level is 223 $cm^{-1}$ above the ground state. At several hundred degrees K, this level will be thermally populated and absorption due to silicon atoms can be observed. The 288.2 nm line, however, is a $^1D$-$^1P^o$ line where the $^1P^o$ state is 6299 $cm^{-1}$ above the ground state. It will not be thermally populated, and no absorption will take place due to the presence of Si atoms. Thus, the 288.2 nm line represents a light intensity extinction due to particle scattering only, while the 251.6 nm line represents a light extinction due to particle scattering and silicon atom absorption. Experiments consisted of measuring the transmitted light intensity at 251.6 nm and 288.2 nm as silane was decomposed at 873 K and 1173 K. No evidence for absorption by silicon atoms could be found, but the "noise" of the experiment was sufficient to not exclude the possibility of the existence of Si atoms. Thus, the experiments were inconclusive.

To probe for the molecular species, laser resonance fluorescence experiments were attempted. In a laser resonance fluorescence experiment, a laser line coincides with an electronic transition between a vibrational level in the ground state with a vibrational level in the excited state. Since the vibrational levels often contain many rotational levels, this chance coincidence is not so unusual for molecules. If the laser light is absorbed, emission occurs at many wavelengths and a vibrational sequence can usually be observed with a spectrometer. This vibrational sequence is characteristic of each particular molecule. Thus, it would be possible to determine whether SiH, $SiH_2$, or $Si_2H_6$ molecules were present. The 514.5 nm and 477.0 nm lines of the argon ion laser were used to attempt to produce resonance fluorescence since these molecules have some vibrational bands that overlap with the energy corresponding to those wavelengths. Noisy spectra were obtained, but these were proven to be scattered laser light. Lasers are so intense that often scattered laser light inside the spectrometer misses the grating giving rise to "spectra". A 514.5 nm bandpass filter was placed in front of the exit slits of the spectrometer. This meant that only 514.5 nm light could be observed by the PMT. The spectrometer was scanned from 700–500 nm and various peaks were obtained. Since less than 0.1% of the light at wavelengths other than 514.5 nm should get through the filter, these peaks at "other" wavelengths are only scattered 514.5 nm laser light. The intensity variation is due to the rotation of the



C-2

grating which is reflecting the laser light in a variable fashion. Thus, no conclusive evidence was obtained for the presence or absence of the molecular species.

## III. RECOMMENDATIONS

Several results appear to be directly applicable to the free space reactor and fluidized bed processes for producing silicon by the thermal decomposition of silane. These are:

1. Increasing the temperature increases the particle growth rate.
2. Increasing the silane concentration does not affect the particle growth rate under the conditions of the present measurements. Thus there may be an optimum silane concentration above which further increases do not increase the growth rate proportionately.
3. Increasing the silane concentration increases the concentration of silicon particles to a limiting value.
4. Seeded particles grow faster at higher temperatures.

Thus, increasing the temperature to the highest possible value in the manufacturing process will increase the throughput. There may be an optimum silane concentration which if increased will not increase the process yield. No indications were found that a limitation on the particle size exists, only a limitation on the concentration of the particles. Thus, it may be that decreasing the silane concentration in the manufacturing process will lead to fewer particles of a larger size. Finally, if seeded particles are used, increasing the temperature will favor the best growth.

Several detailed mechanistic questions remain unanswered. More research is needed to explore the initial phases of particle growth, the anomalies seen in the particle growth rates at 1473 K, the observed pressure dependence of silane decomposition, and the reasons for the apparent decrease in particle concentrations with residence time. The present program has shown the utility of the HTFFR technique for addressing these basic questions and for providing process-useful information. The results described are in need of clarification which can be provided by further experimental work.

## IV. NEW TECHNOLOGY

The fluidized bed for dispersing a powder in a gas stream has been identified as New Technology. This item is described on page 7 and Fig. 4 (page 9). It was disclosed to JPL on 26 January 1981.

## V. REFERENCES


1. Hogness, T.R., Wilson, T.L., and Johnson, W.C., J. Am. Chem. Soc. 58, 108 (1936).
2. Stokland, K., Det. K. noiske Vidensh. Selsk. Skr. 3, (1948).
3. Purnell, J.H. and Walsh, R., Proc. Roy. Soc. A293, 543 (1966).
4. Newman, C.G., Ring, M.A., and O'Neal, H.E., J. Am. Chem. Soc. 100, 5945 (1978).
5. Newman, C.G., Ring, M.A., Leska, D., and Shipley, N., Int. J. Chem. Kinet. 11, 1167 (1979).
6. Neudorfl, P., Jodhan, A., and Strausz, O.P., J. Phys. Chem. 84, 338 (1980).
7. Tabayashi, K. and Bauer, S.H., Twelfth International Symposium on Shock Tubes and Waves (The Magnus Press, The Hebrew University, Jerusalem, 1980).
8. Levin, H., "Proceedings of Symposium on Materials and New Processing Technologies for Photovoltaics," Electrochemical Society, 1980.
9. Fontijn, A., and Felder, W., "High Temperature Flow Tubes. Generation and Measurement of Refractory Species," in Reactive Intermediates in the Gas Phase, D.W. Setser, Ed. (Academic Press, New York, 1979) Chap. 2.
10. Kerker, M., The Scattering of Light and Other Electromagnetic Radiation (Academic Press, New York, 1969).
11. Van de Hulst, H.C., Light Scattering by Small Particles (Wiley, New York, 1957).
12. Vietti, M.A., and Schuster, B.G., J. Chem. Phys. 58, 434 (1973).
13. Dash, W.C., and Newmann, R., Phys. Rev. 99, 1151 (1955).

# APPENDIX A

The extinction of light is given by

$$\frac{I}{I_o} = e^{-\tau \ell} = e^{-(n \ell C_{ext})} \tag{A1}$$

where $\tau$ is the turbidity, $\ell$ is the light path length, $C_{ext}$ is the extinction cross section, and n is the concentration of particles contained in the volume intercepted by the light beam. For small attenuation, i.e., $I/I_o \approx 0.9$, it is possible to expand the exponential to obtain

$$\frac{I}{I_o} = 1 - (n \ell C_{ext}) \tag{A2}$$

In the region where the circumference of the particle is $\approx 10$ times the probing wavelength (632.8 nm), the efficiency factor approaches a value of 2, i.e.,

$$Q_{ext} = \frac{C_{ext}}{\pi r^2} \approx 2 \tag{A3}$$

or

$$C_{ext} = 2\pi r^2$$

substituting into Eq. (A2)

$$\frac{I}{I_o} = 1 - (2\pi n \ell) r^2 \tag{A4}$$

Thus, the attenuated light intensity exiting from a volume of particles which scatters and absorbs light will show a quadratic dependence on r in the region where $2\pi r/\lambda$ approaches 10.

## APPENDIX B

The following constants were used to obtain the silicon particle concentrations in Tables B-I through B-VI:

$$\rho = 2.44 \text{ g cm}^{-3}$$

$$N = 6.02 \times 10^{23} \text{ atom mol}^{-1}$$

$$M = 28 \text{ g mol}^{-1}$$

$$\pi = 3.1416$$

$$[SiH_4]_o = 0.96 \times 10^{16} \text{ molecule cm}^{-3}$$

The number of silicon atoms per $cm^3$ ($N_{Si}$) is obtained from the fraction of silane decomposed (f) for a given temperature and pressure.

$$N_{Si} = [SiH_4]_o \cdot f \qquad \text{(B-1)}$$

The number of silicon atoms per particle of radius R is given by

$$N_{Si}(R) = \left(0.74 \cdot \frac{4}{3} \pi \frac{\rho N}{M}\right) R^3 \qquad \text{(B-2)}$$

The total number of silicon particles of radius R per $cm^3$ is given by

$$n = \frac{N_{Si}}{N_{Si}(R)} \qquad \text{(B-3)}$$

This is Eq. (20) of Section II.G.

TABLE B-I. PARTICLE CONCENTRATION CALCULATION

T = 873 K  $v$ = 500 cm $s^{-1}$

P = 120 Torr  $[SiH_4]_o = 0.96 \times 10^{16}$ molecule $cm^{-3}$

| Residence Time (ms) | Fraction of $SiH_4$ Decomposed f | Number of Si Atoms Produced ($10^{16} cm^{-3}$) | Particle Radius at Time t (μm) | Number of Atoms/ Particles of Radius r $10^{11}$ atoms | Total Number of Si Particles $cm^{-3}$ of Radius R $10^5$ particles $cm^{-3}$ | $\frac{1}{n}$ $10^{-5}$ $cm^3$ |
|---|---|---|---|---|---|---|
| 9.5 | 0.505 | 0.485 | 0.45 | 0.149 | 3.26 | 0.31 |
| 10 | 0.58 | 0.557 | 0.50 | 0.204 | 2.73 | 0.37 |
| 11 | 0.61 | 0.586 | 0.58 | 0.319 | 1.84 | 0.54 |
| 12 | 0.65 | 0.624 | 0.64 | 0.428 | 1.46 | 0.68 |
| 13 | 0.68 | 0.653 | 0.70 | 0.560 | 1.16 | 0.86 |
| 14 | 0.70 | 0.672 | 0.76 | 0.717 | 0.94 | 1.06 |
| 15 | 0.71 | 0.682 | 0.81 | 0.868 | 0.786 | 1.27 |
| 16 | 0.72 | 0.691 | 0.85 | 1.00 | 0.691 | 1.45 |
| 17 | 0.73 | 0.701 | 0.88 | 1.11 | 0.632 | 1.58 |

TABLE B-II. PARTICLE CONCENTRATION CALCULATION

T = 873 K  v = 500 cm $s^{-1}$

P = 200 Torr  $[SiH_4]_o$ = 0.96 × $10^{16}$ molecule $cm^{-3}$

| Residence Time (ms) | Fraction of $SiH_4$ Decomposed f | Number of Si Atoms Produced ($10^{16} cm^{-3}$) | Particle Radius at Time t (μm) | Number of Atoms/ Particles of Radius r $10^{11}$ atoms | Total Number of Si Particles $cm^{-3}$ of Radius R $10^5$ particles $cm^{-3}$ | $\frac{1}{n}$ $10^{-5} cm^3$ |
|---|---|---|---|---|---|---|
| 9.5 | 0.18 | 0.173 | 0.60 | 0.353 | 0.490 | 2.04 |
| 10 | 0.19 | 0.182 | 0.63 | 0.409 | 0.445 | 2.25 |
| 11 | 0.205 | 0.197 | 0.68 | 0.514 | 0.383 | 2.61 |
| 12 | 0.22 | 0.211 | 0.72 | 0.609 | 0.346 | 2.89 |
| 13 | 0.24 | 0.230 | 0.74 | 0.662 | 0.347 | 2.88 |
| 14 | 0.25 | 0.240 | 0.78 | 0.775 | 0.310 | 3.23 |
| 15 | 0.27 | 0.259 | 0.82 | 0.901 | 0.287 | 3.48 |
| 16 | 0.28 | 0.269 | 0.85 | 1.00 | 0.269 | 3.71 |
| 17 | 0.295 | 0.283 | 0.88 | 1.11 | 0.255 | 3.92 |
| 18 | 0.31 | 0.298 | 0.91 | 1.23 | 0.242 | 4.13 |

TABLE B-III. PARTICLE CONCENTRATION CALCULATION

T = 873 K $v = 500\ cm\ s^{-1}$

P = 350 Torr $[SiH_4]_o = 0.96 \times 10^{16}$ molecule $cm^{-3}$

| Residence Time (ms) | Fraction of $SiH_4$ Decomposed f | Number of Si Atoms Produced ($10^{16} cm^{-3}$) | Particle Radius at Time t (μm) | Number of Atoms/ Particles of Radius r $10^{11}$ atoms | Total Number of Si Particles $cm^{-3}$ of Radius R $10^5$ particles $cm^{-3}$ | $\frac{1}{n}$ $10^{-5} cm^3$ |
|---|---|---|---|---|---|---|
| 9.5 | 0.05 | 0.048 | 0.67 | 0.491 | 0.098 | 10.20 |
| 10 | 0.055 | 0.053 | 0.70 | 0.560 | 0.095 | 10.53 |
| 11 | 0.06 | 0.058 | 0.73 | 0.636 | 0.091 | 10.99 |
| 12 | 0.065 | 0.062 | 0.76 | 0.717 | 0.086 | 11.63 |
| 13 | 0.07 | 0.067 | 0.79 | 0.806 | 0.083 | 12.05 |
| 14 | 0.075 | 0.072 | 0.83 | 0.934 | 0.077 | 12.99 |
| 15 | 0.08 | 0.077 | 0.86 | 1.04 | 0.074 | 13.51 |
| 16 | 0.085 | 0.082 | 0.89 | 1.15 | 0.071 | 14.08 |
| 17 | 0.09 | 0.086 | 0.91 | 1.23 | 0.070 | 14.29 |

TABLE B-IV. PARTICLE CONCENTRATION CALCULATION

$T = 1173$ K  $v = 500$ cm $s^{-1}$

$P = 120$ Torr  $[SiH_4]_o = 0.96 \times 10^{16}$ molecule $cm^{-3}$

| Residence Time (ms) | Fraction of $SiH_4$ Decomposed f | Number of Si Atoms Produced ($10^{16} cm^{-3}$) | Particle Radius at Time t (μm) | Number of Atoms/ Particles of Radius r $10^{11}$ atoms | Total Number of Si Particles $cm^{-3}$ of Radius R $10^5$ particles $cm^{-3}$ | $\frac{1}{n}$ $10^{-5} cm^3$ |
|---|---|---|---|---|---|---|
| 9.5 | 0.80 | 0.760 | 0.69 | 0.534 | 1.42 | 0.70 |
| 10 | 0.86 | 0.817 | 0.71 | 0.585 | 1.40 | 0.71 |
| 11 | 0.90 | 0.855 | 0.75 | 0.689 | 1.24 | 0.81 |
| 12 | 0.94 | 0.893 | 0.78 | 0.775 | 1 | 0.87 |
| 13 | 0.96 | 0.912 | 0.81 | 0.868 | | 0.95 |
| 14 | 0.97 | 0.922 | 0.84 | 0.968 | | 1.05 |
| 15 | 0.975 | 0.923 | 0.86 | 1.04 | 0.89 | 1.12 |
| 16 | 0.98 | 0.931 | 0.88 | 1.11 | 0.84 | 1.19 |
| 17 | 0.98 | 0.931 | 0.89 | 1.15 | 0.81 | 1.23 |
| 18 | 0.985 | 0.936 | 0.90 | 1.19 | 0.79 | 1.27 |

TABLE B-V. PARTICLE CONCENTRATION CALCULATION

T = 1173 K  v = 500 cm $s^{-1}$

P = 200 Torr  $[SiH_4]_o$ = 0.96 × $10^{16}$ molecule $cm^{-3}$

| Residence Time (ms) | Fraction of $SiH_4$ Decomposed f | Number of Si Atoms Produced ($10^{16} cm^{-3}$) | Particle Radius at Time t (μm) | Number of Atoms/ Particles of Radius r $10^{11}$ atoms | Total Number of Si Particles $cm^{-3}$ of Radius R $10^{3}$ particles $cm^{-3}$ | $\frac{1}{n}$ $10^{-3} cm^3$ |
|---|---|---|---|---|---|---|
| 9.5 | 0.270 | 0.26 | 0.85 | 1.00 | 0.260 | 3.85 |
| 10 | 0.300 | 0.29 | 0.87 | 1.08 | 0.269 | 3.72 |
| 11 | 0.325 | 0.31 | 0.89 | 1.15 | 0.269 | 3.72 |
| 12 | 0.350 | 0.34 | 0.92 | 1.27 | 0.268 | 3.73 |
| 13 | 0.380 | 0.365 | 0.94 | 1.36 | 0.268 | 3.73 |
| 14 | 0.410 | 0.394 | 0.955 | 1.42 | 0.277 | 3.61 |
| 15 | 0.430 | 0.413 | 0.97 | 1.49 | 0.277 | 3.61 |
| 16 | 0.460 | 0.442 | 0.98 | 1.54 | 0.289 | 3.84 |
| 17 | 0.470 | 0.452 | 0.99 | 1.59 | 0.284 | 3.52 |
| 18 | 0.480 | 0.461 | 1.00 | 1.63 | 0.283 | 3.53 |

TABLE B-VI. PARTICLE CONCENTRATION CALCULATION

$T = 1173$ K $\quad v = 500$ cm $s^{-1}$

$P = 200$ Torr $\quad [SiH_4]_o = 0.96 \times 10^{16}$ molecule $cm^{-3}$

| Residence Time (ms) | Fraction of $SiH_4$ Decomposed f | Number of Si Atoms Produced ($10^{16} cm^{-3}$) | Particle Radius at Time t ($\mu m$) | Number of Atoms/ Particles of Radius r $10^{11}$ atoms | Total Number of Si Particles $cm^{-3}$ of Radius R $10^{5}$ particles $cm^{-3}$ | $\frac{1}{n}$ $10^{-5} cm^3$ |
|---|---|---|---|---|---|---|
| 9.5 | 0.585 | 0.562 | 0.80 | 0.837 | 0.671 | 1.49 |
| 10 | 0.615 | 0.590 | 0.82 | 0.901 | 0.655 | 1.53 |
| 11 | 0.655 | 0.629 | 0.84 | 0.968 | 0.650 | 1.54 |
| 12 | 0.700 | 0.672 | 0.86 | 1.04 | 0.646 | 1.55 |
| 13 | 0.730 | 0.701 | 0.89 | 1.15 | 0.609 | 1.64 |
| 14 | 0.745 | 0.715 | 0.91 | 1.23 | 0.581 | 1.72 |
| 15 | 0.755 | 0.725 | 0.93 | 1.31 | 0.553 | 1.80 |
| 16 | 0.770 | 0.672 | 0.94 | 1.36 | 0.494 | 2.02 |
| 17 | 0.780 | 0.749 | 0.95 | 1.40 | 0.535 | 1.86 |
| 18 | 0.790 | 0.758 | 0.96 | 1.45 | 0.522 | 1.91 |

End of Document